SANDIA REPORT

SAND2014-0479
Unlimited Release
Printed January 2014

Investigation of ALEGRA Shock Hydrocode Algorithms Using an Exact Free Surface Jet Flow Solution

Bradley W. Hanks, Allen C. Robinson

Prepared by
Sandia National Laboratories
Albuquerque, New Mexico 87185 and Livermore, California 94550

Sandia National Laboratories is a multi-program laboratory managed and operated by Sandia Corporation, a wholly owned subsidiary of Lockheed Martin Corporation, for the U.S. Department of Energy's National Nuclear Security Administration under contract DE-AC04-94AL85000.

Approved for public release; further dissemination unlimited.

Sandia National Laboratories

Issued by Sandia National Laboratories, operated for the United States Department of Energy by Sandia Corporation.

NOTICE: This report was prepared as an account of work sponsored by an agency of the United States Government. Neither the United States Government, nor any agency thereof, nor any of their employees, nor any of their contractors, subcontractors, or their employees, make any warranty, express or implied, or assume any legal liability or responsibility for the accuracy, completeness, or usefulness of any information, apparatus, product, or process disclosed, or represent that its use would not infringe privately owned rights. Reference herein to any specific commercial product, process, or service by trade name, trademark, manufacturer, or otherwise, does not necessarily constitute or imply its endorsement, recommendation, or favoring by the United States Government, any agency thereof, or any of their contractors or subcontractors. The views and opinions expressed herein do not necessarily state or reflect those of the United States Government, any agency thereof, or any of their contractors.

Printed in the United States of America. This report has been reproduced directly from the best available copy.

Available to DOE and DOE contractors from
U.S. Department of Energy
Office of Scientific and Technical Information
P.O. Box 62
Oak Ridge, TN 37831

Telephone: (865) 576-8401
Facsimile: (865) 576-5728
E-Mail: reports@adonis.osti.gov
Online ordering: http://www.osti.gov/bridge

Available to the public from
U.S. Department of Commerce
National Technical Information Service
5285 Port Royal Rd
Springfield, VA 22161

Telephone: (800) 553-6847
Facsimile: (703) 605-6900
E-Mail: orders@ntis.fedworld.gov
Online ordering: http://www.ntis.gov/help/ordermethods.asp?loc=7-4-0#online

SAND2014-0479
Unlimited Release
Printed January 2014

Investigation of ALEGRA Shock Hydrocode Algorithms Using an Exact Free Surface Jet Flow Solution

Bradley W. Hanks and Allen C. Robinson
Computational Shock and Multiphysics
Sandia National Laboratories
P.O. Box 5800, MS-1323
Albuquerque, NM 87185-1323
acrobin@sandia.gov

Abstract

Computational testing of the arbitrary Lagrangian-Eulerian shock physics code, ALEGRA, is presented using an exact solution that is very similar to a shaped charge jet flow. The solution is a steady, isentropic, subsonic free surface flow with significant compression and release and is provided as a steady state initial condition. There should be no shocks and no entropy production throughout the problem. The purpose of this test problem is to present a detailed and challenging computation in order to provide evidence for algorithmic strengths and weaknesses in ALEGRA which should be examined further. The results of this work are intended to be used to guide future algorithmic improvements in the spirit of test-driven development processes.

Acknowledgment

We acknowledge the support and encouragement of the many ALEGRA team members in building the software environment and the numerical algorithms that this work is intended to support. Erik Strack has been highly supportive of every effort to examine and improve the algorithms found in ALEGRA. Rich Drake in particular has be very helpful in supporting the software infrastructure and in upgrading software tools.

Contents

Nomenclature **13**

1 Introduction **15**

2 Exact Solution Overview **23**

Steady Plane Irrotational Gas Dynamics in Hodograph Variables 23

Chaplygin Solution to the Plane Free Surface Wall Jet 26

Solution Evaluation 28

3 Comparing the Exact Solution to ALEGRA solutions **31**

4 ALEGRA Solution using Default Settings **39**

5 Artificial Viscosity **49**

6 Time Integration **55**

7 DeBar Advection **59**

8 Extended Finite Element Method (XFEM) **65**

9 CVFA and IMMA Mixed Material/Void **71**

Void Compression OFF 71

Void Compression ON 76

10 Lab Frame Simulations **79**

11 Conclusions **89**

References **91**

Appendix

A Exact Solution Evaluation Code **95**

List of Figures

1.1 Comparison of Chaplygin and Murnaghan gas isentropes for Cu. 20

2.1 Plane Jet Flow 26

3.1 Initial timestep of the shaped charge test problem in ALEGRA. 32

3.2 β = 90°: Density lineouts for the initial timestep in ALEGRA compared against the exact solution. 34

3.3 β = 90°: Pressure lineouts for the initial timestep in ALEGRA compared against the exact solution. 34

3.4 β = 90°: Temperature lineouts for the initial timestep in ALEGRA compared against the exact solution. 35

3.5 β = 45°: Density lineouts for the initial timestep in ALEGRA compared against the exact solution. 36

3.6 β = 45°: Pressure lineouts for the initial timestep in ALEGRA compared against the exact solution. 36

3.7 β = 45°: Temperature lineouts for the initial timestep in ALEGRA compared against the exact solution. 37

4.1 Temperature of the shaped charge at the initial timestep in ALEGRA where $\beta =$ 90° with 17 elements across the jet. 41

4.2 Temperature of the shaped charge at the final timestep in ALEGRA where $\beta = 90°$ with 17 elements across the jet. Compare with Figure 4.7. 41

4.3 Temperature of the shaped charge at the initial timestep in ALEGRA where $\beta =$ 45° with 5 elements across the jet. 42

4.4 Temperature of the shaped charge at the final timestep in ALEGRA where $\beta = 45°$ with 5 elements across the jet. Compare with Figure 4.13. 42

4.5 β = 90°: Temperature lineout on the axis for various mesh resolutions. 43

4.6 β = 90°: Temperature lineout in the middle of the jet for various mesh resolutions. 44

4.7 $\beta = 90°$: Temperature lineout on the jet surface for various mesh resolutions. Compare with Figure 4.2, 8.1, and 9.1. 44

4.8 $\beta = 45°$: Density lineout on the axis for various mesh resolutions. 45

4.9 $\beta = 45°$: Density lineout in the middle of the jet for various mesh resolutions. 45

4.10 $\beta = 45°$: Density lineout on the jet surface for various mesh resolutions. Compare to Figure 9.2. 46

4.11 $\beta = 45°$: Temperature lineout on the axis for various mesh resolutions. Compare with Figure 8.4, 9.3, and 10.3. 46

4.12 $\beta = 45°$: Temperature lineout in the middle of the jet for various mesh resolutions. Compare with Figure 8.5, 9.4, and 10.4. 47

4.13 $\beta = 45°$: Temperature lineout on the jet surface for various mesh resolutions. Compare with Figures 4.4, 8.6, 9.5, and 10.5. 47

5.1 $\beta = 90°$: On axis lineout for temperature with 17 elements across the jet testing ALEGRA artificial viscosity. 51

5.2 $\beta = 90°$: Mid-jet lineout for temperature with 17 elements across the jet testing ALEGRA artificial viscosity. 52

5.3 $\beta = 90°$: Jet surface lineout for temperature with 17 elements across the jet testing ALEGRA artificial viscosity. 52

5.4 $\beta = 45°$: Jet Surface lineout for density with 5 elements across the jet testing ALEGRA artificial viscosity. 53

5.5 $\beta = 45°$: On axis lineout for temperature with 5 elements across the jet testing ALEGRA artificial viscosity. 53

5.6 $\beta = 45°$: Mid-jet lineout for temperature with 5 elements across the jet testing ALEGRA artificial viscosity. 54

5.7 $\beta = 45°$: Jet surface lineout for temperature with 5 elements across the jet testing ALEGRA artificial viscosity. 54

6.1 $\beta = 90°$: Jet surface lineout for temperature with 17 elements across the jet to show the effects of midpoint. 56

6.2 $\beta = 45°$: On axis lineout for temperature to show the effects of midpoint. Compare with Figure 10.6. 57

6.3 $\beta = 45°$: Mid-jet lineout for temperature to show the effects of midpoint. Compare with Figure 10.7. 57

6.4 $\beta = 45°$: Jet surface lineout for temperature to show the effects of midpoint. Compare with Figure 10.8. 58

7.1 $\beta = 90°$: On axis lineout for temperature with 17 elements across the jet showing results from DeBar energy advection. 61

7.2 $\beta = 90°$: Mid-Jet lineout for temperature with 17 elements across the jet showing results from DeBar energy advection. 61

7.3 $\beta = 90°$: Jet surface lineout for temperature with 17 elements across the jet showing results from DeBar energy advection. 62

7.4 $\beta = 45°$: Jet surface lineout for density with 5 elements across the jet showing results from DeBar energy advection. 63

7.5 $\beta = 45°$: On axis lineout for temperature with 5 elements across the jet showing results from DeBar energy advection. 63

7.6 $\beta = 45°$: Mid-Jet lineout for temperature with 5 elements across the jet showing results from DeBar energy advection. 64

7.7 $\beta = 45°$: Jet Surface lineout for temperature with 5 elements across the jet showing results from DeBar energy advection. 64

8.1 $\beta = 90°$: Temperature lineout on the jet surface for the XFEM in ALEGRA. Compare to Figure 4.7. 66

8.2 $\beta = 90°$: Temperature plot at $11\mu s$ for the default settings of ALEGRA. 68

8.3 $\beta = 90°$: Temperature plot at $11\mu s$ for the XFEM in ALEGRA. 68

8.4 $\beta = 45°$: Temperature lineout on the axis for the XFEM in ALEGRA. Compare to Figure 4.11. 69

8.5 $\beta = 45°$: Temperature lineout in the middle of the jet for the XFEM in ALEGRA. Compare to Figure 4.12. 69

8.6 $\beta = 45°$: Temperature lineout on the jet surface for the XFEM in ALEGRA. Compare to Figure 4.13. 70

9.1 $\beta = 90°$: Temperature lineout on the jet surface for the CVFA. Compare with Figure 4.7 and 9.8. 72

9.2 $\beta = 45°$: Density lineout on the jet surface for the CVFA. Compare with Figure 4.10. 73

9.3 $\beta = 45°$: Temperature lineout on the axis for the CVFA. Compare with Figure 4.11. 73

9.4 $\beta = 45°$: Temperature lineout in the middle of the jet for the CVFA. Compare with Figure 4.12. 74

9.5 $\beta = 45°$: Temperature lineout on the jet surface for the CVFA. Compare with Figure 4.13 and 9.9. 74

9.6 $\beta = 90°$: Temperature lineout on the jet surface for the IMMA without void compression. Compare with Figure 4.7. 75

9.7 $\beta = 45°$: Temperature lineout on the jet surface for the IMMA without void compression. Compare with Figure 4.13. 75

9.8 $\beta = 90°$: Temperature lineout on the jet surface for the CVFA with void compression. Compare with Figure 9.1. 76

9.9 $\beta = 45°$: Temperature lineout on the jet surface for the CVFA with void compression. Compare with Figure 9.5. 77

10.1 Relationship of velocities in the laboratory frame of reference. 79

10.2 Laboratory Frame of Reference in ALEGRA for $\beta = 45°$. 80

10.3 $\beta = 45°$: Temperature lineout on the axis for comparison of mesh resolution with the laboratory frame of reference. Compare with Figure 4.11. 82

10.4 $\beta = 45°$: Temperature lineout in the middle of the jet for comparison of mesh resolution with the laboratory frame of reference. Compare with Figure 4.12. 82

10.5 $\beta = 45°$: Temperature lineout on the jet surface for comparison of mesh resolution with the laboratory frame of reference. Compare with Figure 4.13. 83

10.6 $\beta = 45°$: Temperature lineout on the axis for the laboratory frame of reference. Compare with Figure 6.2. 84

10.7 $\beta = 45°$: Temperature lineout in the middle of the jet for laboratory frame of reference. Compare with Figure 6.3. 84

10.8 $\beta = 45°$: Temperature lineout on the jet surface for the laboratory frame of reference. Compare with Figure 6.4. 85

10.9 $\beta = 45°$: Temperature lineout on the axis for the laboratory frame of reference with the XFEM. Compare with Figure 8.4. 86

10.10 $\beta = 45°$: Temperature lineout in the middle of the jet for laboratory frame of reference with the XFEM. Compare with Figure 8.5. 86

10.11 $\beta = 45^\circ$: Temperature lineout on the jet surface for the laboratory frame of reference with the XFEM. Compare with Figure 8.6. 87

List of Tables

1.1 Parameter values for a copper equation of state. 19

5.1 Artificial viscosity settings 49

Nomenclature

ρ	density
p	pressure
ν	specific volume
c	sound speed
e	specific internal energy
γ	power coefficient in isentropic equation of state relation
Γ	Grüneison coefficient
q	velocity magnitude or flow speed
q_∞, ρ_∞	subscript ∞ denotes a free streamline value in dimensional units
c_0, ρ_0	subscript 0 denotes stagnation point value in dimensional units
q_1, ρ_1	subscript 1 denotes a free streamline value in non-dimensional units
q_{max}	maximum speed
q_{cr}	critical speed
τ	$(q/q_{max})^2$
θ	angular flow direction
M	Mach number
u	$q\cos\theta$
v	$q\sin\theta$
ϕ	velocity potential
ψ	stream function
$\psi_n(\tau)$	fundamental Chaplygin function
$F_n(\tau)$	Chaplygin function given by Gauss hypergeometric series
β	incoming jet angle
a_n, b_n	useful parameters related F_n
W	complex potential
Ω	complex hodograph variable = $(q/q_1)e^{-i\theta}$
Θ	generic phase offset in series representations
V_n	velocity normal to shaped charge liner
V_{sp}	velocity of the stagnation point
V_t	velocity of the material flowing into the stagnation point
Q	artificial viscosity

Chapter 1

Introduction

Shock hydrocodes can be used to model interactions at very high pressures due to high velocity impact. These codes create simulations that model important, complex scenarios. A certain code may perform well under specific conditions and fail catastrophically in other cases. Due to the breadth of situations a code must handle, constant testing is required for improvement of the mathematical algorithms and their implementation. This type of test-driven development ensures continuous improvment and quality maintenance of a code. Verification and validation are two separate and distinct aspects of testing a simulation code. Verification compares the results of the code against known properties of the mathematical equations. Validation involves comparison of the results against experimental data for determination of the validity of the equations for the purposes intended. This work is a continuation of a 2002 SAND report entitled *"Evaluation Techniques and Properties of an Exact Solution to a Subsonic Free Surface Jet Flow"*, which detailed the theory and evaluation of an exact free surface compressible planar jet flow solution which closely mimics that of a shaped charge jet [28]. This report discusses the verification of ALEGRA, an arbitrary Lagrangian-Eulerian shock code, using this exact subsonic jet flow solution.

ALEGRA is an arbitrary Lagrangian-Eulerian (ALE) shock physics hydrocode that has been developed at Sandia National Laboratories since 1990 [30]. The code is designed for modeling shock waves and has the ability to handle complex geometries with multiple materials. ALEGRA can simulate a wide variety of scenarios involving shocks at high pressures.

A conical shaped charge includes a cylinder packed with a high explosive. A cone shape is hollowed out of the explosive and replaced with a metal liner. Upon detonation of the explosive material, the conical liner is collapsed forming a jet of metal. The jet forms and heats due to shock loading and plastic work [40, 24, 38]. A shaped charge jet may be idealized during the quasi-steady collapse phase with a steady compressible fluid model. Key features in this model include large velocity gradients in small spatial regions as well as very large strains in a steady subsonic isentropic free-surface flow. The features combine to generate computational difficulties with the shaped charge jet test problem. The shaped charge jet is very difficult to model correctly by either a Lagrangian finite element code or an Eulerian code. Lagrangian codes tend to experience severe deformation in the jet leading to a breakdown of the numerical method due to element distortion. The Eulerian codes may have difficulty with interfaces and excessive heating of jet material. The test problem proposed tests ALEGRA executing in Eulerian mode where the nodes move based on the velocity of the material(Lagrangian) and then the nodes are moved back to their original positions and quantities are remapped back onto this mesh (Eulerian).

Expected numerical issues for the shaped charge problem may include unrealistic temperature diffusion into the liner from the explosive products, nonphysical numerical exchange of kinetic energy to internal energy and heating due to artificial viscosity terms in high compression rate shockless processes [15, 31, 22]. Variations in numerical algorithms can produce dramatic differences in estimates of internal energy and temperature. The question is really one of entropy. In any numerical calculation one wishes any excess numerical production of entropy to be much smaller than the correct entropy increase. The numerical difficulties may be particularly acute when the flow to be computed is isentropic or poorly resolved. If confidence is to be placed in calculations which purport to include advanced material models that are highly dependent on temperature, it is necessary to develop reliable numerical methods and practical calculational rules of thumb to deal with the shaped charge jet problem in the case of simple hydrodynamic material modeling. For example, temperature dependent yield and fracture models require that heating in flows with or without shocks as well as heating due to plastic work be calculated accurately. Mechanical response is affected by solid-solid, solid-liquid and liquid-vapor phase transitions and these transitions will appear in the numerical simulation correctly only if the thermodynamic state space is traversed correctly. The proper application of advanced material modeling in shaped charge simulations thus depends upon proper energy partitioning in the numerical method. In particular it may be difficult for a numerical method to distinguish a rapid shockless transition from a true shock which is to be captured by the numerical method. Of course, it does not follow that an algorithm which can effectively computes a shockless flow properly will capture shocks well. The complete shaped charge jet problem requires consistent and effective modeling for both shocks and subsonic quasi-steady state flow. This report is concerned with a specific test problem which is used to test the current capability of ALEGRA, a shock capturing code, to model shockless high-strain-rate isentropic subsonic flow. The principal strategy and purpose for this work is to discover inconsistencies and anomalies which then give direction for research and development leading to improvements in numerical algorithms.

The conical shaped charge jet has been reasonably modeled in a gross engineering sense for years by the assumption that the jet collapse process is approximately a steady state in the frame of reference of the collapse point and that free-surface jet theory can be applied [3]. Operational shaped charges collapse the liner at a subsonic velocity in order to form coherent jets. Supersonic collapse speeds result either in no jet formation or incoherent jets [6]. Steady compressible subsonic plane and axis-symmetric free surface jet flows may be effectively calculated with specialized finite difference codes employing boundary fitting coordinate systems or by computing in the hodograph plane [23, 7]. The hodograph plane uses velocity and flow angle, (q, θ), as independent variables. However, as discussed above these same flows can still represent a significant challenge for *general purpose* transient dynamics codes. Karpp developed a test problem, the symmetrical impact of two plane jets, for the purpose of comparison with hydrodynamic code solutions and in order to better understand compressible jet flow [14]. He used the Chaplygin pressure-density relation given by

$$p = (\rho_\infty c_\infty)^2 (1/\rho_\infty - 1/\rho) = (\rho_\infty c_\infty)^2 (\nu_\infty - \nu) \tag{1.1}$$

where p is pressure, ρ_∞ is the reference or free surface density, $\nu = 1/\rho$ is the specific volume, and c_∞ is the reference sound speed. A material with the above response is often termed a Chaplygin gas. The Chaplygin gas has the well-known property that the hodograph plane equations of motion can be manipulated to give the incompressible equations of motion for which standard

incompressible methods apply. Thus any free-surface flow which can be solved by the usual methods of incompressible plane flow analysis can be solved for the Chaplygin gas. Karpp's work was used to assist in verifying a version of the HELP code which conserved internal energy instead of total energy in the remap step of the calculation [15].

The two parameters of the Chaplygin gas can be chosen to match any reference sound speed and pressure to give a linear curve in $p-v$ space. It is desirable to have an additional test problem for which the pressure-volume relation is concave upward. This is not simply an academic extension since curvature in the $p-v$ relation is necessary for heat addition in a shock process. Extremely high strain rate isentropic processes may have every appearance of a shock process to a finite resolution numerical grid. In order to fully test numerical methods, it appears that one is required to test with a pressure-volume relation which stiffens under compression. To this end one may choose the isentropic relation

$$p = \bar{p}(\rho) = \kappa_\infty((\rho/\rho_\infty)^\gamma - 1) \tag{1.2}$$

where $\kappa_\infty \equiv \rho_\infty c_\infty^2/\gamma$ and $p(\rho_\infty) = 0$. This relation is known as the Tait or Murnaghan equation of state and is clearly of the same form as that for an ideal gas with the pressure at reference density set to zero by subtracting a constant. The Chaplygin gas is a particular case of the above relation and is chosen by setting $\gamma = -1$.

One can choose κ_∞ and γ in Equation 1.2 to match the first and second derivatives with respect to ρ at ρ_∞ for any given isentrope. Of course the Hugoniot may also be used, if this is more convenient, since the Hugoniot and isentrope are the same to third order in the strain. A common form for the description of a metal Hugoniot is

$$p_H = \rho_\infty c_\infty^2 \eta/(1-s\eta)^2 \tag{1.3}$$

where $\eta = 1-\rho_\infty/\rho$. One may match either of these two curves locally near $\rho = \rho_\infty$ to the same order by the Murnaghan relation. Setting the first and second derivatives with respect to $1/\rho$ of Equations 1.3 and 1.2 equal at reference conditions leads to the equations

$$\gamma\kappa_\infty = \rho_\infty c_\infty^2 \tag{1.4}$$

$$\gamma(\gamma+1)\kappa_\infty = 4\rho_\infty c_\infty^2 s\ . \tag{1.5}$$

Solving for κ_∞ and γ yields the equations

$$\gamma = 4s - 1 \tag{1.6}$$

$$\kappa_\infty = \rho_\infty c_\infty^2/\gamma\ . \tag{1.7}$$

In this case the Chaplygin gas may be obtained by setting $s = 0$.

It is convenient to develop a simple general equation of state relationship which matches the Murnaghan gas isentropic relations. The most obvious candidate for such an equation of state for test purposes is a Mie-Grüneison relation for the pressure $p(e,\rho)$. In this case,

$$p(e,\rho) = \bar{p}(\rho) + \rho\Gamma(e - \bar{e}(\rho)) \tag{1.8}$$

where $\bar{e}$ satisfies the isentropic differential equation for the internal energy,

$$de = -pd\nu, \tag{1.9}$$

so that

$$\bar{e} - e_\infty = \frac{\kappa_\infty}{\gamma - 1}\left(\frac{1}{\rho}(\rho/\rho_\infty)^\gamma - \frac{1}{\rho_\infty}\right) + \kappa_\infty(1/\rho - 1/\rho_\infty) \ . \tag{1.10}$$

The Grüneison coefficient $\Gamma = \nu(\partial p/\partial e)_\nu$ is an arbitrary function of volume. For convenience, $\rho\Gamma = \alpha$ is taken to be constant. The heat capacity at constant volume, $c_\nu = (\partial e/\partial T)_\nu$, is also assumed constant. One can then derive equations for the energy, e (Equation 1.11), pressure, $p(\rho, T)$ (Equation 1.12), temperature, $\bar{T}$ (Equation 1.16), entropy, S (Equation 1.17), and sound speed, (c (Equation 1.21).

$$e - \bar{e}(\rho) = c_\nu(T - \bar{T}(\rho)) \tag{1.11}$$

and

$$p(\rho, T) = \bar{p}(\rho) + \alpha c_\nu(T - \bar{T}(\rho)) \ . \tag{1.12}$$

Application of the second law of thermodynamics allows the determination of the variation of $\bar{T}$ with ρ.

$$\begin{aligned} dS &= \frac{de}{T} + p\frac{d\nu}{T} && (1.13)\\ &= \frac{c_\nu}{T}dT + ((\partial e/\partial \nu)_T + p)\frac{d\nu}{T} && (1.14)\\ &= \frac{c_\nu}{T}dT + (\partial p/\partial T)_\nu d\nu \ . && (1.15) \end{aligned}$$

The identity $T(\partial p/\partial T)_\nu = (\partial e/\partial \nu)_T + p$ has been used in the final formula above. This identity follows from the consistency condition for dS to be an exact differential. Since $(\partial p/\partial T)_\nu = \alpha c_\nu$, Equation 1.15 is solvable on an isentrope. The solution of the differential equation for $\bar{T}$ is

$$\bar{T} = T_\infty e^{-\alpha(\nu - \nu_\infty)} \ . \tag{1.16}$$

Integrating at constant volume to obtain the entropy, S, yields

$$\begin{aligned} S &= \bar{S} + \int_{\bar{T}}^{T} \frac{c_\nu}{T}dT && (1.17)\\ &= S_\infty + c_\nu \log(T/T_\infty) + \alpha c_\nu(\nu - \nu_\infty) \ . && (1.18) \end{aligned}$$

A general relation for the sound speed is

$$\begin{aligned} c^2 &= (\partial p/\partial \rho)_S = (\partial p/\partial \rho)_T + (\partial p/\partial T)_\rho(\partial T/\partial \rho)_S && (1.19)\\ &= (\partial p/\partial \rho)_T + \frac{T}{\rho^2 c_\nu}(\partial p/\partial T)_\rho^2 \ . && (1.20) \end{aligned}$$

Since $(\partial p/\partial T)_\rho = \alpha c_v$ and $(\partial p/\partial \rho)_T = d\bar{p}/d\rho - \alpha^2 v^2 c_v \bar{T}$,

$$c^2 = d\bar{p}/d\rho + \alpha^2 v^2 c_v (T - \bar{T}) \ . \tag{1.21}$$

The above equations should be sufficient to provide enough information to implement this equation of state in any code framework. Note that for this reference isentrope, $p(\rho_\infty, T_\infty) = 0$. Copper parameters used in this report are listed in Table 1.1 in cgs units. These were obtained from the copper table on page 532 of Appendix E of Kinslow [16]. Only the first three parameters are relevant to the exact isentropic flow as summarized in this report. The remaining parameters are useful for defining the full equation of state in a hydrocode such as ALEGRA. A linear pressure-volume isentrope may be obtained with $s = 0$ ($\gamma = -1$).

ρ_∞	8.94 gm/cc
c_∞	3.94 10^5 cm/s
s	1.489 ($\gamma = 4.956$)
Γ	1.99
c_v	3.718 10^6 erg/(gm-deg K)
T_∞	293 deg K
e_∞	arbitrary
S_∞	arbitrary

Table 1.1. Parameter values for a copper equation of state.

Figure 1.1 shows the pressure-volume isentrope for a Chaplygin gas isentrope and for a Murnaghan isentrope which is matched to a standard Hugoniot relation for copper. The Mie-Grüneisen formulation, using the Murnaghan isentropic relation as a reference curve, represents a reasonable copper equation of state for conditions of interest and can be easily implemented as a simple equation of state model in any shock modeling code.

In this report we review computational procedures for evaluation of steady isentropic subsonic wall jet flows for the pressure-density relation of Equation 1.2 as given in great detail in [28]. The steady plane irrotational compressible fluid equations of motion in the hodograph plane variables, (q, θ), are separable and particular solutions can be obtained in terms of products of trigonometric functions and Gauss hypergeometric functions. These can be used to solve certain problems of a particular form that arise frequently in free surface flow theory. The original ideas and procedures are due to Chaplygin who solved the problem of a plane jet emerging from a slot in a wall [5]. A great many problems can be solved by Chaplygin's technique or variants of it [35].

This exact steady solution is imported into ALEGRA in order to test its ability to correctly model shockless isentropic subsonic free surface flow. The steady subsonic isentropic flow is a complex and challenging simulation for ALEGRA. While ALEGRA does not guarantee that the vorticity is zero for all time, the exact solution representation of the initial conditions should be close enough as to avoid any significant negative effects. The desired results are that the entropy will remain constant at all points while the temperature of any material point will stay on the

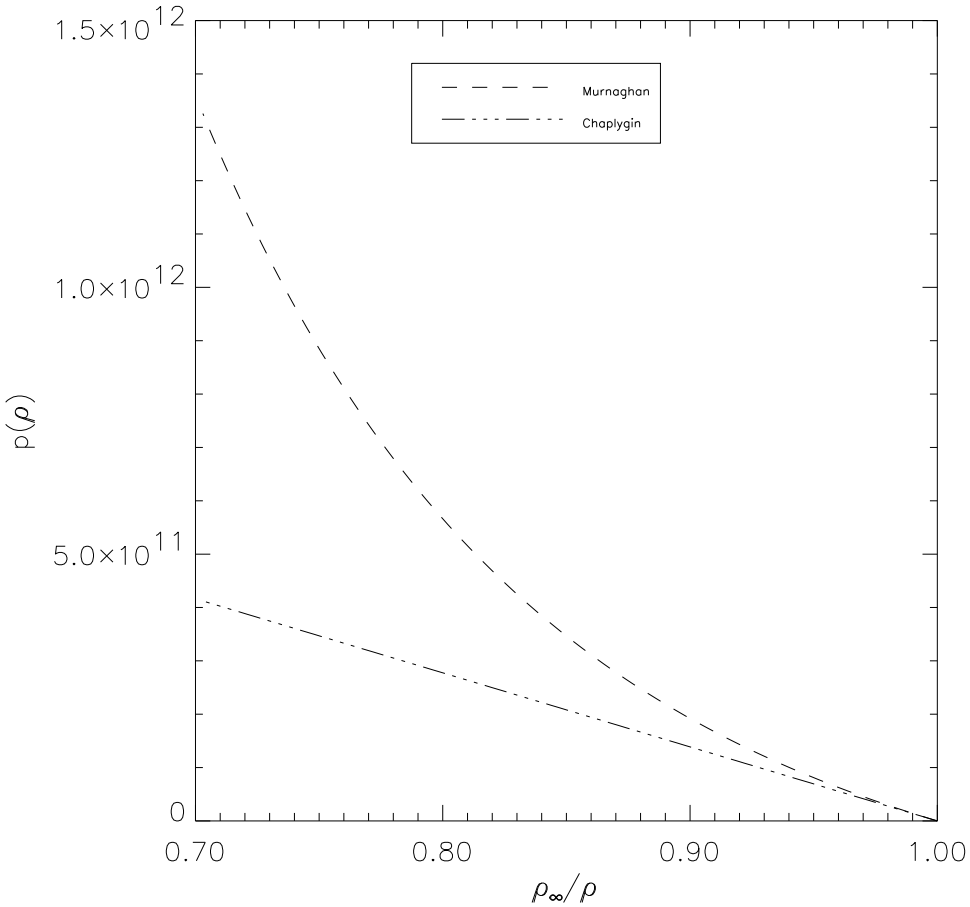

Figure 1.1. Comparison of Chaplygin and Murnaghan gas isentropes for Cu.

isentrope and then move toward the free-stream value as it flows into the fully released free-stream jet. The actual simulation results can then highlight numerical features of current algorithms and indicate which classical or newly implemented proposed advanced algorithms are candidates for acceptance or additional improvement and testing.

Chapter 2

Exact Solution Overview

This chapter of the report focuses on major details and concepts from the 2002 SAND report describing the analytic solution of a subsonic shaped charge jet [28]. Much of the theory but not the numerical details are presented in order to provide the reader with an immediate grasp of the solution methodology.

Steady Plane Irrotational Gas Dynamics in Hodograph Variables

The theory of steady plane irrotational adiabatic compressible inviscid flow theory in the hodograph variables, (q,θ), is well documented [2, 4, 12, 13, 20, 32]. A short summary of pertinent equations for our purposes follows below in the the notation of Bers [2]. In steady irrotational isentropic flow, with an assumed $p = p(\rho)$ relation, Bernoulli's theorem says that

$$\frac{q^2}{2} + \int \frac{dp}{\rho} = \frac{q^2}{2} + \int \frac{c^2 d\rho}{\rho} \tag{2.1}$$

is constant and thus gives a relation between density and flow speed. The density, sound speed, c, $(c^2 = dp/d\rho = -\rho q/\rho'(q))$, and Mach number, M, $(M^2 = -q\rho'(q)/\rho)$, are then computable as a function of speed alone. For the case of Equation 1.2 these relationships may be given explicitly. The Bernoulli equation becomes

$$\frac{q^2}{2} + \frac{c^2}{\gamma - 1} = \frac{c_0^2}{\gamma - 1} \tag{2.2}$$

where the subscript zero denotes stagnation point conditions $(q = 0)$. The stagnation point density and sound speed are given by

$$c_0^2 = c_\infty^2 (1 - \frac{\gamma - 1}{2} M_\infty^2) \tag{2.3}$$

$$\rho_0 = \rho_\infty (1 - \frac{\gamma - 1}{2} M_\infty^2)^{1/(\gamma - 1)} \ . \tag{2.4}$$

For convenience, units are now chosen such that, at the stagnation point $(q = 0)$, the density

$\rho_0 = 1$, and sound speed $c_0 = 1$. Thus

$$c^2 = 1 - \frac{\gamma - 1}{2} q^2 \tag{2.5}$$

$$\rho = (1 - \frac{\gamma - 1}{2} q^2)^{1/(\gamma-1)} \tag{2.6}$$

$$M^2 = \frac{q^2}{1 - \frac{\gamma-1}{2} q^2} \tag{2.7}$$

$$q^2 = \frac{M^2}{1 + \frac{\gamma-1}{2} M^2} \ . \tag{2.8}$$

The irrotationality assumption

$$\frac{\partial u}{\partial y} - \frac{\partial v}{\partial x} = 0 \tag{2.9}$$

implies the existence of a velocity potential ϕ such that $d\phi = udx + vdy$ where u and v are the x and y velocity components, respectively. Conservation of mass,

$$\frac{\partial(\rho u)}{\partial x} + \frac{\partial(\rho v)}{\partial y} = 0, \tag{2.10}$$

implies the existence of a stream function, ψ, such that $d\psi = -\rho v dx + \rho u dy$ represents the mass flux across a differential line element from left to right. The relations

$$u = \frac{\partial \phi}{\partial x} \qquad v = \frac{\partial \phi}{\partial y} \tag{2.11}$$

$$\rho u = \frac{\partial \psi}{\partial y} \qquad \rho v = -\frac{\partial \psi}{\partial x} \tag{2.12}$$

follow.

Assuming a one-to-one mapping between the physical plane (x, y) and the hodograph or velocity-angle space, (q, θ) with $(u, v) = (q\cos\theta, q\sin\theta)$, one obtains equations for the variation of the stream function and velocity potential in terms of q and θ. Thus

$$d\phi = udx + vdy = q(\cos\theta dx + \sin\theta dy) \tag{2.13}$$

$$d\psi = -\rho v dx + \rho u dy = \rho q(-\sin\theta dx + \cos\theta dy) \tag{2.14}$$

or

$$dz = dx + idy = \frac{e^{i\theta}}{q}\left(d\phi + \frac{i}{\rho} d\psi\right) \ . \tag{2.15}$$

Since dz is a perfect differential, so that the line integral in the physical plane is path independent, one obtains after considering that ϕ and ψ are functions of q and θ and equating the mixed derivatives of z with respect to q and θ, the equations

$$\frac{\partial \phi}{\partial \theta} = \frac{q}{\rho}\frac{\partial \psi}{\partial q} \qquad \frac{\partial \phi}{\partial q} = -\frac{(1 - M^2)}{q\rho}\frac{\partial \psi}{\partial \theta} \ . \tag{2.16}$$

Elimination of ϕ leads to an equation for the stream function

$$q^2\frac{\partial^2\psi}{\partial q^2}+q(1+M^2)\frac{\partial\psi}{\partial q}+(1-M^2)\frac{\partial^2\psi}{\partial\theta^2}=0\ . \tag{2.17}$$

This is termed the Chaplygin equation for the stream function. It is a separable linear second order equation whose coefficients depend only on the speed q. This equation possesses separable solutions of the form $\psi=\psi_n(q)e^{in\theta}$. In the case of the isentropic ideal gas relation, Chaplygin noted that if one writes

$$\psi=\tau^{n/2}F_n(\tau)e^{in\theta}=\psi_n(\tau)e^{in\theta} \tag{2.18}$$

where

$$\tau=(q/q_{max})^2=(\gamma-1)q^2/2 \tag{2.19}$$

so that

$$\tau_{cr}=(\gamma-1)/(\gamma+1) \tag{2.20}$$

then substitution in Equation 2.17 yields

$$\tau(1-\tau)F_n''+[n+1-(a_n+b_n+1)\tau]F_n'-a_nb_nF_n=0 \tag{2.21}$$

where

$$a_n+b_n=n-\frac{1}{\gamma-1} \tag{2.22}$$

$$a_nb_n=-\frac{n(n+1)}{2(\gamma-1)}. \tag{2.23}$$

Clearly, a_n and b_n are roots of a quadratic. In addition, we adopt the convention , $a_n<b_n$. It may be shown that either $\gamma>1$ or $\gamma\leq-1$ is required in order that a_n and b_n be real for every n.

One recognizes the solutions of Equation 2.21 as Gauss hypergeometric functions. The solution regular at $\tau=0$ is of particular interest to us and is given by

$$F_n(\tau)=\ {}_2F_1(a_n,b_n;n+1;\tau)=\sum_{m=0}^{\infty}\frac{(a_n)_m(b_n)_m}{(n+1)_m}\frac{\tau^m}{m!} \tag{2.24}$$

in the notation of Abramowitz and Stegun with $(a)_m\equiv(a)(a+1)\cdots(a+m-1)$ [1]. For the Chaplygin gas, $\gamma=-1$, so that $a_n=n/2$ and $b_n=(n+1)/2$. Then by a quadratic transformation formula,

$${}_2F_1(n/2,(n+1)/2;n+1;\tau)=\left(\frac{2}{1+\sqrt{1-\tau}}\right)^n\ . \tag{2.25}$$

(See 15.3.19 of [1].) Since Equation 2.17 is linear, boundary value problems may be solved by appropriate linear combinations of solutions. Free surface boundary value problems are especially amenable to solution since these surfaces are lines of constant velocity in hodograph variables.

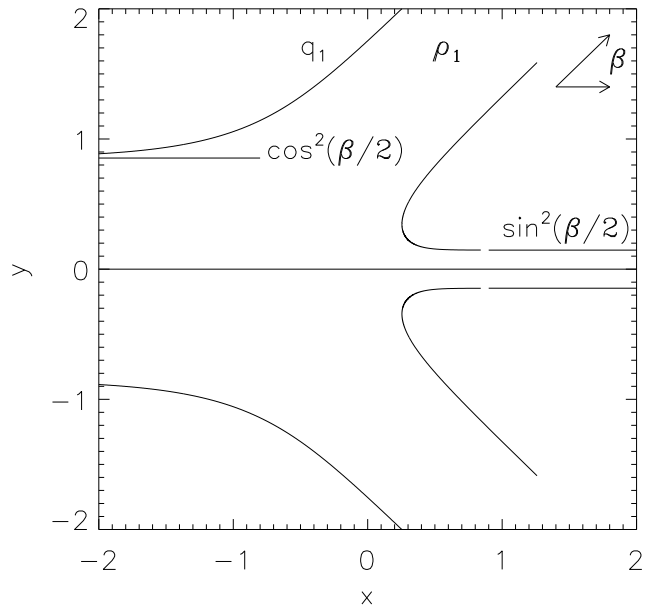

Figure 2.1. Plane Jet Flow

Chaplygin Solution to the Plane Free Surface Wall Jet

Imagine a plane free surface jet of unit width impinging on a wall at an angle β and subsonic velocity $q_1 < q_{cr}$ with an incoming flux $\Delta\psi = \rho_1 q_1$ where ρ_1 is the free streamline density and q_1 is the free streamline velocity. The jet splits into two outgoing streams of asymptotic widths $(1+\cos\beta)/2$ on the left and $(1-\cos\beta)/2$ on the right as is required from mass and linear momentum conservation. See Figure 2.1.

The Chaplygin procedure takes a solution of the incompressible problem and provides a similar subsonic compressible solution. The incompressible wall jet solution for this problem can be determined by standard complex variable techniques [4, 14]. The incompressible complex potential, $W = \phi + i\psi$, is given by

$$\begin{aligned} W(\Omega) = (q_1/\pi)\Big\{&\log(1+\Omega e^{i\beta}) + \log(1+\Omega e^{-i\beta}) \\ &-(1-\cos\beta)\log(1-\Omega) - (1+\cos\beta)\log(1+\Omega)\Big\} \end{aligned} \tag{2.26}$$

where $\Omega = (q/q_1)e^{-i\theta}$ is the incompressible velocity in complex form. Another representation for this solution may be given by expanding each of the log functions in a Taylor series about $\Omega = 0$.

Thus

$$
\begin{aligned}
W = -(q_1/\pi) \Bigg\{ & \sum_{n=2}^{\infty} \frac{1}{n} (q/q_1)^n e^{-in(\theta-\beta+\pi)} \\
& + \sum_{n=2}^{\infty} \frac{1}{n} (q/q_1)^n e^{-in(\theta+\beta-\pi)} \\
& - (1-\cos\beta) \sum_{n=2}^{\infty} \frac{1}{n} (q/q_1)^n e^{-in\theta} \\
& - (1+\cos\beta) \sum_{n=2}^{\infty} \frac{1}{n} (q/q_1)^n e^{-in(\theta-\pi)} \Bigg\} .
\end{aligned}
\tag{2.27}
$$

The $n = 1$ terms in each series sum exactly to zero as a consequence of the required mass and momentum balance and thus do not appear. The Chaplygin procedure for writing a corresponding subsonic compressible solution from an incompressible solution is to make the correspondence

$$
\left(\frac{q}{q_1}\right)^n \Rightarrow \frac{\psi_n(\tau)}{\psi_n(\tau_1)} \tag{2.28}
$$

in the formula for the stream function ψ where τ_1 is the value of τ on the free streamlines. Thus the stream function for compressible flow is

$$
\begin{aligned}
\psi = ((\rho_1 q_1)/\pi) \Bigg\{ & \sum_{n=2}^{\infty} \frac{1}{n} \frac{\psi_n(\tau)}{\psi_n(\tau_1)} \sin n(\theta-\beta+\pi) \\
& + \sum_{n=2}^{\infty} \frac{1}{n} \frac{\psi_n(\tau)}{\psi_n(\tau_1)} \sin n(\theta+\beta-\pi) \\
& - (1-\cos\beta) \sum_{n=2}^{\infty} \frac{1}{n} \frac{\psi_n(\tau)}{\psi_n(\tau_1)} \sin n\theta \\
& + (1+\cos\beta) \sum_{n=2}^{\infty} \frac{1}{n} \frac{\psi_n(\tau)}{\psi_n(\tau_1)} \sin n(\theta-\pi) \Bigg\} .
\end{aligned}
\tag{2.29}
$$

An extra factor of ρ_1 is applied in the above formula since the stream function in the compressible case represents a mass flux. The convergence theory for this series, called a Chaplygin series, has been described by Sedov [32] and a summary of the theory is given in a previous report [28].

Integration to obtain the physical plane may be accomplished in several ways since the physical plane is independent of integration path in the (q,θ) plane. The evaluation code actually implements two different approaches which utilize Equations 2.29, 2.15 and 2.16 to obtain a complex series for $\partial z/\partial q$ and $\partial z/\partial\theta$. In the first $\partial z/\partial q$ is evaluated for each point (q,θ) and then $z(q,\theta)$ is obtained by numerical integration with respect to q subject to $z(0,\theta) = 0$ using the trapezoidal rule. Summation of the series near the free surface require the use of a non-linear convergence accelerator for summing the slowly convergent and divergent series. The second technique is to integrate $\partial z/\partial\theta$ with respect to θ analytically and sum the resultant series of integrated terms to obtain the position $z(q,\theta)$.

Solution Evaluation

The exact solution discussed in the previous section can be written down with relative ease. The difficulty now with this solution (as with many non-trivial exact solutions) is that the properties of the solution are not immediately obvious and an efficient and accurate numerical evaluation of the solution is needed for any chosen value of the Mach number, M, and the collapse angle, β. We give a brief summary of this significant effort which has been previously documented [28]. There are two major tasks: first, the Chaplygin functions, $F_n(\tau)$, must be computed, and second, the infinite series related to the solution must be effectively summed. This summation is a particular problem near the free surface since the convergence of the series is very slow.

In [5], Chaplygin used a continued fraction approximation to compute

$$(2\tau/n)\psi_n'/\psi_n = 1 + (2\tau/n)F_n'/F_n.$$

This was sufficient to allow the computation of the contraction ratio for a planar jet emanating from a slit in a semi-infinite reservoir. Frank has given a number of continued fraction representations for ratios of Gauss hypergeometric functions [11]. The representations were derived by manipulation of the three term contiguous relations for the hypergeometric function. The primary representation used in this work is discussed below. Consider continued fractions of the form

$$\beta_0 + \frac{\alpha_1 \mid}{\mid \beta_1} + \frac{\alpha_2 \mid}{\mid \beta_2} + \frac{\alpha_3 \mid}{\mid \beta_3} + \cdots . \tag{2.30}$$

where, for example, three terms of the continued fraction give

$$\beta_0 + \frac{\alpha_1}{\beta_1 + \frac{\alpha_2}{\beta_2}}. \tag{2.31}$$

A continued fraction representation (Equation (2.5') vii of [11]) is given by the coefficients

$$\alpha_k = -\frac{(b+k)(c-a+k-1)}{(c+k-1)(c+k)}\tau \qquad k = 1,2,3,\cdots \tag{2.32}$$

$$\beta_k = \frac{b-a+k}{c+k}\tau + 1 \qquad k = 1,2,3,\cdots \tag{2.33}$$

with $\beta_0 = 1$. This continued fraction converges to the generating function

$$\frac{F(a,b;c;\tau)}{F(a+1,b+1;c+1;\tau)} + \frac{a\tau}{c} = \frac{abF(a,b;c;\tau)}{cF'(a,b;c;\tau)} + \frac{a\tau}{c} \tag{2.34}$$

provided $\mid \tau \mid < 1$. The prime represents differentiation with respect to τ. The limit characteristic equation associated with the forward difference equation for the continued fraction is

$$\sigma^2 - (1+\tau)\sigma + \tau = 0 \tag{2.35}$$

and has roots 1 and τ. Thus for $\gamma > 1$ and subsonic values of τ ($0 < \tau < (\gamma-1)/(\gamma+1) < 1$), this continued fraction leads to an effective computation of the ratio F'/F.

The ratios F'/F are needed to compute shapes of free streamlines and related fundamental quantities (e.g. the compression ratio for a jet from a slit). For some applications this may be sufficient and no further information about F would be necessary. However, since the whole flow field is of interest for code verification studies, the F'/F information obtained above can be used to compute F in a useful form. Numerical integration leads immediately to values of $\log F(\tau)$ with $\log(F(0)) = 0$. The trapezoidal rule with Romberg extrapolation is used for the numerical integration scheme. The ratio $\psi_n(\tau)/\psi_n(\tau_1)$ is given by

$$\psi_n(\tau)/\psi_n(\tau_1) = \exp\{(n/2)\log(\tau/\tau_1) + \log F_n(\tau) - \log F_n(\tau_1)\}. \tag{2.36}$$

Forming sums and differences of logs prior to exponentiation has the advantage of avoiding underflow errors for large values of n. The above algorithm was found to be accurate, reliable and effective with no apparent numerical difficulties.

Once the Chaplygin functions are available, it is necessary to sum the series solutions. The series solutions given by the Chaplygin technique are very slowly convergent for points near to the free surface. For $q = q_1$ but away from the singular points the z series is conditionally convergent and the $\partial z/\partial q$ series is divergent. It therefore seems necessary to sum the series using a convergence accelerator which will successfully accelerate the convergent series as well as sum the divergent series on the boundary. Both summations are required for a complete solution specification since $\partial z/\partial q$ is needed to compute velocity gradients.

What is meant by the "sum" of a divergent series? A series can be thought of as a limited representation of an underlying function. This representation makes mathematical sense only where it is convergent. However, it can be meaningfully related to an extension of this function outside the original domain of validity of the representation. For example, the complex series $1+z+z^2+\cdot$ is convergent only for $|z| < 1$ while the equivalent representation $1/(1-z)$ is valid everywhere except at the pole $z = 1$. Successful series acceleration and summation techniques essentially extract a more fundamental representation from a sequence of finite sums.

The ε-algorithm was found to be a successful accelerator for summing the series representation for $\partial z/\partial q$ and z. The sums were computed separately and as complex sequences. This preserves the simple structure of the sums and precluded the failure of the acceleration algorithm due to the presence of zero or very small terms in the real or imaginary parts. The ε algorithm appears successful since the algorithm will successfully compute the analytic continuation of meromorphic functions in the complex plane with a finite number of poles. See page 131 of [39].

The ε-algorithm has been implemented previously by Nieuwland (1967) to accelerate the the convergence of Chaplygin series [21]. The ε-algorithm is an economical procedure for evaluating the Schmidt transformation or iterated Shank's transformation for accelerating the convergence of certain sequences. Given a sequence $s_m, m \geq 0$ with m integral the ε-algorithm is defined by

$$\varepsilon_{k+1}^{(m)} = \varepsilon_{k-1}^{(m+1)} + kk(\varepsilon_k^{(m+1)} - \varepsilon_k^{(m)})^{-1} \qquad m,k \geq 0 \tag{2.37}$$

$$\varepsilon_{-1}^{(m)} = 0, \quad \varepsilon_0^{(m)} = s_m \qquad m \geq 0. \tag{2.38}$$

The values $\varepsilon_{2k}^{(m)}$ are used as estimates for the limit of the sequence s_m given by the partial sum of the series.

The variation of the pressure, density and energy are all computable from the velocity, q. These can be plotted at the mesh locations which are computed from the solution as described above. Additional kinematic quantities are of interest and can also be computed from the solution. The methodology and description of how this can be done along with a comparison of flow characteristics with respect to variation in the exponent γ is found in the preceding report [28].

A stretched evaluation mesh is utilized in both the θ direction and the q direction. The θ mapping is two cubic polynomials connecting the θ values corresponding to the singularities. The θ values match at the singularities, but the slopes with respect to the linear θ are set zero at the singular values of θ. This has the effect of concentrating more points near singularities so that better coverage is obtained in physical space. The q mesh is a linear q mesh near the origin which switches to a linear τ mesh at a specified mesh number. This has the effect of generating smooth line plots in physical space. The code given in Appendix A allows for specification of the θ and τ stretching options.

Chapter 3

Comparing the Exact Solution to ALEGRA solutions

The exact solution detailed in Chapter 2 is imported into ALEGRA for the purpose of test-driven development for continuous improvement of the numerical algorithms. Only the full Eulerian remap option is used for testing the exact solution. Since the exact solution is a steady solution, we wish to import this solution as initial conditions. We then expect this solution to be maintained for some time period until the effects of the jet at "infinity" possibly interacting with mesh boundaries become apparent. The solution is imported through the diatom exodus solution import facility in ALEGRA. Once imported, a number of tests are run which are intended to test various algorithms in ALEGRA. Some algorithms are relatively new and other have been in the code for a long time. The intent of the detailed comparisons in this report is to highlight subtle numerical issues which may be present when a shock code is applied to this subsonic isentropic flow problem. In particular it is expected that irreversible heating may occur in the ALEGRA algorithms. The challenge is to determine from testing which algorithms or combination of algorithms give the best results and which might clearly seen as needing improvement and in what ways. The results of testing the default settings of ALEGRA, artificial viscosity, midpoint time integration, DeBar energy advection, the extended finite element method(XFEM), and mixed material/void algorithms are shown in Chapters 4 through 9.

The simulation is run using two incident angles ($\beta = 90^\circ$, $\beta = 45^\circ$) in the stagnation point frame of reference. The stagnation point frame of reference provides a simpler way of viewing the shaped charge jet simulation. The imported solution remains stationary and material is added to create a continuous flow through the imported solution thereby forming a jet as shown in Figure 3.1. In Chapter 10, a second frame of reference is detailed and results are shown.

The input parameters and CJETB code shown in Appendix A are used to create an exodus file containing the exact solutions for both angles, $\beta = 90^\circ$ (timestep 1) and $\beta = 45^\circ$ (timestep 2). It creates the solution using the EXODUS I format. For analysis and visualization, the EXODUS I file is then converted to EXODUS II format. The parameters used for the simulation approximately match a copper equation of state as given in Table 1.1. The free-stream Mach number is set to .9.

The testing of ALEGRA focuses on the under-resolved case of the test problem. High resolution runs improve the code results at the expense of requiring greater computing power to complete the problem. Ideally this problem will guide future improvement of algorithms at lower

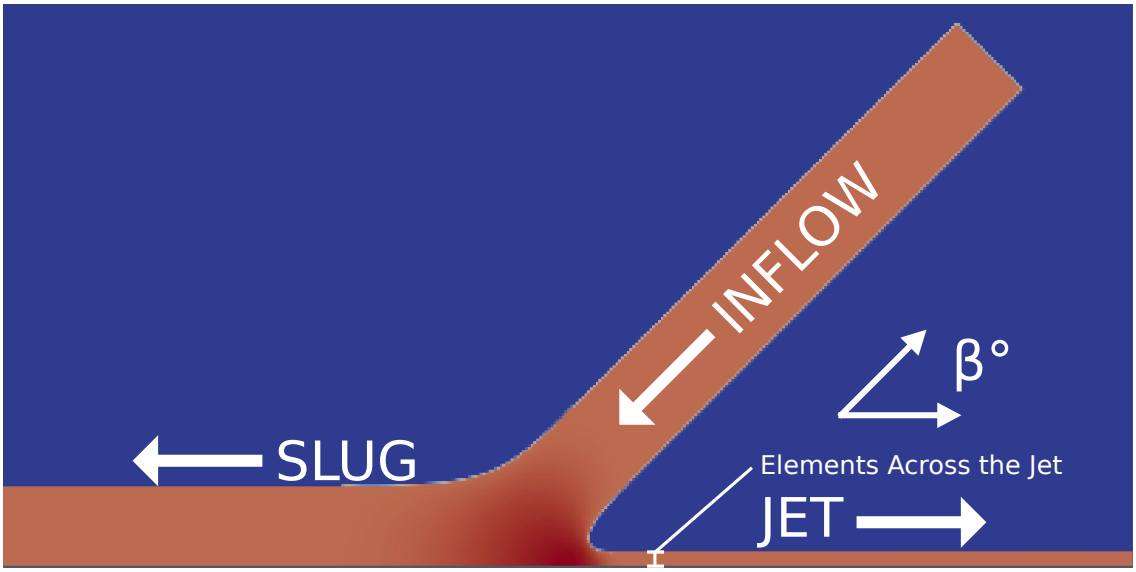

Figure 3.1. Initial timestep of the shaped charge test problem in ALEGRA.

resolutions. With improved algorithms for lower resolution, ALEGRA will require less computing power to achieve the same accuracy as high resolution simulations. Chapter 4 contains information and results regarding the default settings of ALEGRA. It includes plots which compare the effects of increasing the mesh resolution. The under-resolved cases with larger errors provide better insight into algorithmic improvements. Plots are labeled by the number of elements across the jet as shown in Figure 3.1. The height of the jet is dependent on the angle β as shown in Figure 2.1, therefore the number of elements across the jet varies, as β varies, in order to achieve the same resolution. When $\beta = 90°$, the typical under-resolved case includes 17 elements across the jet. A high resolution run includes between 31 and 57 elements across the jet. When $\beta = 45°$, the typical under-resolved case includes 5 elements across the jet. A typical run at high resolution includes between 9 and 17 elements across the jet.

The results of a "perfect" simulation would not change as time progresses because the analytic solution is for a steady state problem. The material would heat up as it compresses and then release and return to its original temperature. The entropy would be constant and uniform throughout the whole problem. It is expected that there will be some initial very small waves and oscillations as the simulation begins due to finite resolution and imperfections in the initial state. These oscillations may be expected to diminish and damp out as time progresses. The oscillations may cause fluctuations in dependent variables such as temperature but should be small and reach a quasi-steady state. Once a quasi-steady state is achieved, analysis is performed to view any variations from the analytic solution.

Analysis of the results are performed using horizontal lineouts which are compared against the analytic solution. Three lineouts are used for each case. The main focus of analysis is in the stagnation point region and along the surface of the jet. Density, pressure, and temperature are

reviewed for each lineout. There is a lineout through the elements along the axis, through the elements in the middle of the jet, and through the elements closest to the surface of the jet. They are referred to as lineouts “on-axis”, “mid-jet”, and “jet-surface”, respectively. The nature of the test problem allows for comparison of later timesteps with the initial timestep to provide evidence for the correct subsonic isentropic flow.

In order to compare the initial timestep against later timesteps, it is first necessary to ensure the initial timestep matches the analytic solution. The initial timestep for the ALEGRA simulation imports the exact solution through the exodus diatom solution import. Lineouts as described above are used to compare the analytic solution from the CJETB code and initial timestep. Figures 3.2 - 3.7 show the exact solution is imported correctly into the initial timestep and matches the analytic solution.

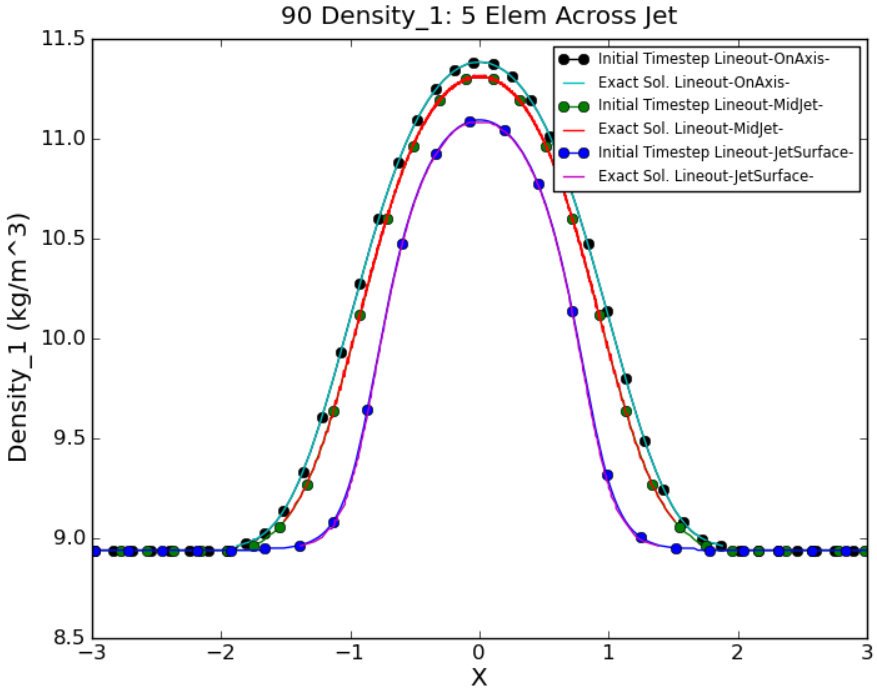

Figure 3.2. $\beta = 90°$: Density lineouts for the initial timestep in ALEGRA compared against the exact solution.

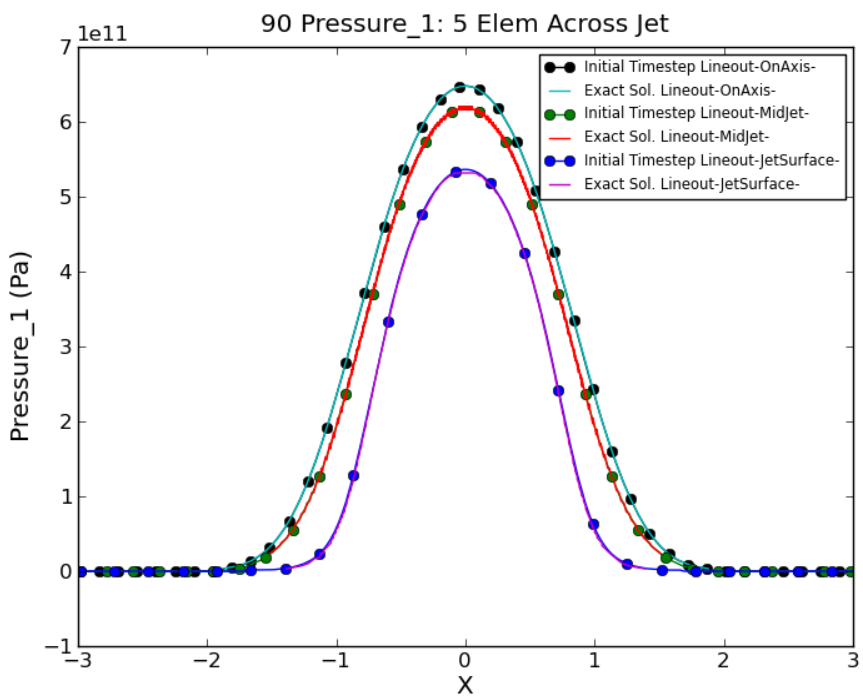

Figure 3.3. $\beta = 90°$: Pressure lineouts for the initial timestep in ALEGRA compared against the exact solution.

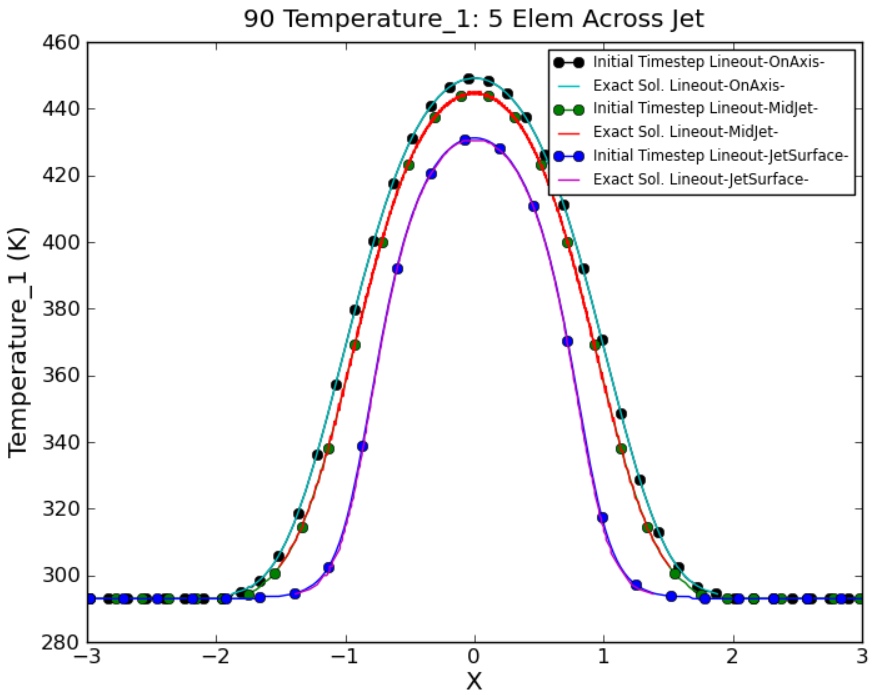

Figure 3.4. $\beta = 90°$: Temperature lineouts for the initial timestep in ALEGRA compared against the exact solution.

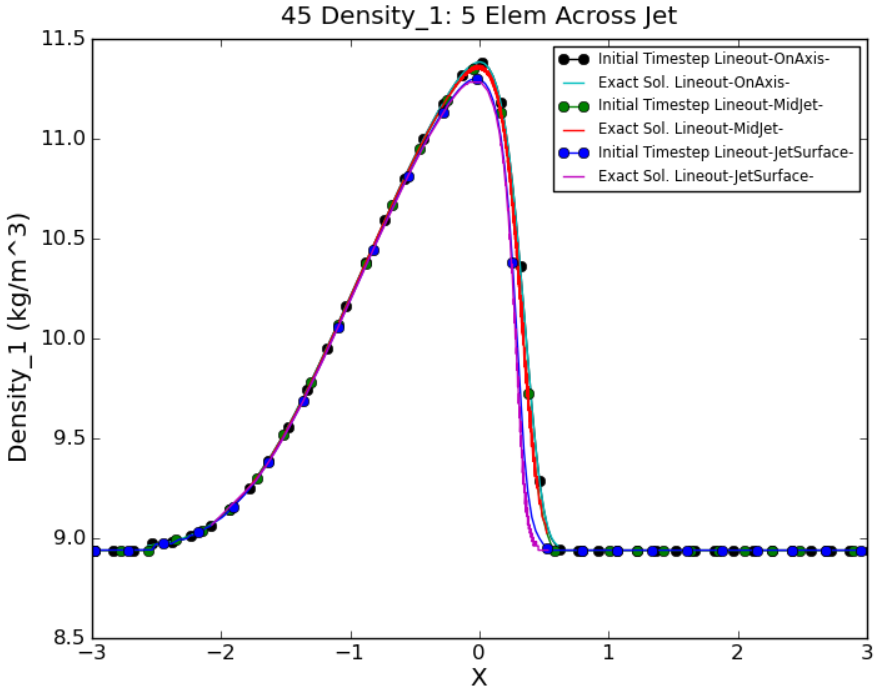

Figure 3.5. $\beta = 45°$: Density lineouts for the initial timestep in ALEGRA compared against the exact solution.

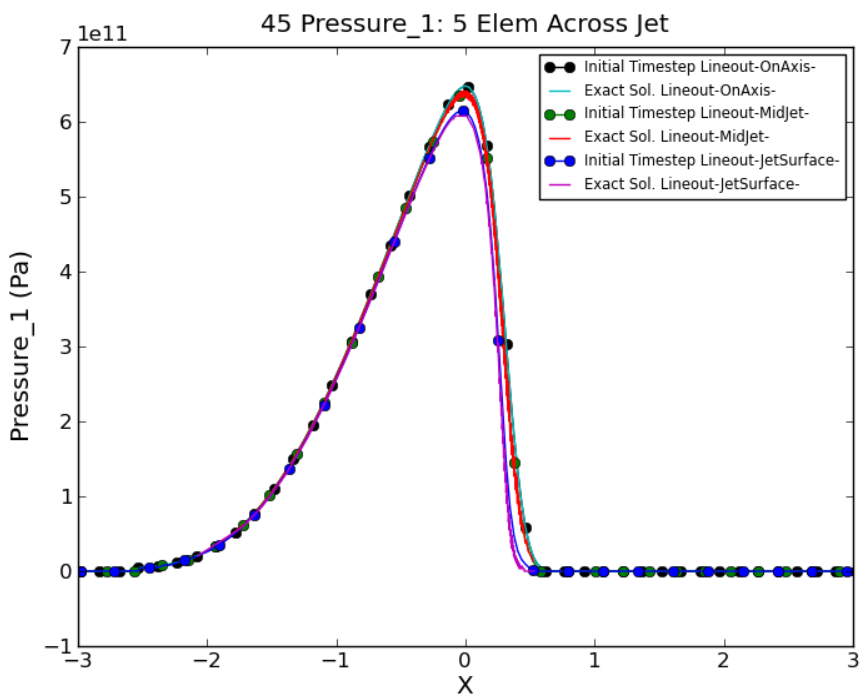

Figure 3.6. $\beta = 45°$: Pressure lineouts for the initial timestep in ALEGRA compared against the exact solution.

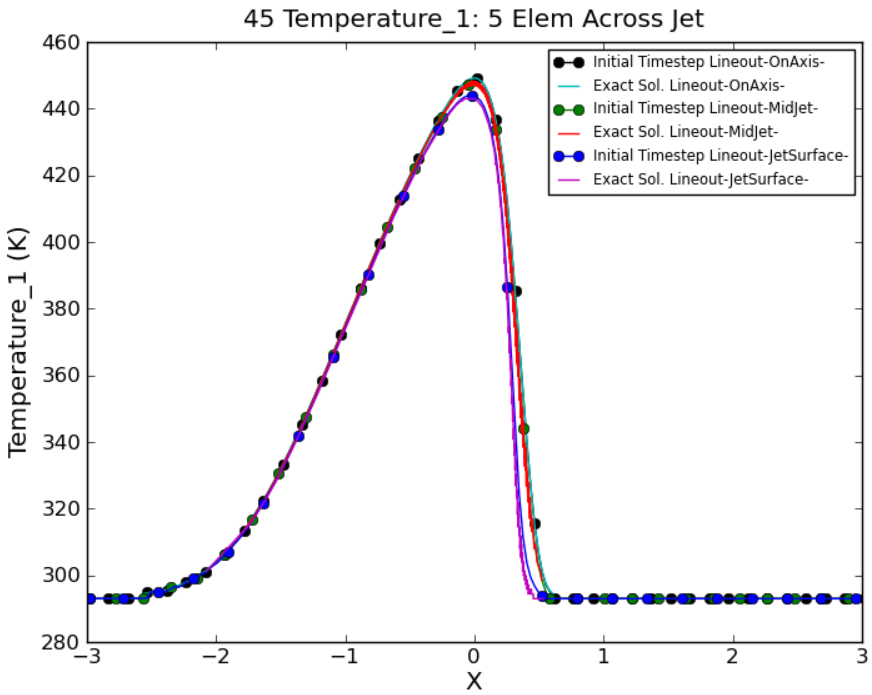

Figure 3.7. $\beta = 45°$: Temperature lineouts for the initial timestep in ALEGRA compared against the exact solution.

Chapter 4

ALEGRA Solution using Default Settings

As the simulation begins, small oscillations occur near the stagnation point and the corner where the jet is formed. These two areas are expected to be the most difficult because of the high compression and release, and the sharp change in velocity around the corner. These oscillations are not unexpected and are caused by small local interactions as the truncation errors in the numerical solution try to adjust to the exact initial conditions. These oscillations are greatly reduced after a few ALEGRA time steps. At the final timestep of 15 μs, the oscillations that occurred at the beginning have diminished and the effects have been pushed farther along in the jet as more material moves through stagnation point. When $\beta = 90°$, ALEGRA is able to handle the isentropic flow very well. Figures 4.1 and 4.2 show a close up view of the temperature at t = 0.0μs and t = 15μs respectively. All appears correct with the exception of a slight increase in temperature visible along the surface of the jet at t = 15μs.

Figures 4.3 and 4.4 show the temperature for $\beta = 45°$ at t = 0.0 μs and t = 15 μs respectively. From these plots a more significant rise in temperature is seen along the surface of the jet, including a particular increase in the corner where material flows into the jet. Important to note is the lack of temperature rise along the slug. While the simulation with $\beta = 90°$ shows an increase in temperature on both sides of the inflow, when $\beta = 45°$ the increase in temperature is focused at the sharp corner and extends into the jet. Thus, from Figure 4.4, it is clear that a major issue occurs in the tight corner where the jet is formed. Where $\beta = 90°$, as seen in Figure 4.2, the temperature errors in the corners on either side of the inflow are equivalent. Where $\beta = 45°$ the corners on either side of the inflow are not equivalent, one being approximately 135° and the other being approximately 45°. For the smaller angle there is a significant rise in temperature while there is little to no change in temperature for the larger angle. As β decreases the corner that the material must turn becomes much sharper and the presence of numerical difficulties is not unexpected. The test problem was also run using pattern interface reconstruction (PIR), a 2nd order interface tracker in ALEGRA. PIR shows an insignificant variation from the default interface tracker in ALEGRA for this test problem.

The lineouts for temperature, where β = 90°, are shown in Figures 4.5 - 4.7 at t = 15μs. For many variables the simulation matches the analytic solution well. In this case, temperature lineouts are used to show deviations from the analytic solution. Also included in these lineouts are several different resolution qualities. As explained in Chapter 3, and shown in these plots, the high resolution plots more closely match the analytic solution, particularly along the surface of the jet. Figures 4.5 - 4.7 show that there are increased temperatures along the surface of the jet. The error

in temperature is inversely related to the resolution of the mesh. Greater errors are seen for β = 45°.

Figures 4.8 - 4.13 show lineouts for density and temperature for β = 45° at t = 15μs. As with the previous case, the greatest issues occur along the surface of the jet. Figures 4.8 - 4.10 show that the density diverges from the analytic solution as the lineout moves toward the jet surface. The decrease is likely due to the extreme rise in temperature along the jet seen in Figures 4.11 - 4.13. The lineout on the axis and through the middle of the jet show slight increase in temperature while the greatest increase is along the jet surface shown in Figure 4.13. At greater computational expense as the mesh resolution increases the temperature error decreases along the surface of the jet.

Analyzing similarities and differences seen in these two cases where $\beta = 45°$ and 90° pinpoints where issues are occurring. Figures 4.7 and 4.13 are used for the comparison. Both figures show the temperature error along the surface of the jet is inversely related to the resolution of the mesh. Clearly smaller elements improve the accuracy of the simulation. Another clear issue as explained in Chapter 3 is the angle of the shaped charge. As β increases, the errors along the surface of the jet decrease. The largest angle is the slug in Figure 4.13 at approximately 135°. At this large angle no significant errors are visible. As the material moves from the inflow into the slug, the corner is moderate providing a smoother transition. Evidence of major issues in sharp corners are also seen in both Figures. There are spikes in the temperature that occur near the sharp corners. The clearest evidence of these spikes is seen not only in the lineouts but also in Figure 4.4. This figure shows the hottest portion of the simulation to be in the sharp corner.

Other similarities are seen in reference to the quasi-steady state achieved. The oscillations from the initial timesteps are seen clearly in Figure 4.13. From the position X = 1 to X = 2, the temperature is constant at about 600 kelvin with a mesh resolution of 5 elements across the jet. This region for $1 < X < 2$ represents a quasi-steady state that has been reached. For $X > 2$, the effects of the initial oscillations in the stagnation point are seen and are pushed out as the test is allowed to progress further in time. Though it appears the temperature along the surface of the jet returns to the correct value as $X \rightarrow 6$, this area is material from the initial state still being pushed out as material enters the jet from the inflow. Therefore Figure 4.13 shows an error of roughly 300 kelvin along the jet surface for β = 45° with 5 elements across the jet.

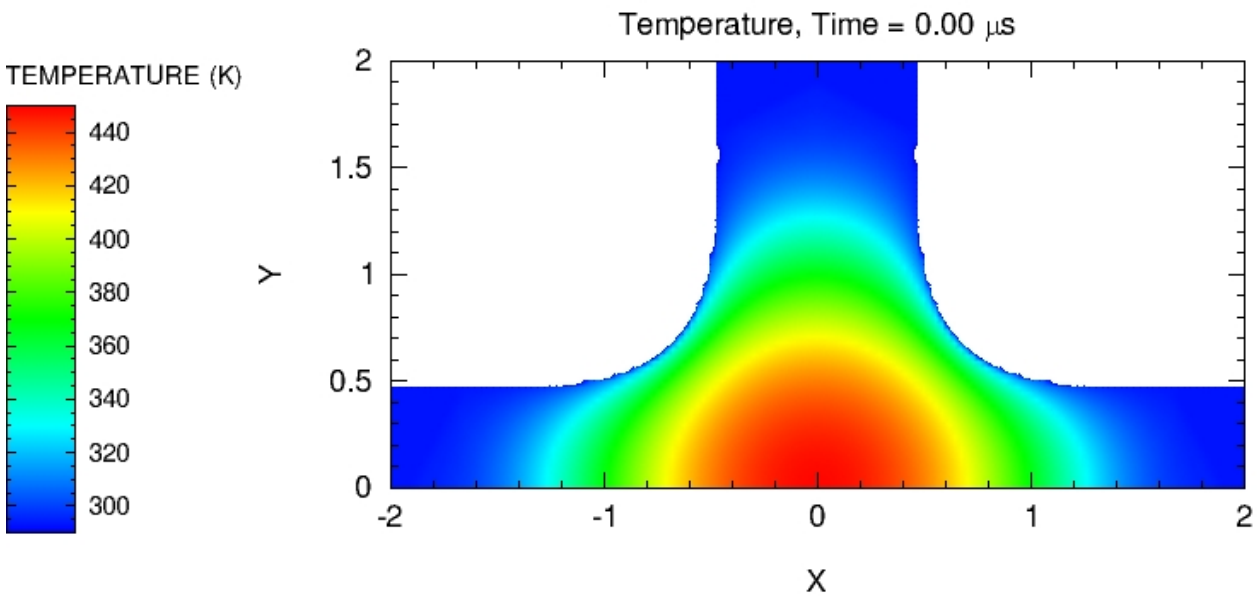

Figure 4.1. Temperature of the shaped charge at the initial timestep in ALEGRA where $\beta = 90°$ with 17 elements across the jet.

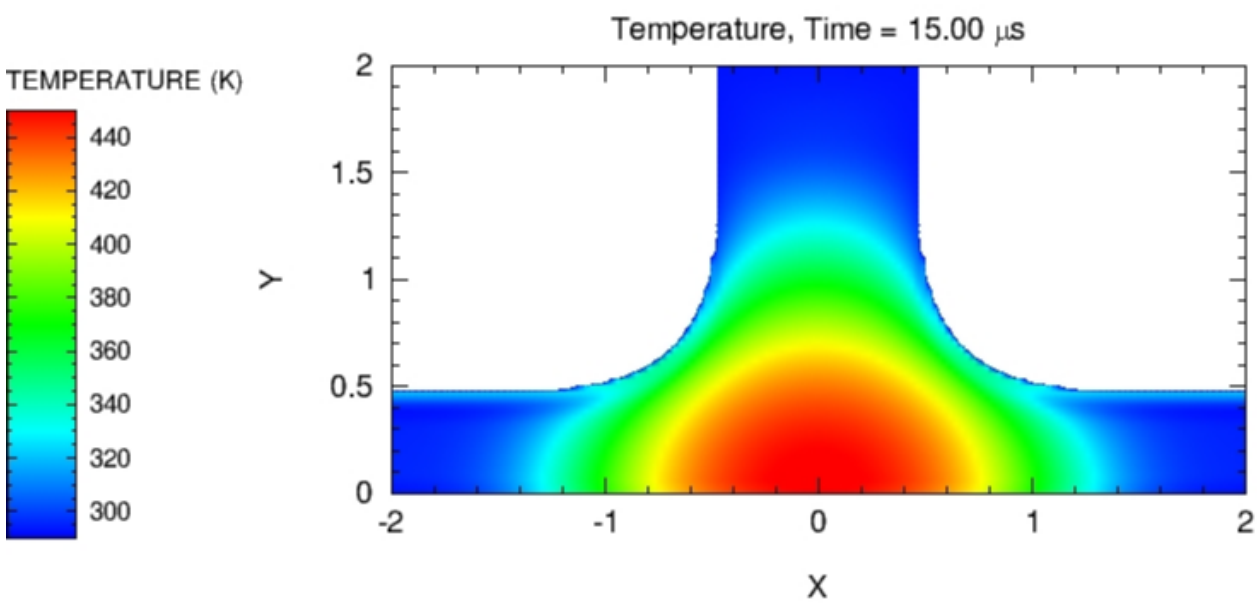

Figure 4.2. Temperature of the shaped charge at the final timestep in ALEGRA where $\beta = 90°$ with 17 elements across the jet. Compare with Figure 4.7.

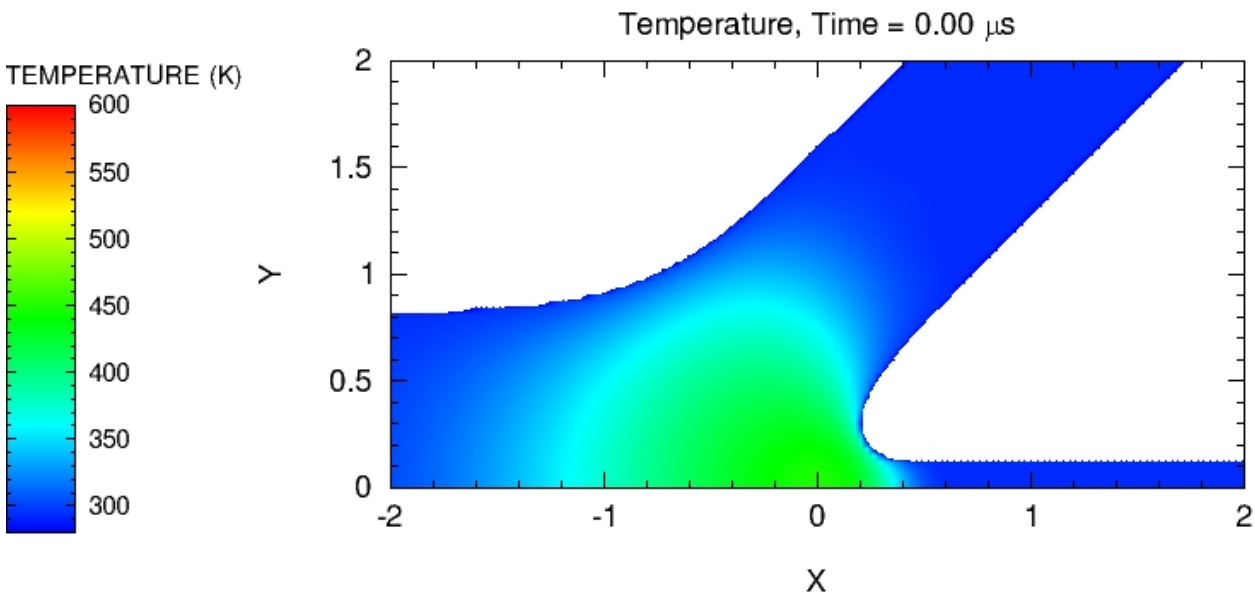

Figure 4.3. Temperature of the shaped charge at the initial timestep in ALEGRA where $\beta = 45°$ with 5 elements across the jet.

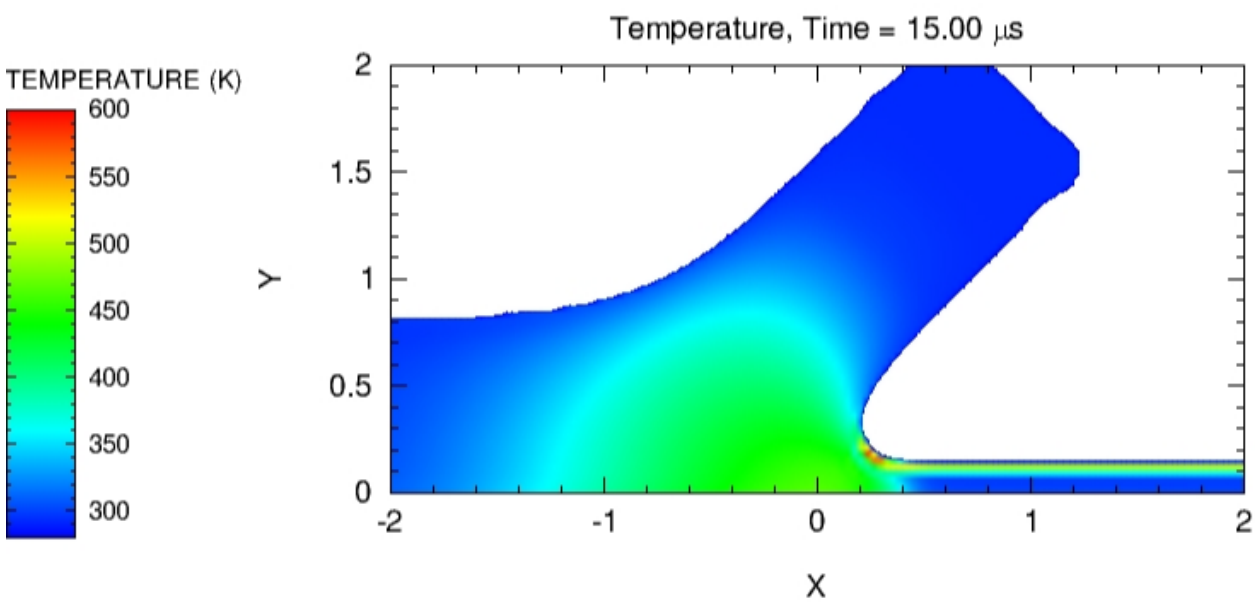

Figure 4.4. Temperature of the shaped charge at the final timestep in ALEGRA where $\beta = 45°$ with 5 elements across the jet. Compare with Figure 4.13.

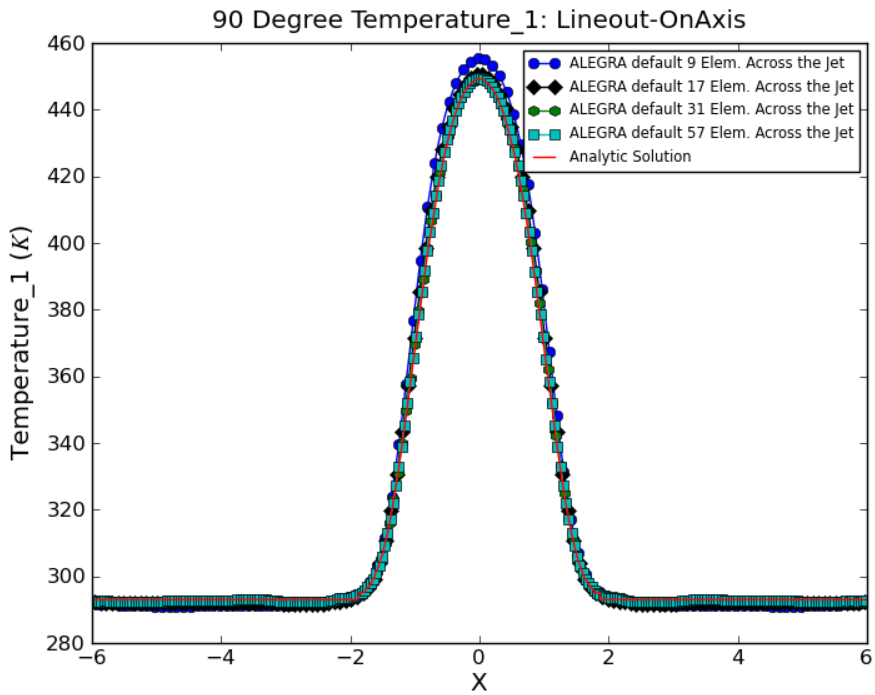

Figure 4.5. $\beta = 90°$: Temperature lineout on the axis for various mesh resolutions.

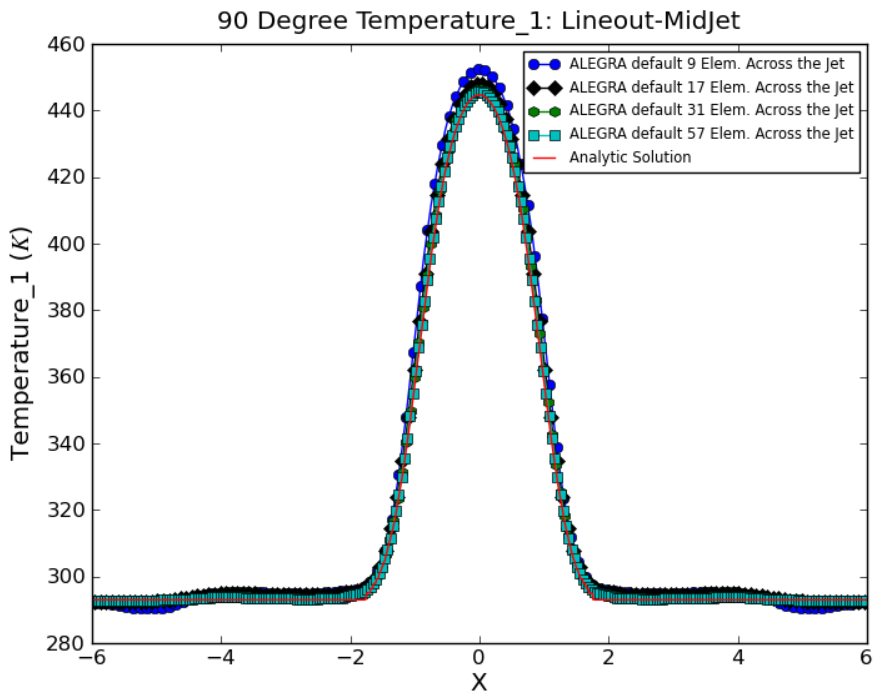

Figure 4.6. $\beta = 90°$: Temperature lineout in the middle of the jet for various mesh resolutions.

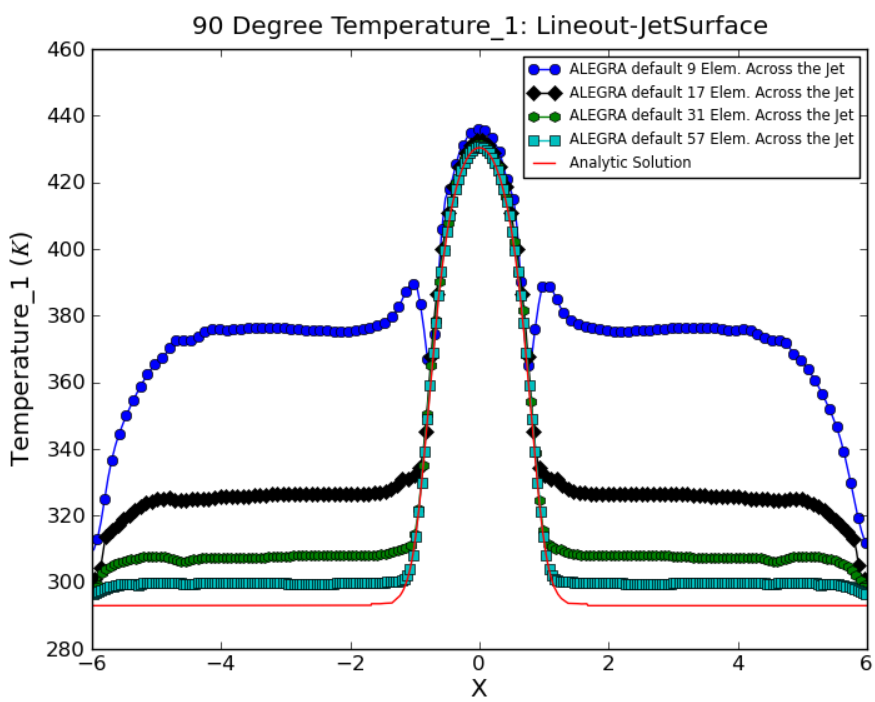

Figure 4.7. $\beta = 90°$: Temperature lineout on the jet surface for various mesh resolutions. Compare with Figure 4.2, 8.1, and 9.1.

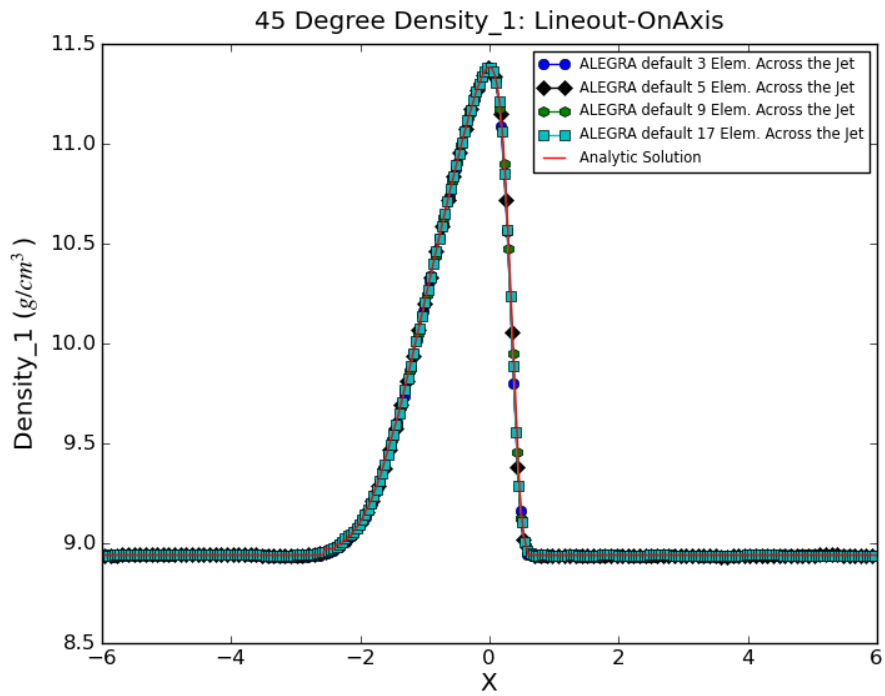

Figure 4.8. $\beta = 45°$: Density lineout on the axis for various mesh resolutions.

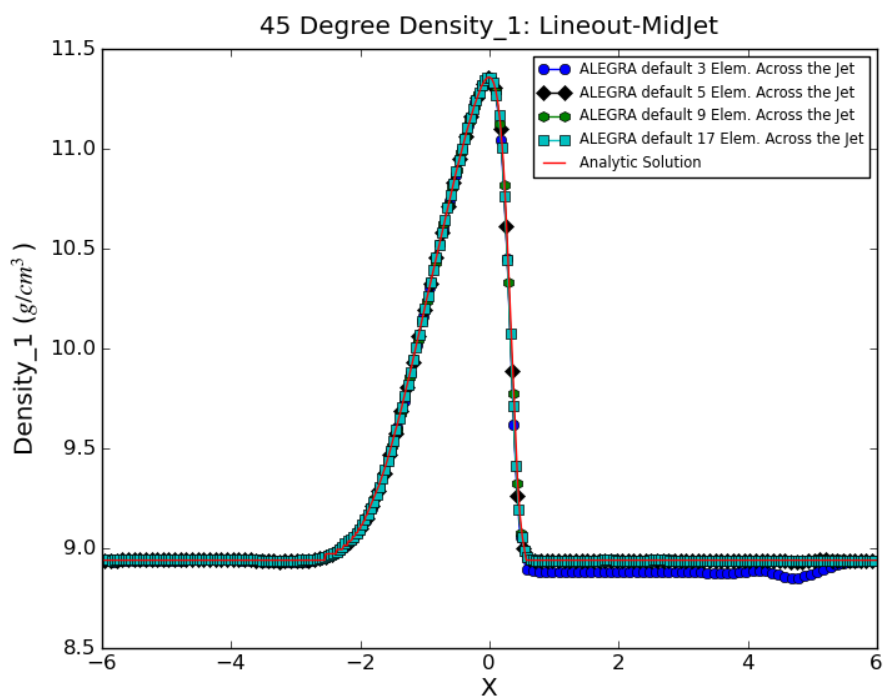

Figure 4.9. $\beta = 45°$: Density lineout in the middle of the jet for various mesh resolutions.

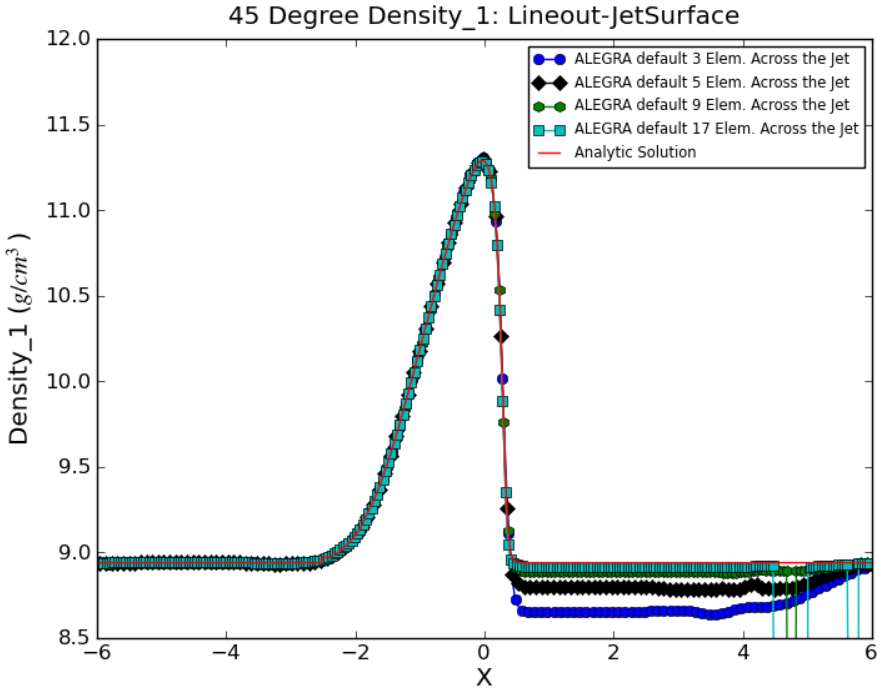

Figure 4.10. $\beta = 45°$: Density lineout on the jet surface for various mesh resolutions. Compare to Figure 9.2.

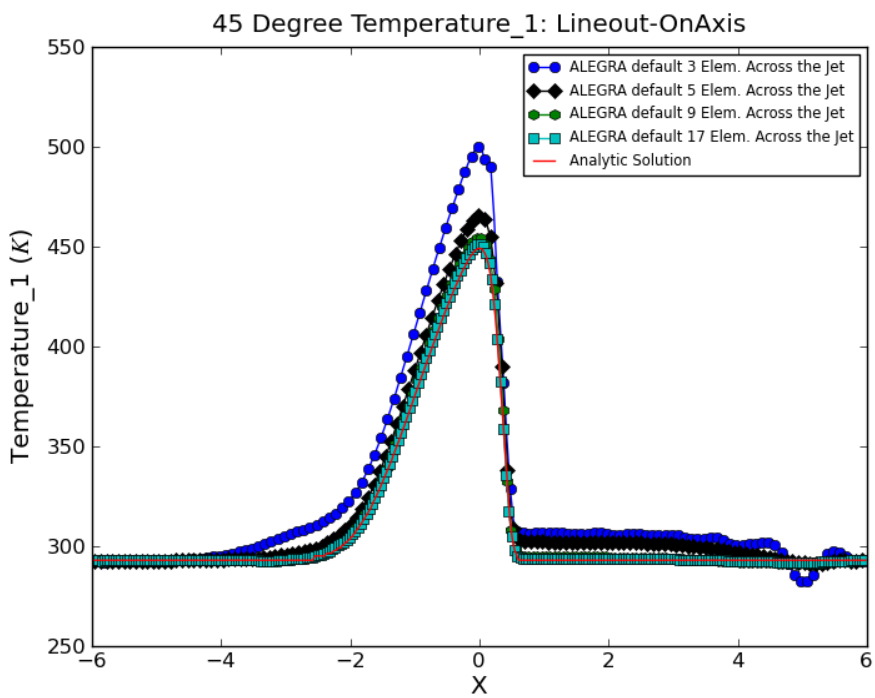

Figure 4.11. $\beta = 45°$: Temperature lineout on the axis for various mesh resolutions. Compare with Figure 8.4, 9.3, and 10.3.

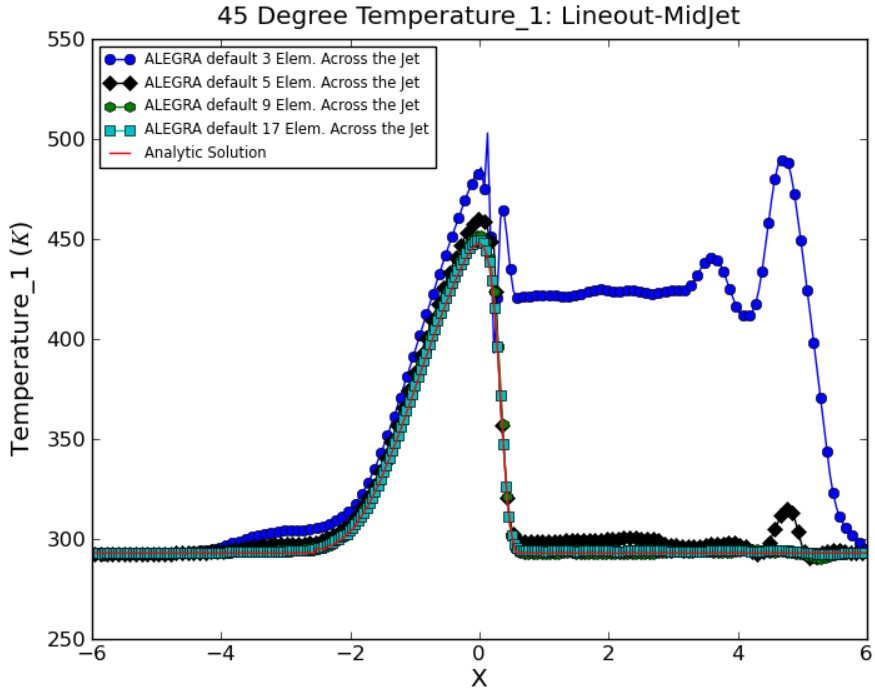

Figure 4.12. $\beta = 45°$: Temperature lineout in the middle of the jet for various mesh resolutions. Compare with Figure 8.5, 9.4, and 10.4.

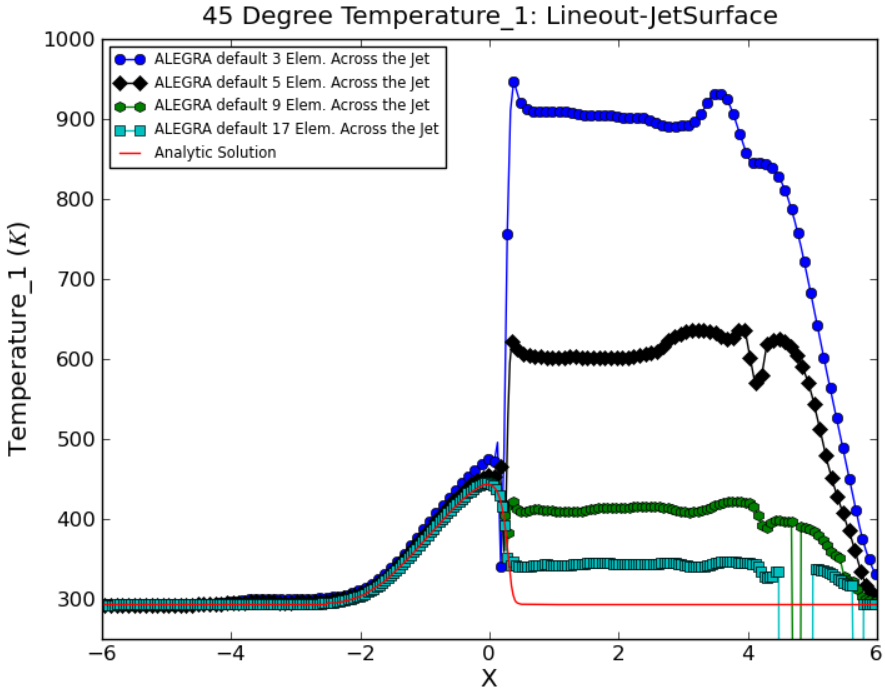

Figure 4.13. $\beta = 45°$: Temperature lineout on the jet surface for various mesh resolutions. Compare with Figures 4.4, 8.6, 9.5, and 10.5.

Chapter 5

Artificial Viscosity

The shaped charge test problem posed provides computational difficulties related to shock capturing codes. With an inflow velocity just under the sound speed and an initial exact steady state profile which is fully subsonic, no shock waves should be produced. However it is possible that the high compression at low resolution may appear to the hydrocode algorithm as a shock and thus additional entropy could be added through the artificial viscosity terms. Advanced artificial viscosity algorithms might be able to provide better control of nonphysical numerical dissipation.

Artificial viscosity algorithms in ALEGRA are tested for improvement of their ability to correctly handle the shockless isentropic flow. Better algorithms should be more proficient at differentiation between shocks and non-shock compression. Artificial viscosity works by smoothing out discontinuities caused by shocks through dissipative processes which add entropy [37]. The default artificial viscosity is tested along with two other options called the limiter and hyperviscosity. The limiter works to monitor the artificial viscosity and reduce or turn off its effects when the artificial viscosity may be unnecessary. In this case, where no shocks should occur, the limiter should reduce any negative effects of the artificial viscosity such as added entropy. Hyperviscosity is an option designed to be utilized together with the limiter. Hyperviscosity is not applied where the lower order artificial viscosity is applied. The use of hyperviscous dissipation helps to control small-scale oscillations [25]. The parameters for both the default artificial viscosity option and utilizing the limiter with hyperviscosity(limhyp) are shown below in Table 5.1.

Default Settings	
Pronto Artificial Viscosity	
Linear	0.15
Quadratic	2.00
Expansion Linear	OFF
Expansion Quadratic	OFF
Limiter	OFF
Hyperviscosity	0.00

Limiter and Hyperviscosity On	
Pronto Artificial Viscosity	
Linear	0.50
Quadratic	1.00
Expansion Linear	ON
Expansion Quadratic	OFF
Limiter	ON
Hyperviscosity	1.00

Table 5.1. Artificial viscosity settings

The limhyp option is intended to be used with the midpoint time integration detailed in Chap-

ter 6. The central difference time integrator is used for the default artificial viscosity settings of ALEGRA. Further analysis of the effects of the time integrators is discussed in Chapter 6.

The main area of focus for analyzing the effects of artificial viscosity is the jet surface. As seen in Chapter 4 the major issues that arise in the test problem are visible through lineouts along the surface of the jet. Figures 5.1 - 5.7 show the comparison between the default and limhyp option for temperature on the axis, in the middle of the jet, and on the jet surface.

Figures 5.1 - 5.3 are plots where $\beta = 90°$. They show that the limhyp has not improved the simulation results when compared with the default settings. Figures 5.1 - 5.3 show how the temperature of the jet is effected based on distance from the axis. For the lineout on the axis (Figure 5.1) and in the middle of the jet (Figure 5.2) the limhyp lineout matches the default and analytic lineout. The lineout on the surface of the jet (Figure 5.3) shows that the limhyp results in yet higher temperatures than the default ALEGRA. The temperature error for the limhyp along the jet surface is nearly twice that of the default settings.

Figures 5.4 - 5.7 are plots where $\beta = 45°$. The density lineout on the jet surface and the temperature lineout on the jet surface, Figures 5.4 and 5.5 respectively, show that the limhyp option makes little to no difference from the default solution errors. The lineouts in the middle of the jet as seen in Figure 5.6 show that the limhyp temperature is slightly greater than the default settings. Figure 5.7 shows that the heating along the surface of the jet decreases when the limhyp option is utilized. While the temperature along the surface of the jet for the limhyp option is less than the default settings it remains significantly higher than the exact solution.

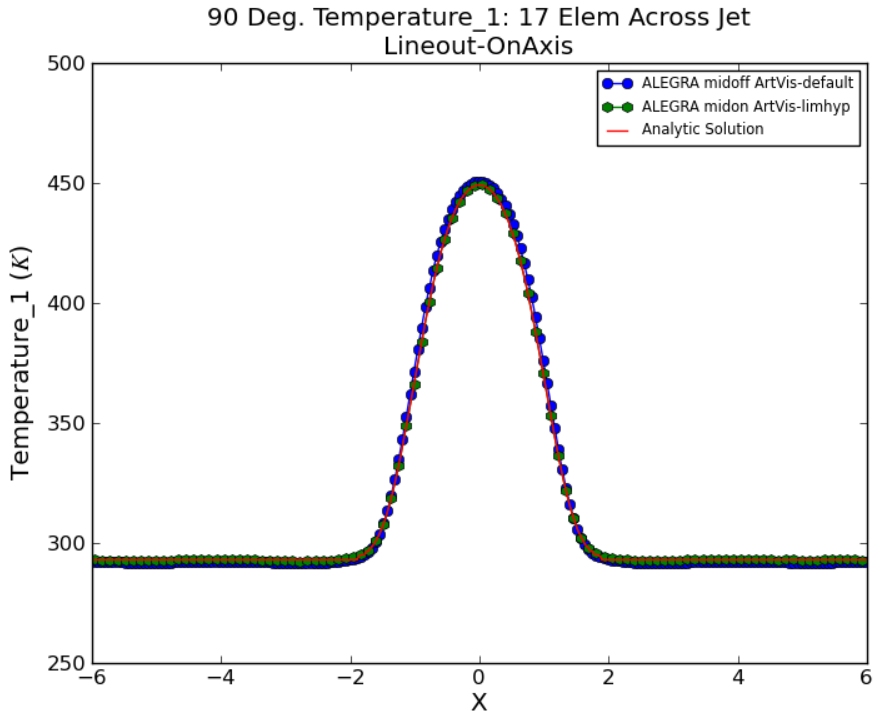

Figure 5.1. $\beta = 90°$: On axis lineout for temperature with 17 elements across the jet testing ALEGRA artificial viscosity.

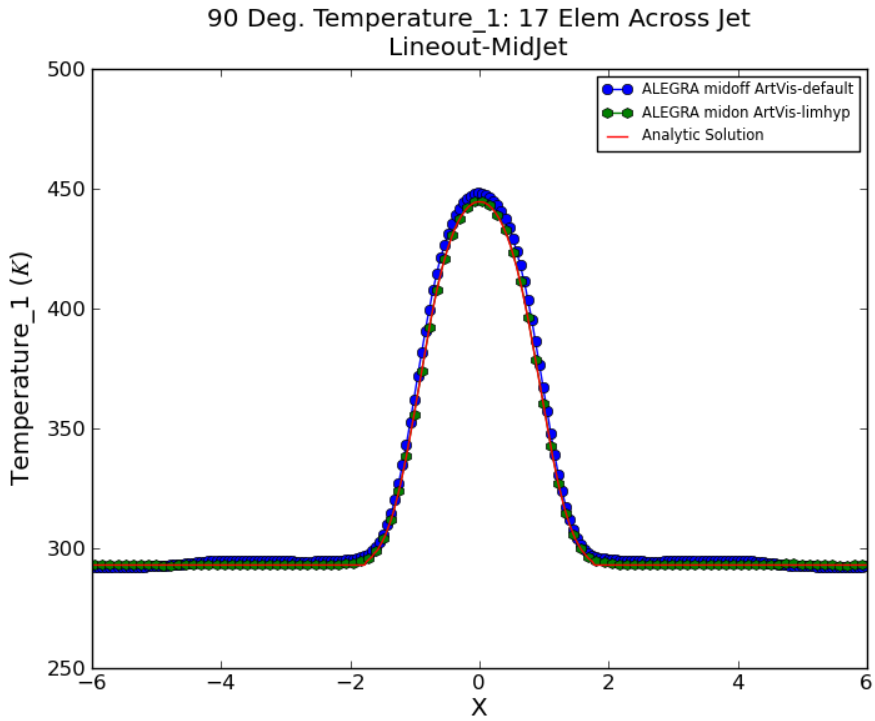

Figure 5.2. $\beta = 90°$: Mid-jet lineout for temperature with 17 elements across the jet testing ALEGRA artificial viscosity.

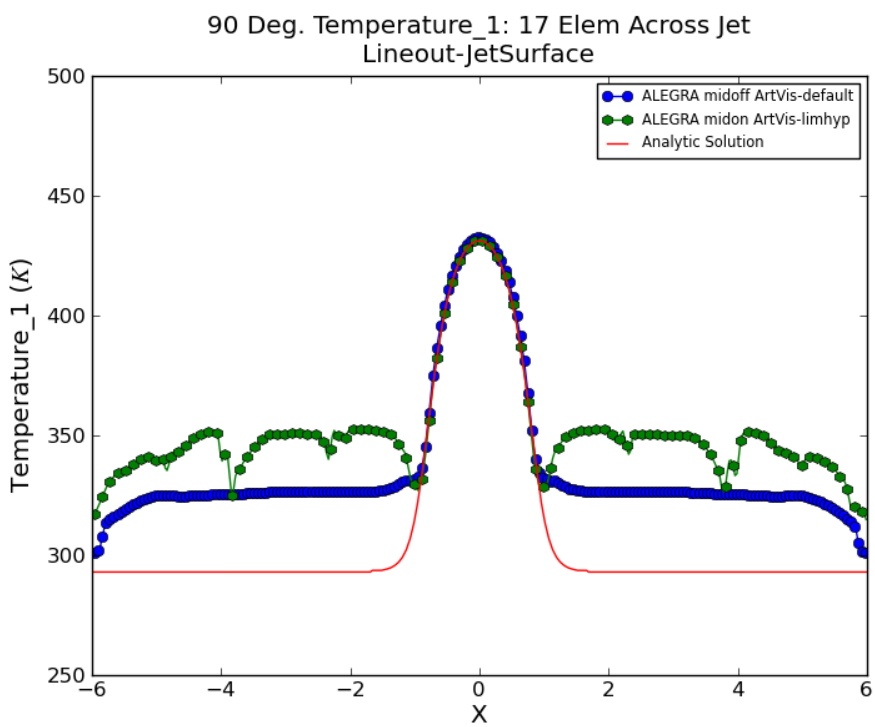

Figure 5.3. $\beta = 90°$: Jet surface lineout for temperature with 17 elements across the jet testing ALEGRA artificial viscosity.

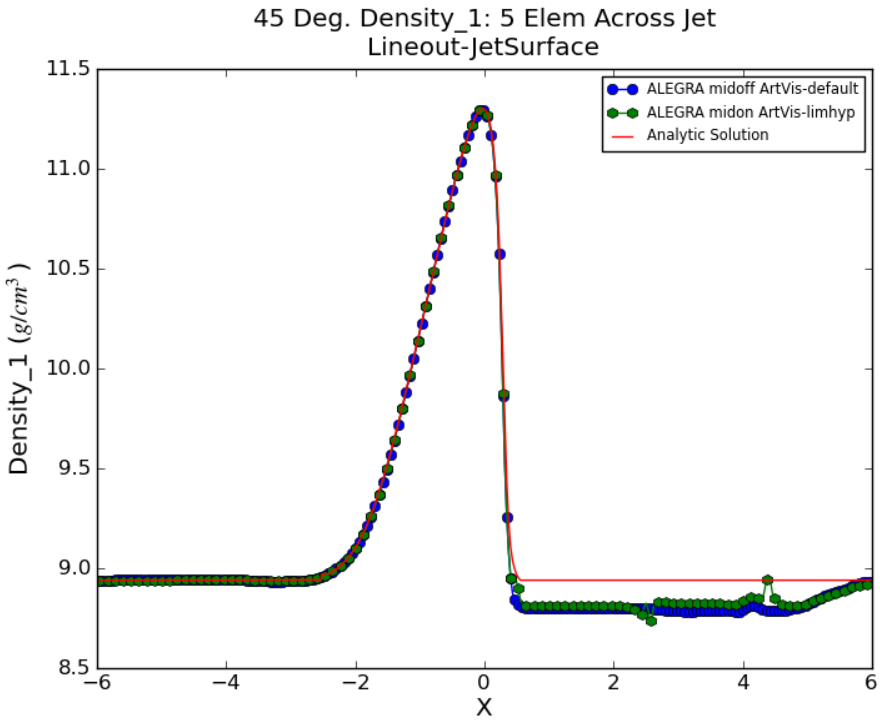

Figure 5.4. $\beta = 45°$: Jet Surface lineout for density with 5 elements across the jet testing ALEGRA artificial viscosity.

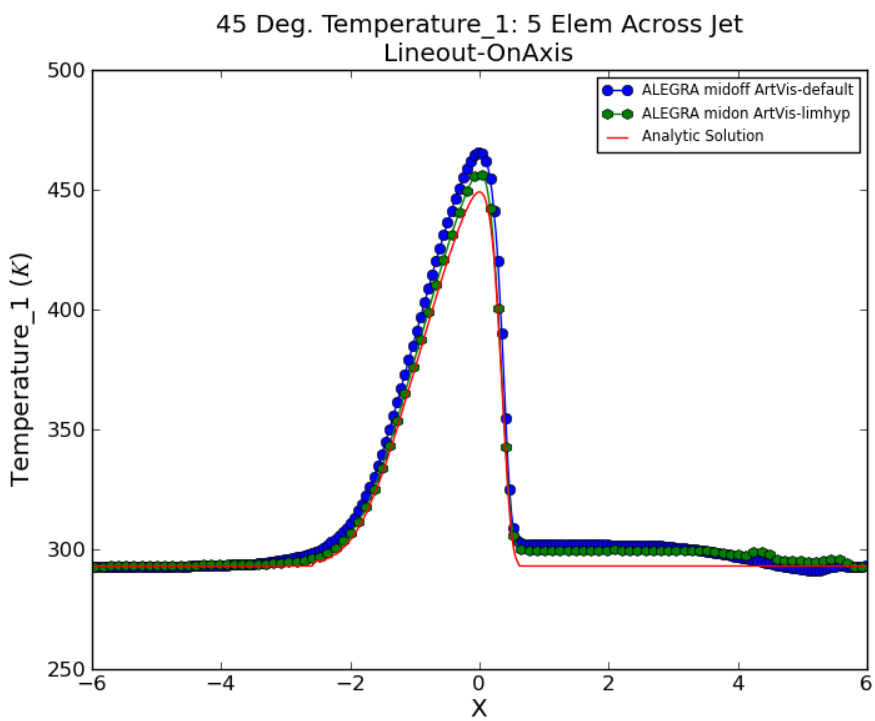

Figure 5.5. $\beta = 45°$: On axis lineout for temperature with 5 elements across the jet testing ALEGRA artificial viscosity.

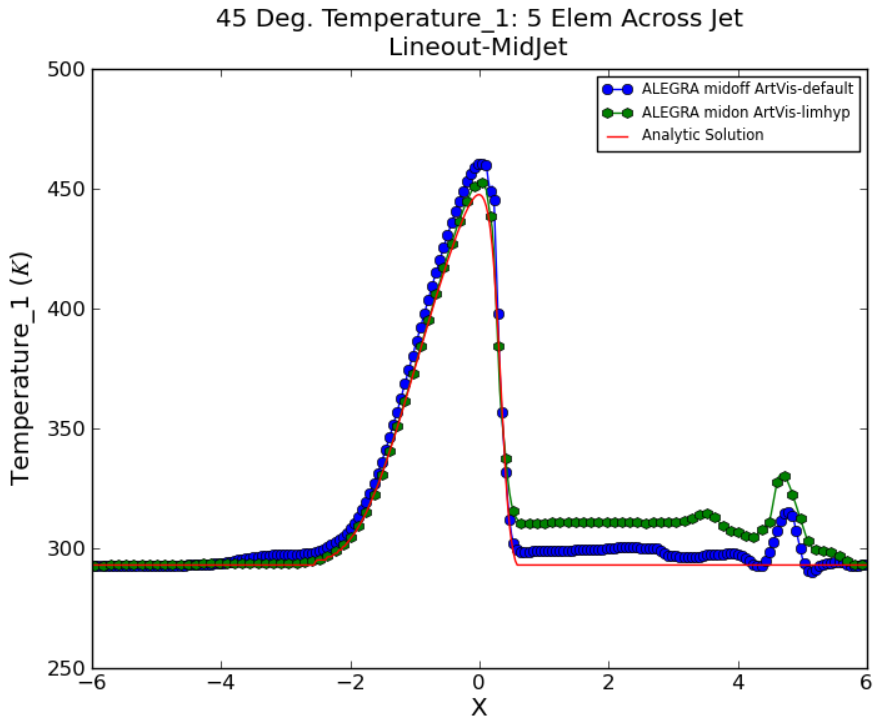

Figure 5.6. $\beta = 45°$: Mid-jet lineout for temperature with 5 elements across the jet testing ALEGRA artificial viscosity.

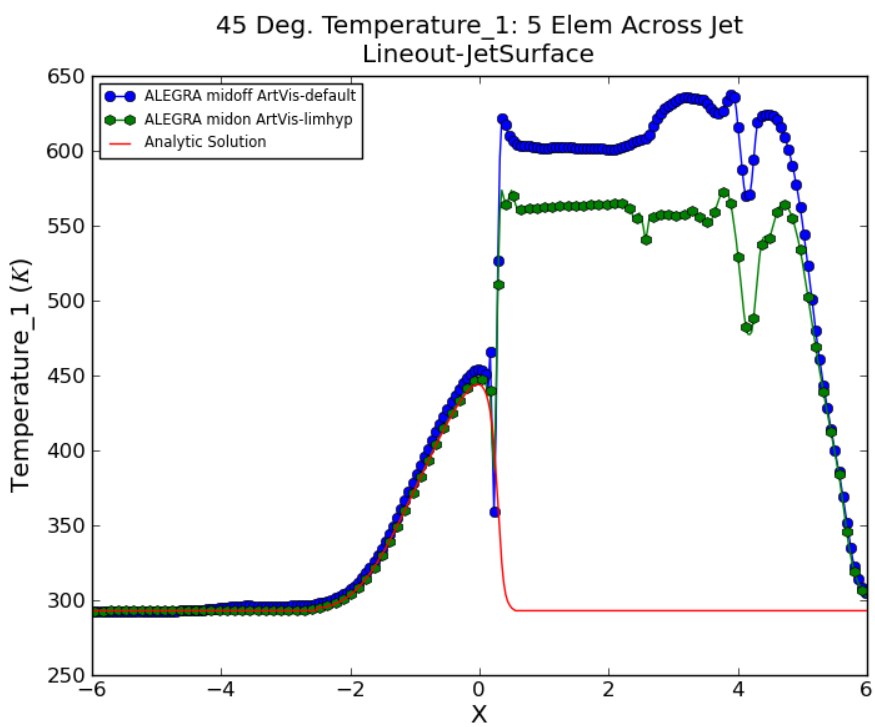

Figure 5.7. $\beta = 45°$: Jet surface lineout for temperature with 5 elements across the jet testing ALEGRA artificial viscosity.

Chapter 6

Time Integration

There are two time integration methods currently available in ALEGRA for the Lagrangian step. The current ALEGRA default method is the central-difference time integrator. Central-difference is a second order algorithm commonly used for structural dynamics calculations which do not include the energy equation. Since ALEGRA must capture shocks, a solution of the energy equation is required as well. The current default algorithm is energy-conservative but is unfortunately overall only first order accurate and numerically unstable in expansion. The alternative predictor-corrector or midpoint method is approximately twice as expensive as central-difference in the ALEGRA Lagrangian step. It is however fully second-order accurate in time and stable. Stability analysis of the midpoint time integrator is discussed in [17]. The midpoint method is slated to become the default time integrator for ALEGRA simulations.

The midpoint time integrator results are compared against the central-difference time integrator using both the default settings of ALEGRA and the limhyp option. For $\beta = 90°$, the lineout on the jet surface is the only location where a difference between the midpoint and central-difference time integrators is seen. Figure 6.1 shows plots of temperature lineouts for this case. From this figure, midpoint appears to have no effect relative to the default settings of ALEGRA. The default settings for midpoint and central-difference overlap one another almost completely. The limhyp option with the midpoint time integrator slightly lowers the temperature on the jet surface. The simulations where $\beta = 45°$ show greater deviation from the analytic solution than $\beta = 90°$ when comparing the time integrators.

Figures 6.2 - 6.4 are temperature lineouts which show the effects of midpoint and central-difference time integration where $\beta = 45°$. Similar to $\beta = 90°$, midpoint time integration does not appear to introduce any variation from the central difference time integrator except for minor changes in temperature along the jet. Figure 6.2 shows the temperature along the axis. The midpoint time integrator appears to have minimal effect on both the default and limhyp options. Figure 6.3 shows the results for temperature along the middle of the jet. In this plot none of the settings overlap completely and they are progressively worse in the following order: default settings with midpoint-off, limhyp with midpoint-off, default settings with midpoint-on, limhyp with midpoint-on. Thus from this plot the midpoint time integrator has slightly worsened the results. Figure 6.4 shows that the midpoint option has had similar results on the surface of the jet as in the middle of the jet. The temperatures are slightly higher with midpoint than central difference. Slight variations are seen between the midpoint and central difference time integrators but the variations are insignificant overall.

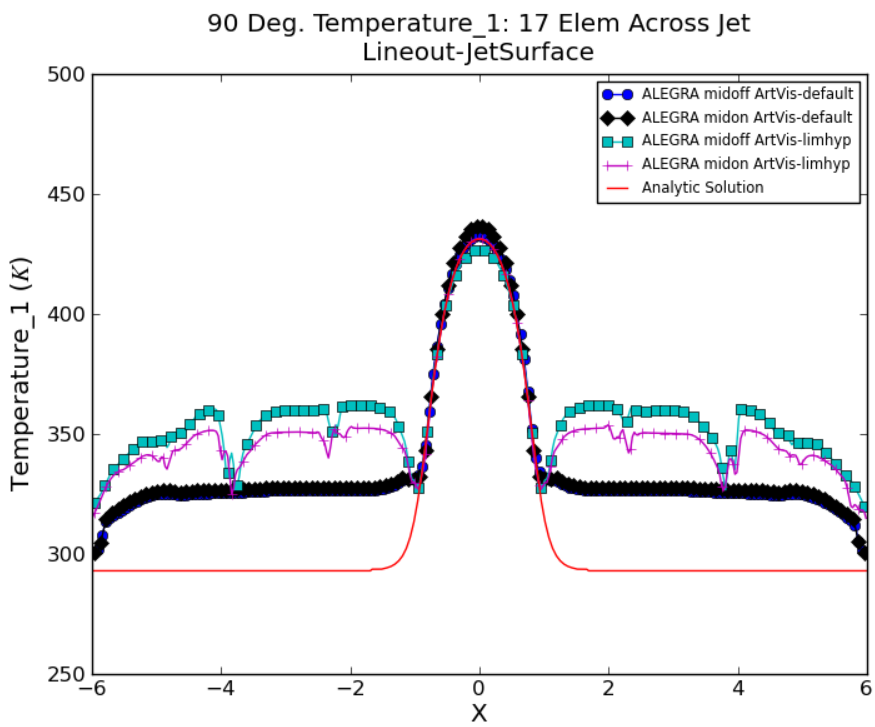

Figure 6.1. $\beta = 90°$: Jet surface lineout for temperature with 17 elements across the jet to show the effects of midpoint.

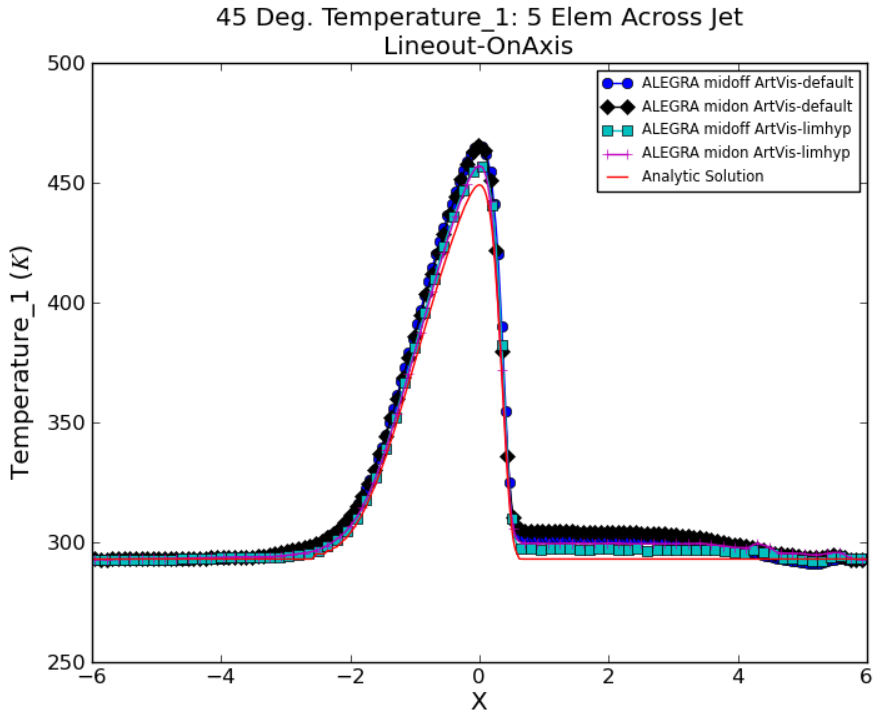

Figure 6.2. $\beta = 45°$: On axis lineout for temperature to show the effects of midpoint. Compare with Figure 10.6.

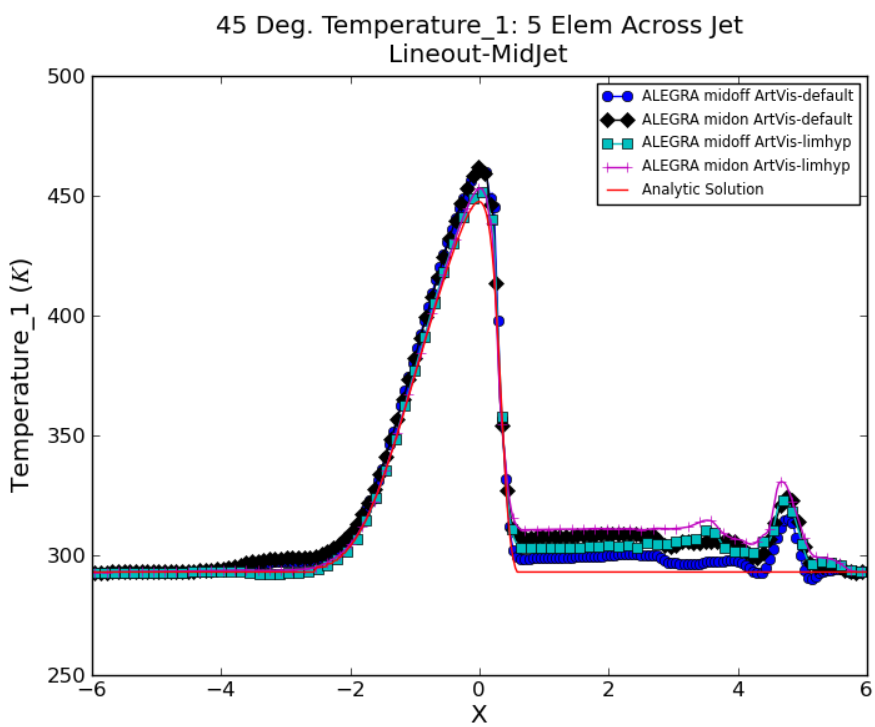

Figure 6.3. $\beta = 45°$: Mid-jet lineout for temperature to show the effects of midpoint. Compare with Figure 10.7.

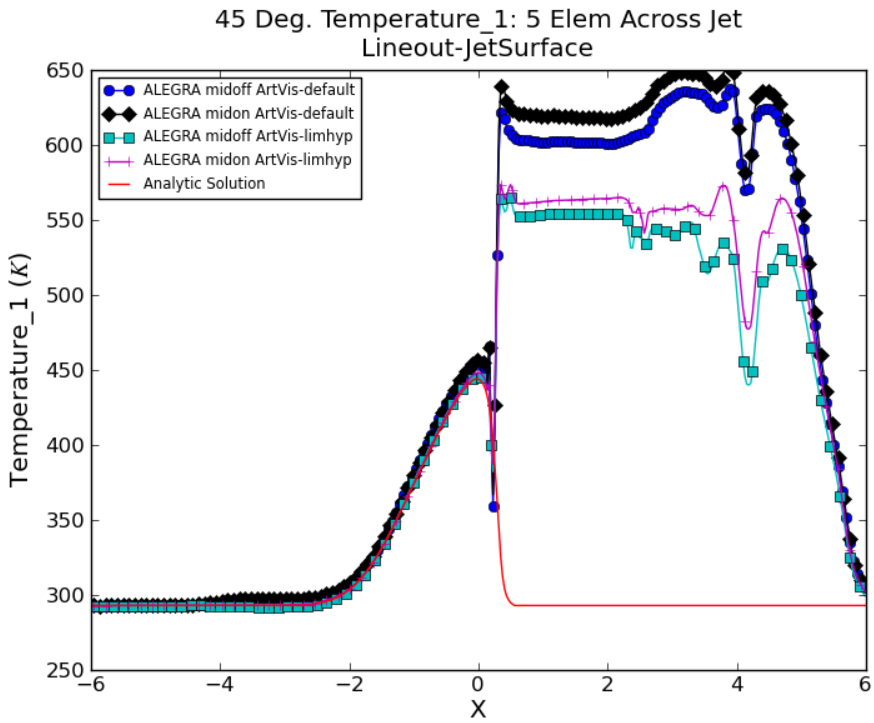

Figure 6.4. $\beta = 45°$: Jet surface lineout for temperature to show the effects of midpoint. Compare with Figure 10.8.

Chapter 7

DeBar Advection

DeBar Energy Advection is an optional algorithm implemented in ALEGRA which conserves total energy [30, 29]. The DeBar method remaps the kinetic energy, then adds the difference between the remapped kinetic energy and the kinetic energy computed after the momentum remap to the internal energy. The advection option does have the possibility of creating anomalously cold regions or hot regions due to truncation errors but has shown excellent results with some shock simulations. The DeBar method as implemented also includes an option intended to reduce the negative effects of applying the full algorithm everywhere.

The challenge for the DeBar type of algorithm is to provide for high quality shock simulations while still retaining thermodynamic robustness. The DeBar method will only be implemented when the code finds a shock with a Q/p value greater than the value specified in the input deck, where Q represents the artificial viscosity and p represents the pressure. If no value is specified, a default value of 0.0 is used and the DeBar method does not respect the size of the shock. The plots in this chapter are run with the default DeBar energy advection.

Large errors are seen with the DeBar option where $Q/p = 0.0$ including cooling anomalies along the inflow and heating errors along the jet for both $\beta = 90°$ and $45°$. Errors became so large for the limhyp option with central-difference time integration that the simulation failed. Figures 7.1 - 7.3 shows the lineouts for temperature along the jet where $\beta = 90°$. While the lineout along the jet surface (Figure 7.3) continues to show the worst errors, the on-axis and mid-jet lineouts show heating that propagates from the stagnation point (Figures 7.1 and 7.2 respectively).

Common to previous chapters, the errors seen for $\beta = 45°$ are worse. Figures 7.4 - 7.7 show the lineouts for density on the jet surface and temperature lineouts in the jet. Figure 7.4 shows that the drop in density is worse than shown in previous chapters. The temperature lineouts also continue to show similar issues as seen in previous chapters with greater errors. The temperature plots show that none of the various options seem to make much difference with DeBar on. All lines in the plots follow the same general path. The negative effects from DeBar at the stagnation point are now large enough to cause errors in the slug. Figure 7.5 shows a decrease in temperature on the axis near the stagnation point.

Various values of Q/p are used and show that as Q/p increases, the effect from the DeBar method decreases. The values include 1×10^{-4}, 1×10^{-2}, 1×10^{-1}, and 5×10^{-1}. The extreme negative effects shown in the plots of this chapter occur with values 1×10^{-4} and 1×10^{-2}. Larger values slightly improve the results but only continue to improve until the DeBar method is com-

pletely off and the results are the similar to the default ALEGRA code from Chapter 4. Therefore the DeBar method only has negative effects for this test problem.

The large negative effect that this algorithm causes on this relatively benign quasi-isentropic flow is perhaps indicative of a fundamental implementation error of some sort. A thorough review of this algorithm is therefore called for.

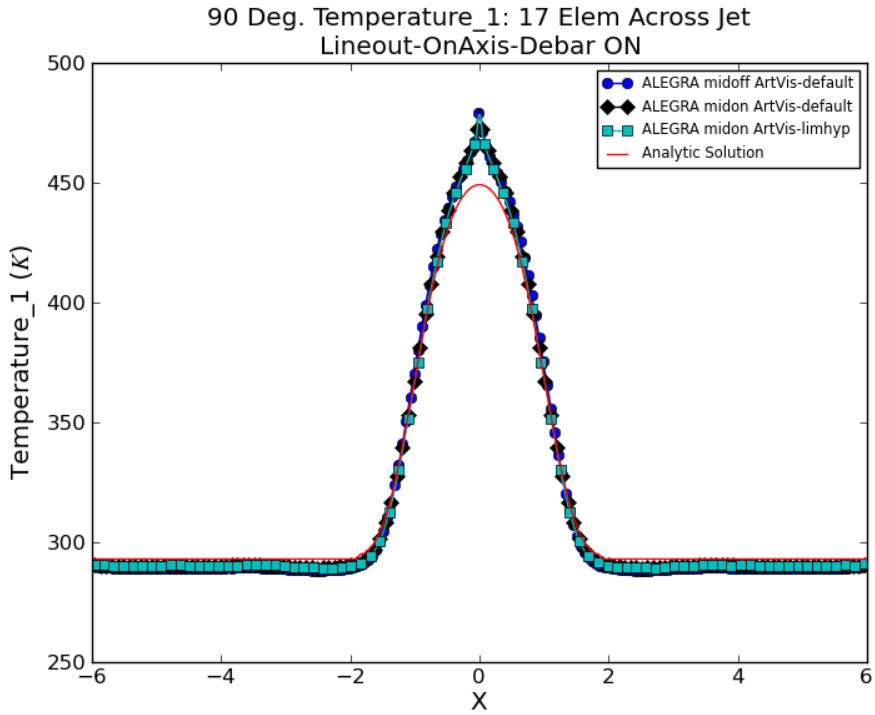

Figure 7.1. $\beta = 90°$: On axis lineout for temperature with 17 elements across the jet showing results from DeBar energy advection.

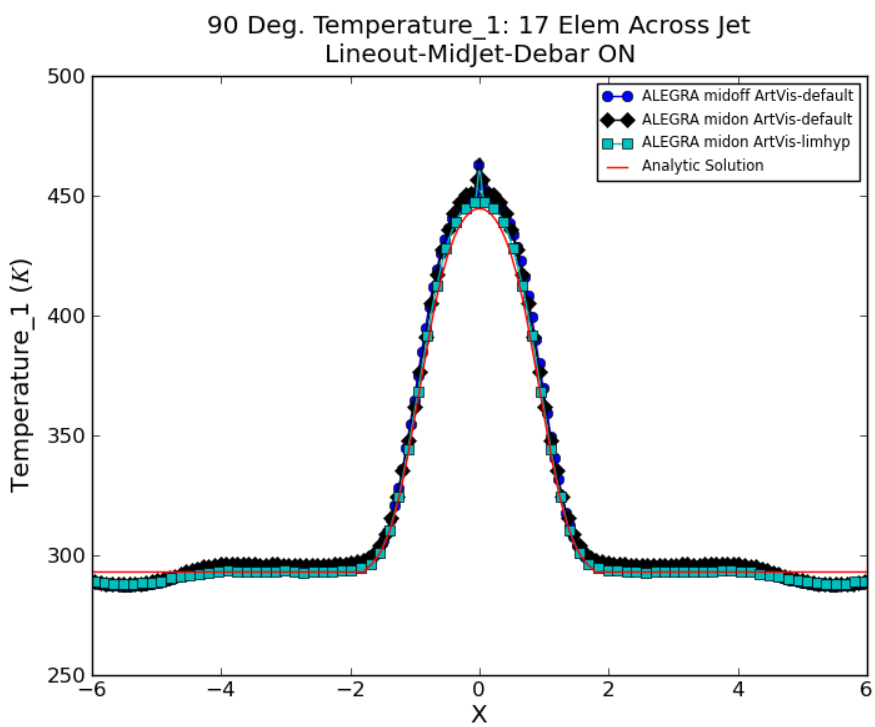

Figure 7.2. $\beta = 90°$: Mid-Jet lineout for temperature with 17 elements across the jet showing results from DeBar energy advection.

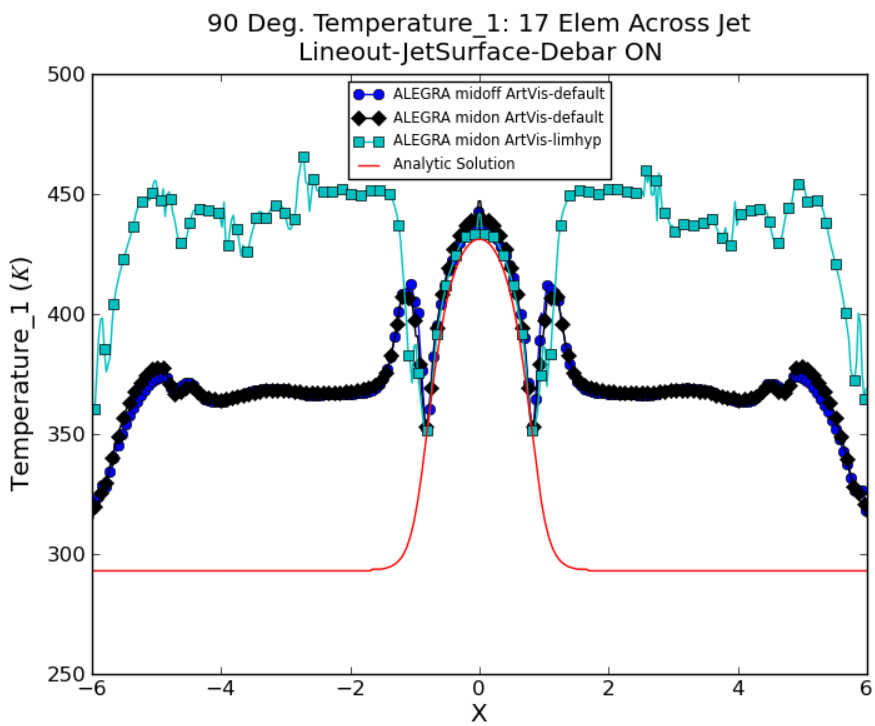

Figure 7.3. $\beta = 90°$: Jet surface lineout for temperature with 17 elements across the jet showing results from DeBar energy advection.

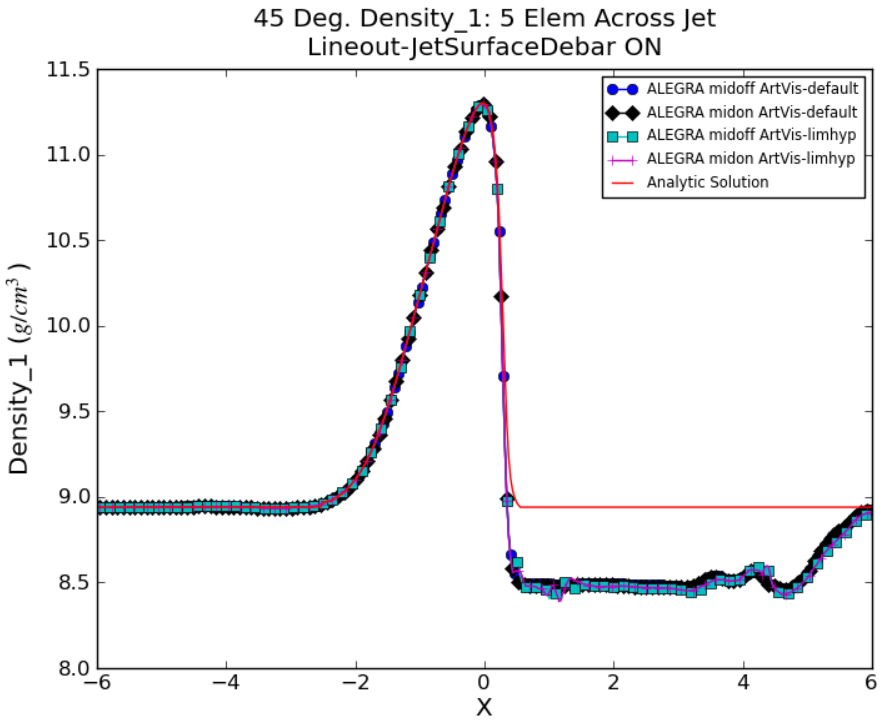

Figure 7.4. $\beta = 45°$: Jet surface lineout for density with 5 elements across the jet showing results from DeBar energy advection.

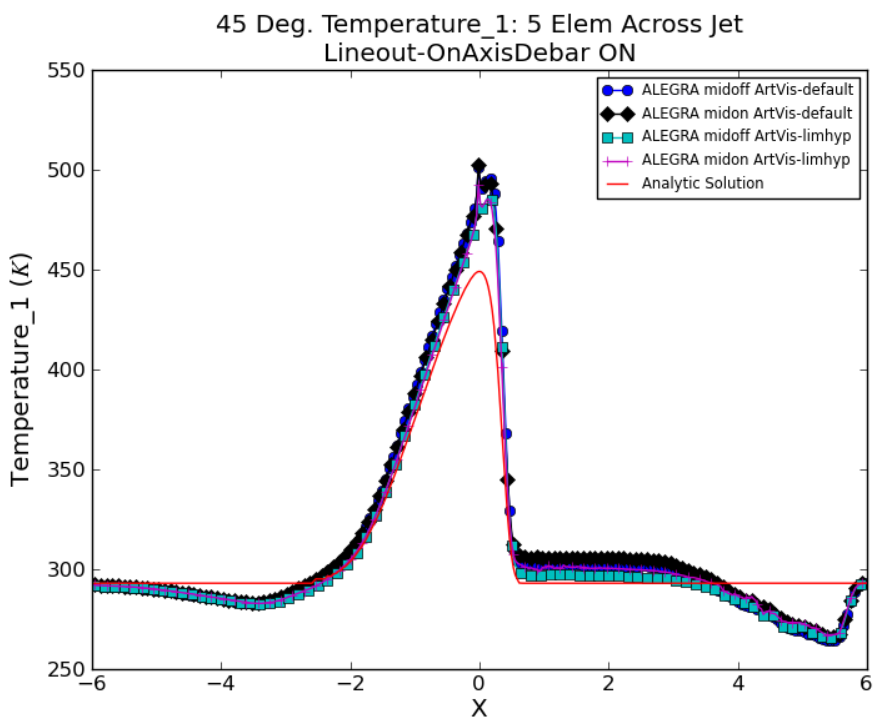

Figure 7.5. $\beta = 45°$: On axis lineout for temperature with 5 elements across the jet showing results from DeBar energy advection.

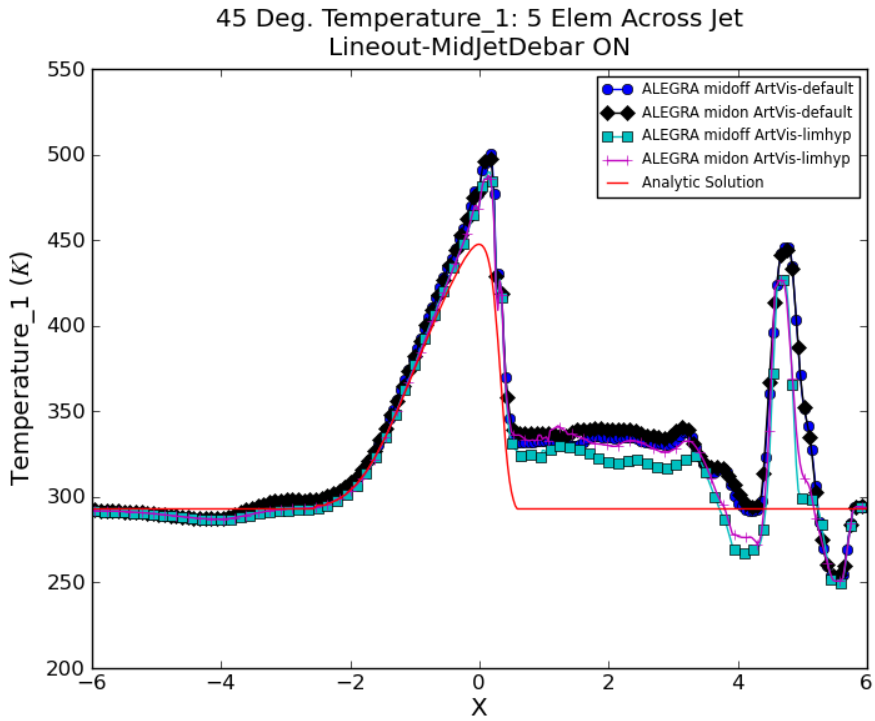

Figure 7.6. $\beta = 45°$: Mid-Jet lineout for temperature with 5 elements across the jet showing results from DeBar energy advection.

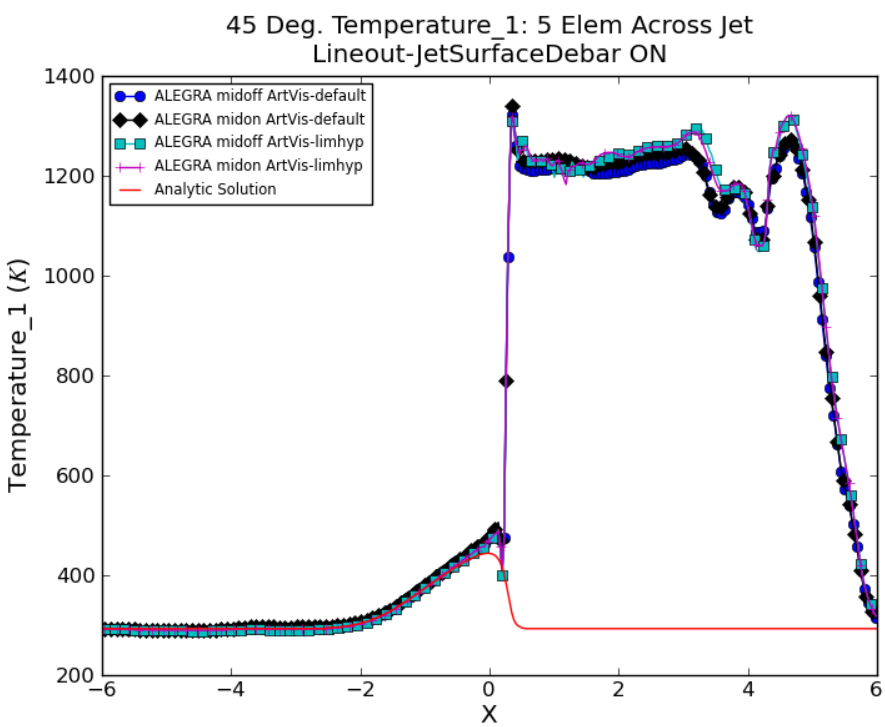

Figure 7.7. $\beta = 45°$: Jet Surface lineout for temperature with 5 elements across the jet showing results from DeBar energy advection.

Chapter 8

Extended Finite Element Method (XFEM)

The extended finite element method (XFEM) in ALEGRA was developed in order to achieve better sub-cell resolution for multi-material elements. It is conceivable that the issues that occur in multi-material elements in general and specifically on a material void interface as in the jet problem may be totally sidestepped using this algorithm. The standard finite element method (FEM) basically binds two materials together and modeling deficiencies occur when two materials experience contact, slide past one another, or must release from each other. The modeling issue is caused by the singular, continuous velocity field of the FEM [36]. One can speculated that the anomalous heating issues visible in ALEGRA are caused by the interface between a material and void. In the shaped charge test problem this interface lies between the void background and copper jet where the significant anomalous heating of the jet surface material occurs. The XFEM algorithm could reduce the heating by its detailed treatment of the surface interaction. Originally XFEM was used to model crack propagation and has since been implemented in ALEGRA as a new algorithm underdevelopment for treating grain boundaries and dealing with multi-material elements [27]. ALEGRA uses pattern interface reconstruction with a volume-of-fluid based method together with the XFEM to improve these interactions [8, 9]. This test problem utilizes the XFEM in ALEGRA to assist in testing this emerging capability.

As with other capabilities tested, where $\beta = 90^\circ$, the XFEM algorithm appears to have a minimal effect. Figure 8.1 shows that the XFEM simulation results are similar to the default settings of ALEGRA as seen in Figure 4.7. There is an increase in temperature near the stagnation point and along the jet surface for each resolution. Another change from the default settings are the smoothness of the plots seen in the XFEM results. Particularly at high resolution, waves have developed in the lineouts which may possibly be due to numerical instabilities.

This subtle instability is a new problematic issue seen in the XFEM simulations. The issue is represented by the development of a coarseness or waves associated with the plots. The default settings of ALEGRA are quite stable and smooth while the XFEM plots exhibit instabilities that seem to worsen with increasing resolution. This is clearly visible in Figures 8.2 and 8.3 which show the simulation at 11μs for the default and XFEM settings respectively. It is also visible in the resolution plots of this chapter as compared to the smooth plots from Chapter 4. The vertical lines seen in Figures 8.1 and 8.6 represent small break-ups of the copper jet along its surface caused by these instabilities. After further analysis, these instabilities appear to be related to the relatively new 2nd order remap option associated with the XFEM. Reducing the remap to first order removes the waves and instabilities yet the 2nd order remap is essential for reducing the anomalous heating

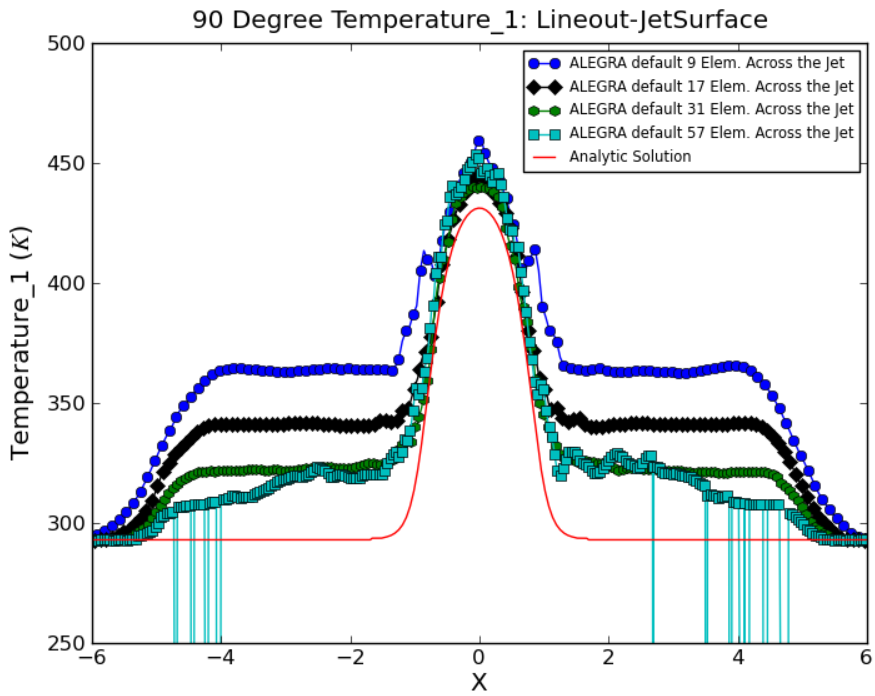

Figure 8.1. $\beta = 90°$: Temperature lineout on the jet surface for the XFEM in ALEGRA. Compare to Figure 4.7.

along the jet surface.

Figures 8.4 - 8.6 show the results of temperature lineouts for $\beta = 45°$. The temperature lineout on the axis in Figure 8.4 is compared with Figure 4.11. The XFEM simulation is not as accurate on the axis. In Figure 4.11 the lower resolution plots show some heating near the stagnation point and higher resolution plots follow the analytic solution very well. The XFEM results in Figure 8.4 appear wavy and there is more heating near the stagnation point. Even the higher resolution plots do not return to the correct temperature value along the jet.

The lineout for temperature through the middle of the jet as seen in Figure 8.5 may be compared with Figure 4.12. All errors for the temperature lineout on the axis are amplified in this plot. The results appear rough or coarse from instabilities or waves propagating through the solution. The heating near the stagnation point has also worsened for each mesh resolution. Even a very refined mesh such as 17 elements across the jet does not match the temperature of the analytic solution along the jet.

The XFEM has a significant effect on the shaped charge test problem at the jet surface. Figure 8.6 shows the temperature lineout on the jet surface for the XFEM and is compared with Figure 4.13. When comparing the highest resolution mesh, the default settings of ALEGRA match the analytic solution better than the XFEM in ALEGRA. It is the low resolution plots which show

significant improvement over the default settings in ALEGRA. With only 3 and 5 elements across the jet the XFEM in ALEGRA greatly reduces the heating as compared to the default settings of ALEGRA.

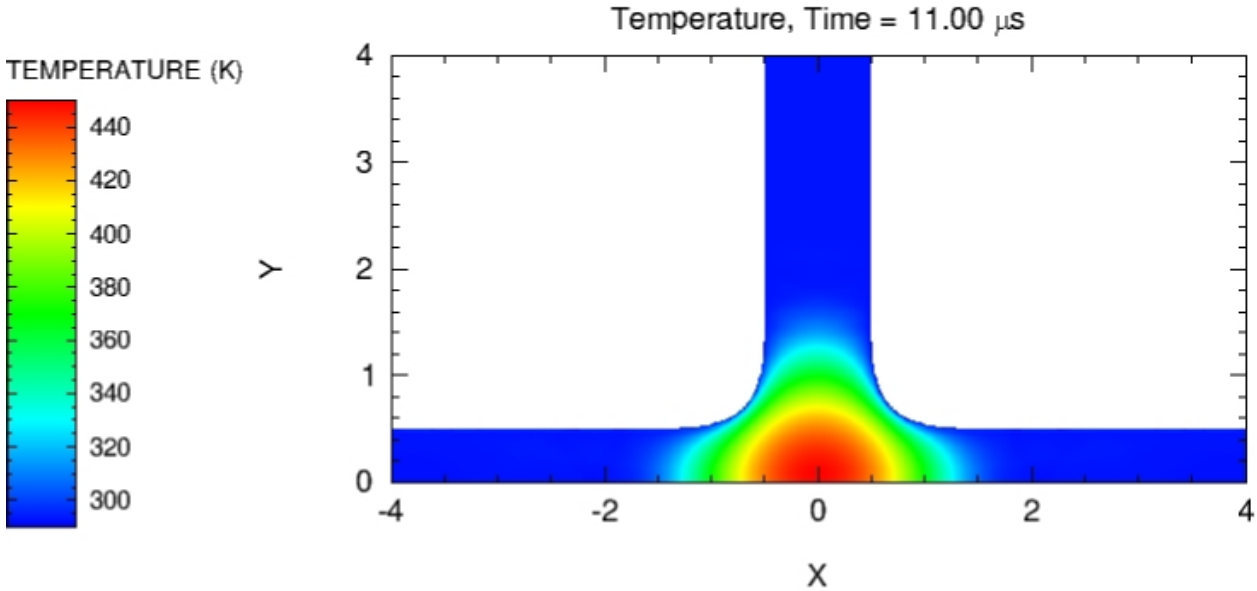

Figure 8.2. $\beta = 90°$: Temperature plot at $11\mu s$ for the default settings of ALEGRA.

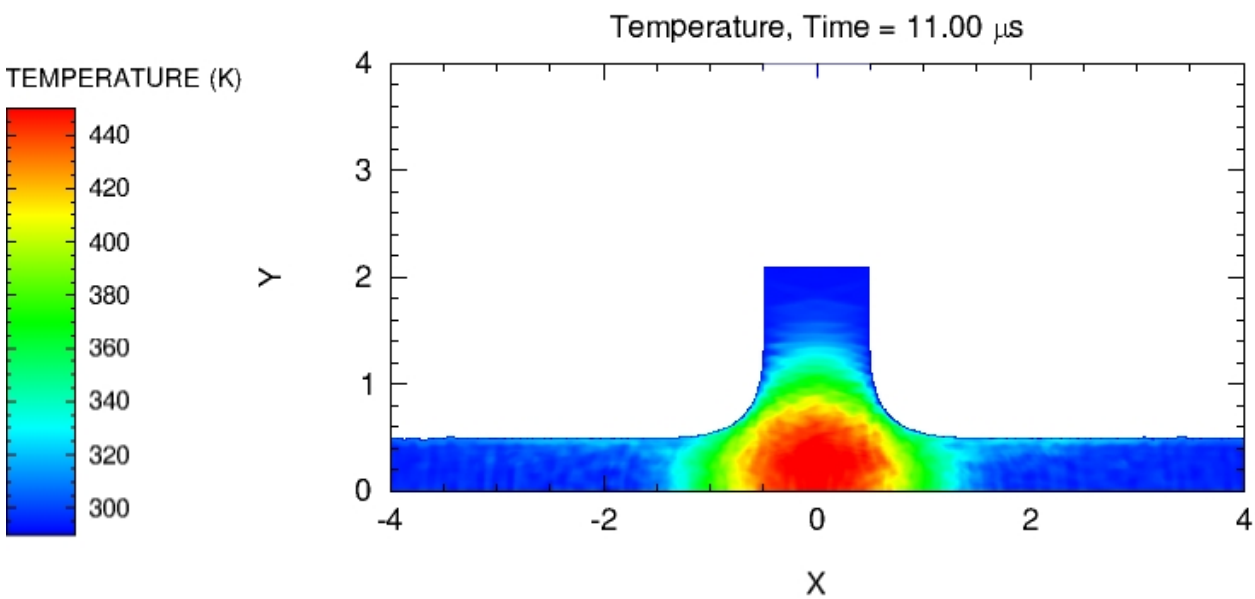

Figure 8.3. $\beta = 90°$: Temperature plot at $11\mu s$ for the XFEM in ALEGRA.

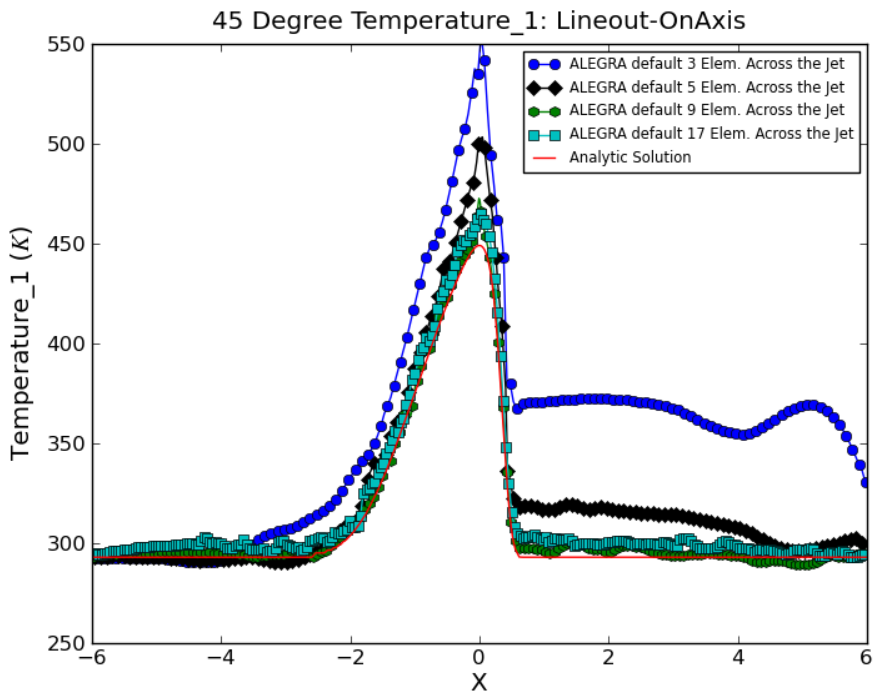

Figure 8.4. $\beta = 45°$: Temperature lineout on the axis for the XFEM in ALEGRA. Compare to Figure 4.11.

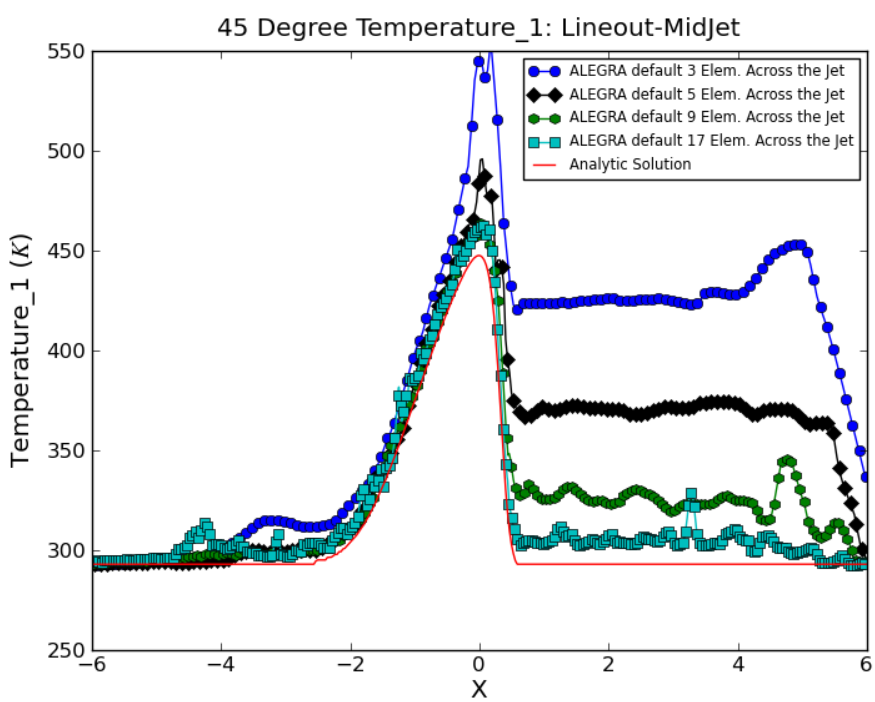

Figure 8.5. $\beta = 45°$: Temperature lineout in the middle of the jet for the XFEM in ALEGRA. Compare to Figure 4.12.

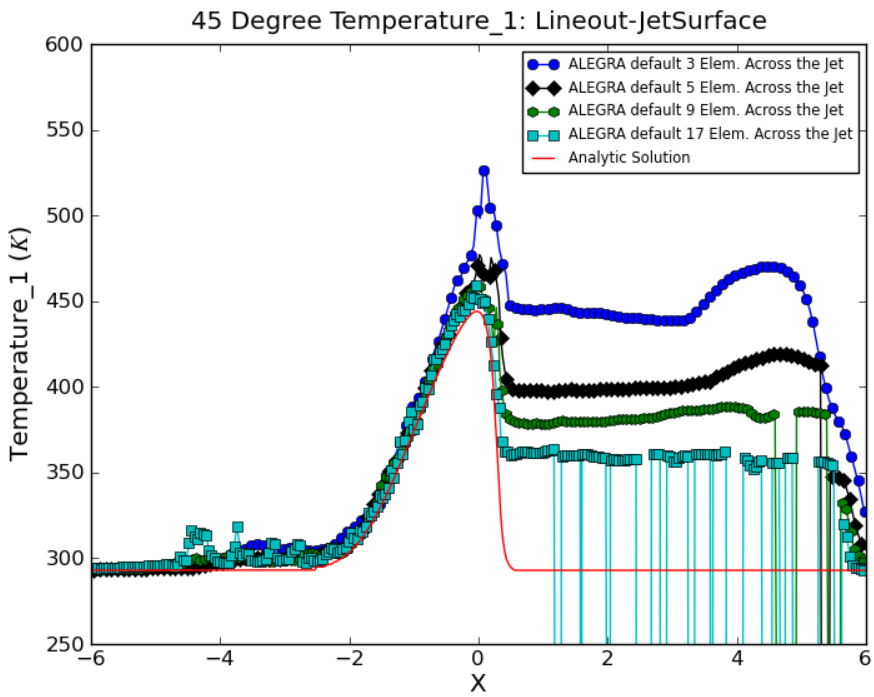

Figure 8.6. $\beta = 45°$: Temperature lineout on the jet surface for the XFEM in ALEGRA. Compare to Figure 4.13.

Chapter 9

CVFA and IMMA Mixed Material/Void

The XFEM simulations from Chapter 8 appear to be the best for reducing the heat along the surface of the jet. This suggests that an algorithm required by XFEM may be related to this effect of reducing the anomalous heating. The constant volume fraction algorithm (CVFA) and void compression algorithm turned off are possible causes for the heat reduction seen in XFEM. The CVFA was replaced by the isentropic multi-material algorithm (IMMA) as the default in ALEGRA [26]. The CVFA may be used with or without void compression while the user is forced to use the void compression algorithm with the IMMA. These algorithms alter the way void interacts with material in ALEGRA. This chapter provides further testing for issues that may exist on the material/void interface. It focuses on the testing and results of the CVFA and IMMA with and without the void compression algorithm.

Void Compression OFF

When $\beta = 90°$, the CVFA results show subtle improvements from the standard ALEGRA default settings.The temperature lineouts on the axis and in the middle of the jet match the analytic solution as do those associated with the default settings of ALEGRA. Figure 9.1 shows the temperature lineout along the jet surface for the CVFA and is compared with Figure 4.7. The lower mesh resolutions show slight improvements while higher resolutions are practically identical.

When $\beta = 45°$, the CVFA shows more significant results. In Chapter 4 it was shown that the temperatures increased enough along the surface of the jet as to reduce the density. Figure 9.2 shows CVFA results for density on the jet surface that may be compared with Figure 4.10 from Chapter 4. The CVFA results show no drop in density suggesting that the temperature along the jet surface is closer to the analytic solution. Figures 9.3 - 9.5 show the temperature lineouts for the CVFA. For comparison, the results for the default setting are in Figures 4.11 - 4.13. On the jet surface in Figure 9.5, all resolutions have reduced the heating, particularly those of 3 and 5 elements across the jet. In the middle of the jet and on the axis the higher resolution plots, 9 and 17 elements across the jet, are nearly identical between the CVFA and default settings. The lower resolutions on the axis and in the middle of the jet tend to show small variations in heating from the default settings.

The IMMA with void compression off also produces similar results. As seen in Figures 9.6 and 9.7 the heating along the jet has been reduced for both $\beta = 90°$ and $\beta = 45°$ respectively.

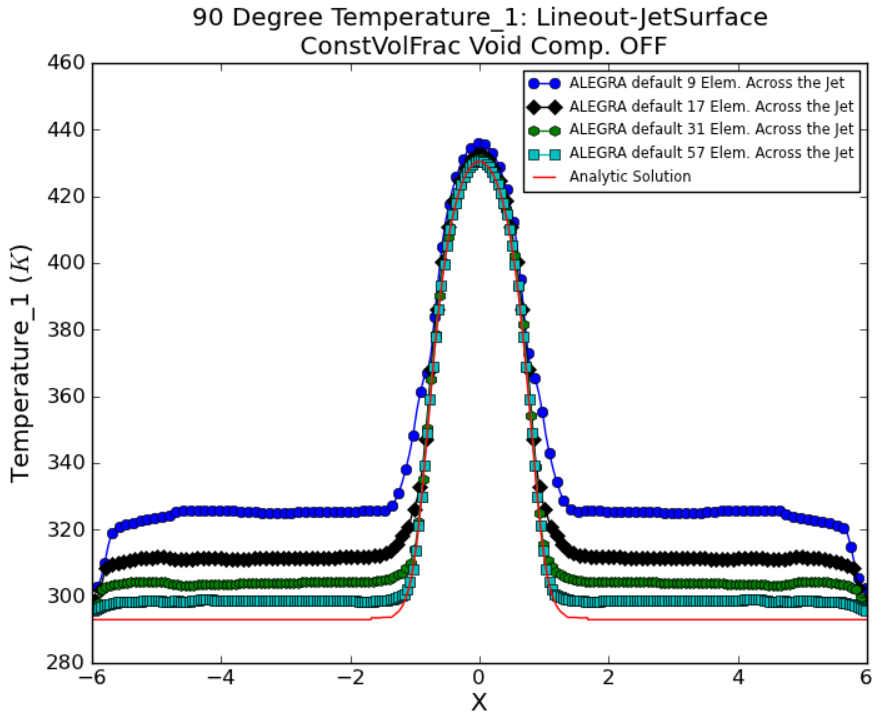

Figure 9.1. $\beta = 90°$: Temperature lineout on the jet surface for the CVFA. Compare with Figure 4.7 and 9.8.

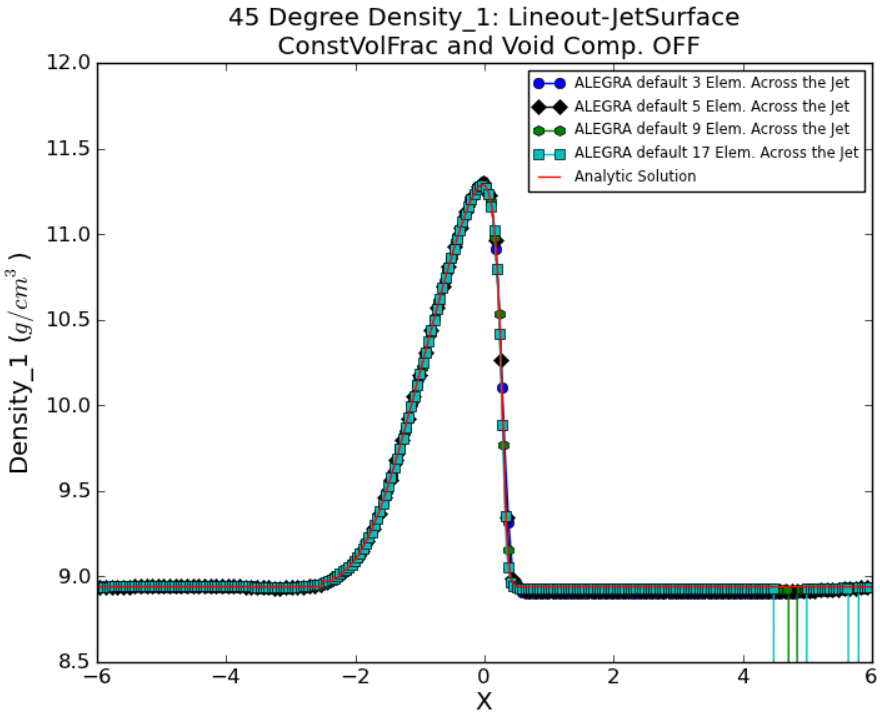

Figure 9.2. $\beta = 45°$: Density lineout on the jet surface for the CVFA. Compare with Figure 4.10.

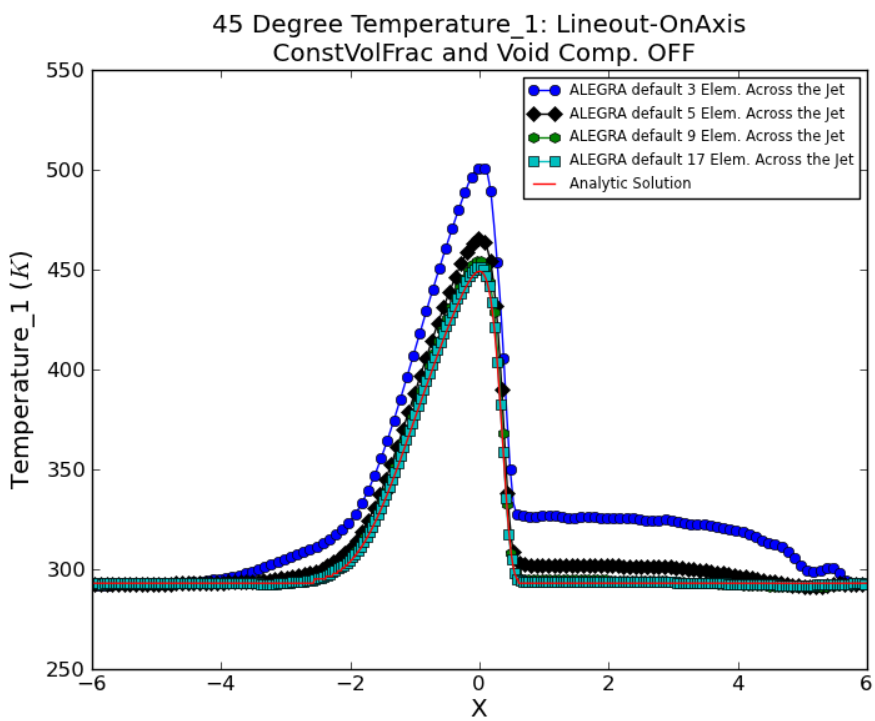

Figure 9.3. $\beta = 45°$: Temperature lineout on the axis for the CVFA. Compare with Figure 4.11.

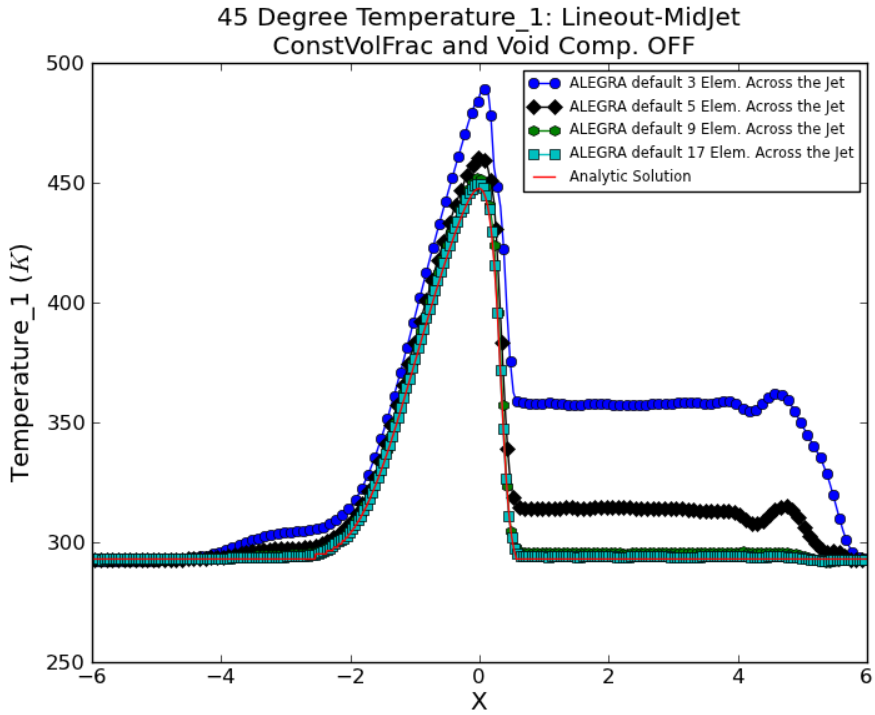

Figure 9.4. $\beta = 45°$: Temperature lineout in the middle of the jet for the CVFA. Compare with Figure 4.12.

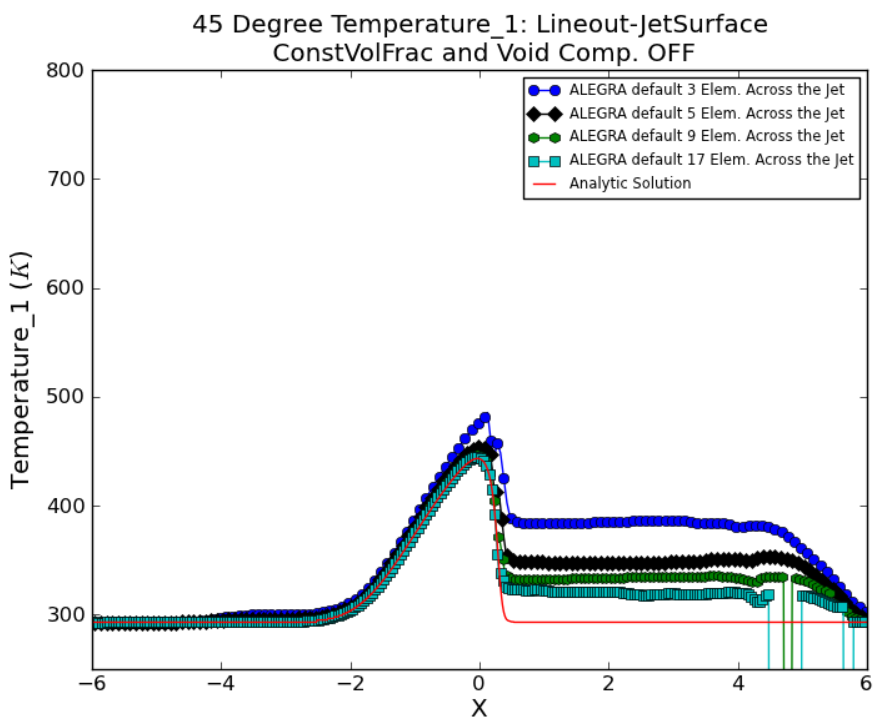

Figure 9.5. $\beta = 45°$: Temperature lineout on the jet surface for the CVFA. Compare with Figure 4.13 and 9.9.

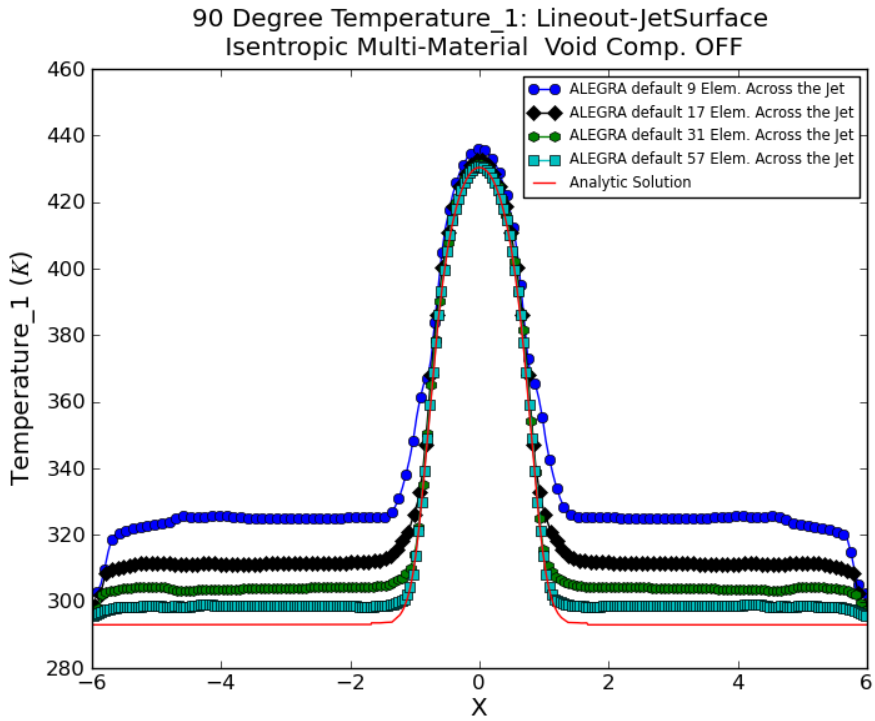

Figure 9.6. $\beta = 90°$: Temperature lineout on the jet surface for the IMMA without void compression. Compare with Figure 4.7.

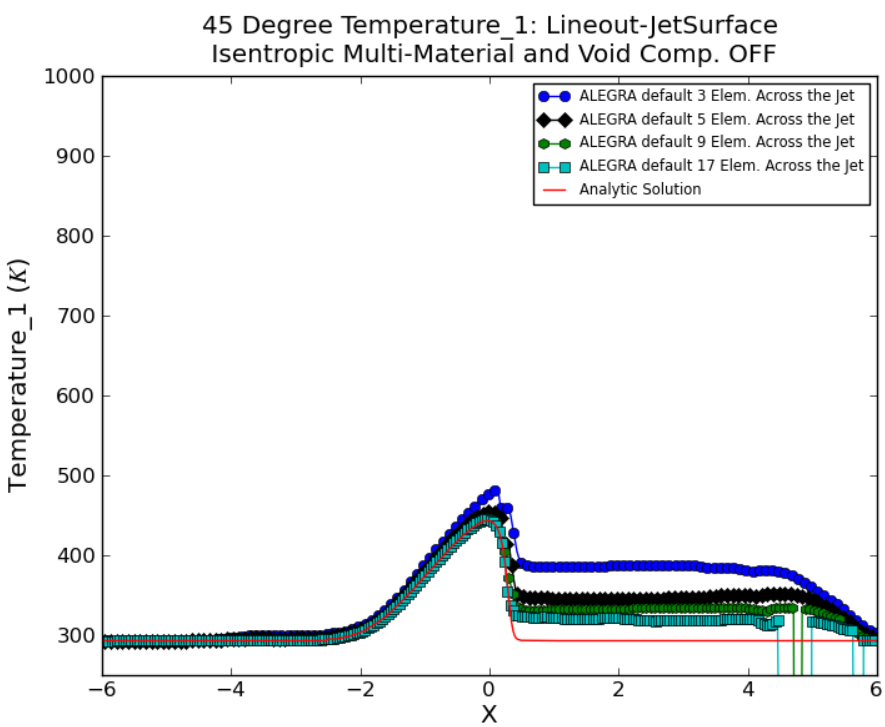

Figure 9.7. $\beta = 45°$: Temperature lineout on the jet surface for the IMMA without void compression. Compare with Figure 4.13.

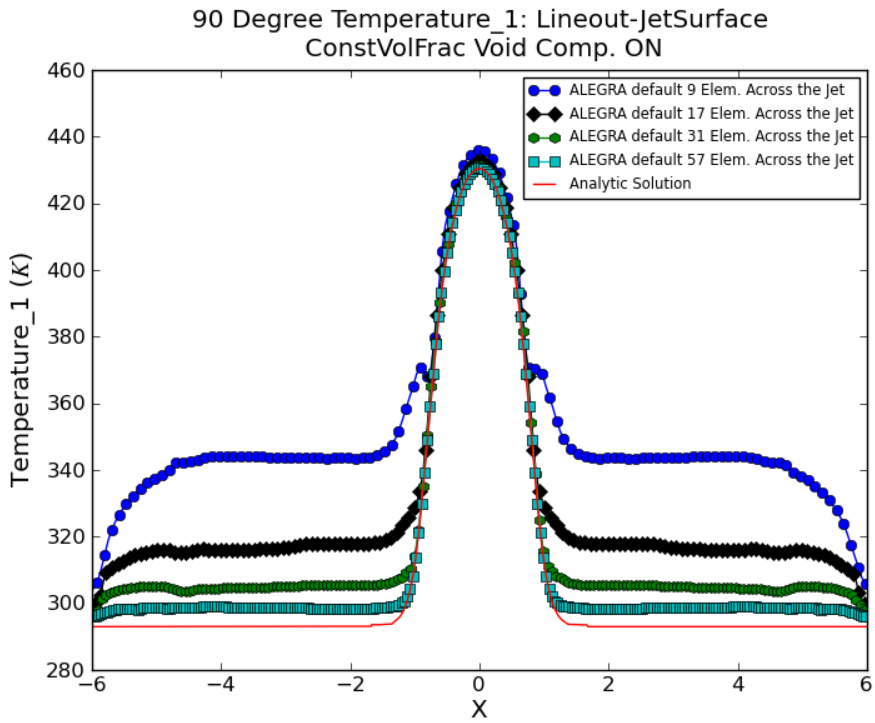

Figure 9.8. $\beta = 90°$: Temperature lineout on the jet surface for the CVFA with void compression. Compare with Figure 9.1.

Void Compression ON

The CVFA with void compression shows an increase in temperature along the surface of the jet. Figures 9.8 and 9.9 shows results for $\beta = 90°$ and $\beta = 45°$ for comparison against those previously shown in this chapter. The heating has increased along the jet surface with the void compression algorithm. Therefore, void compression could be a major factor in the heating anomalies seen in ALEGRA simulations.

The default ALEGRA code utilizes the IMMA with void compression on. Therefore the results of the standard ALEGRA shown in Chapter 4 are compared against Figures 9.6 and 9.7. This comparison shows that the IMMA without void compression has improved the results. Similar results are seen in this chapter for the CVFA, the use of void compression increases the heating along the surface of the jet.

The behavior of the plots with void compression off are similar to those shown in Chapter 8 which contains the ALEGRA XFEM results. These plots show that a major factor in the heating of the jet is related to the void compression. Improvements shown from the CVFA and IMMA are the smooth solutions, reduced heating along the jet, and they do not exhibit the subtle oscillations and interface instabilities seen in the XFEM simulations.

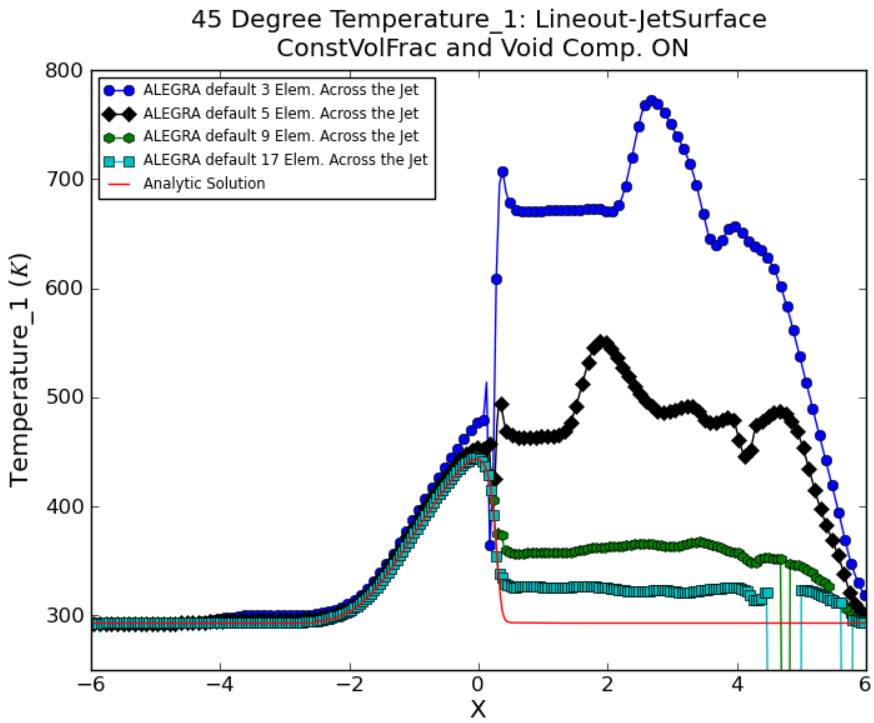

Figure 9.9. $\beta = 45°$: Temperature lineout on the jet surface for the CVFA with void compression. Compare with Figure 9.5.

Chapter 10

Lab Frame Simulations

The shaped charge test problem is also simulated using a laboratory frame of reference which provides a slightly more complex situation. ALEGRA is forced to deal with the high compression of the stagnation point and associated large velocity gradients near the tight corner in an transformed frame of reference. This chapter details the results of utilizing a laboratory frame of reference and the observed differences from the stagnation point frame of reference.

The laboratory frame of reference for the shaped charge test problem is the more traditional way of viewing a shaped charge. In these simulations the copper liner collapses, forming a jet, as shown in Figure 10.1. The collapse velocity, V_n, is assumed to be perpendicular to the copper liner. The velocity of the stagnation point, V_{sp} is based upon the inflow velocity, V_t, according to the relationships shown in Figure 10.1.

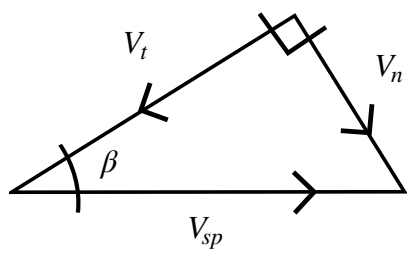

$$V_{sp} = \frac{V_t}{\cos\beta} = \frac{V_n}{\sin\beta}$$

Figure 10.1. Relationship of velocities in the laboratory frame of reference.

Figure 10.2 illustrates the laboratory frame of reference in ALEGRA. The stagnation point moves as the liner collapses as opposed to the stationary stagnation point seen in the stagnation point frame of reference (see Figure 3.1). The shaped charge test problem uses $\beta = 45°$ to simulate the collapse of the liner. Mesh resolution is the same as explained in Chapter 3 and the focus is on the under-resolved cases of 5 elements across the jet.

Analysis of the laboratory frame case is similar to that of previous chapters. Lineouts are used

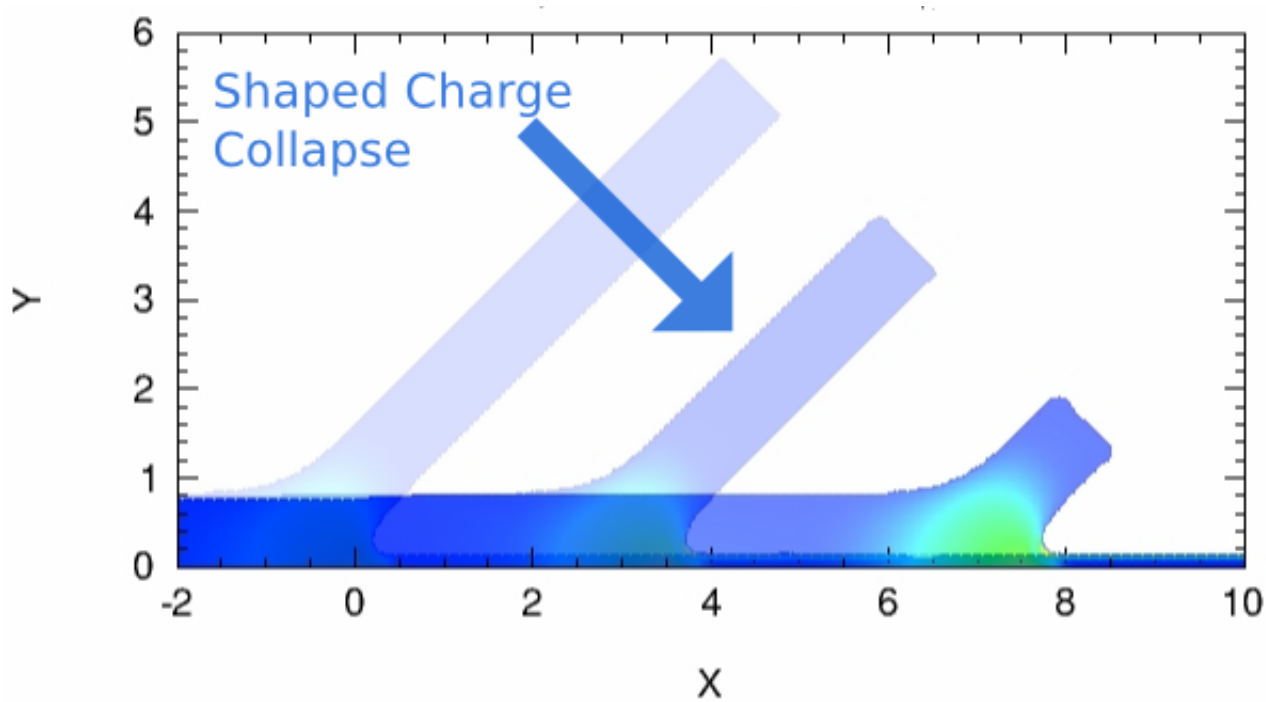

Figure 10.2. Laboratory Frame of Reference in ALEGRA for $\beta = 45°$.

to verify the ability of ALEGRA to correctly model the subsonic isentropic flow. The lineouts at the initial timestep are shifted according to the distance traveled by the stagnation point in order to overlay the lineouts of the final timestep.

Resolution as seen in Chapter 4 greatly improves the accuracy of ALEGRA. Figures 10.3 - 10.5 show temperature lineouts comparing mesh resolution for the laboratory frame of reference. Compared to Figures 4.11 - 4.13, the results of the laboratory frame of reference tend to vary. For the temperature along the axis, the results are similar for both frames of reference. See Figures 10.3 and 4.11. For comparison of the temperature along the middle of the jet for both frames of reference, see Figures 10.4 and 4.12. The laboratory frame of reference performs worse at all resolutions with the exception of the highest resolution, 17 elements across the jet. At the highest mesh resolution, both frames of reference match the analytic solution. For comparison of the temperature along the jet surface for both frames of reference, see Figures 10.5 and 4.13. The laboratory frame of reference gives mixed results. At 3 and 5 elements across the jet, the temperature is closer to the analytic solution. At 9 elements across the jet the simulations are very similar. At 17 elements across the jet, the stagnation point frame of reference is closest to the analytic solution. Thus overall, the relative quality of the laboratory frame of reference depends upon the lineout location and mesh resolution.

Standard options such as the artificial viscosity and time integrators, explored in Chapters 5

and 6, are used to test the laboratory frame of reference. Figures 10.6 - 10.8 show results for temperature lineouts. The time integrator does not have any significant effect on the results. The artificial viscosity algorithm shows very different behavior than that seen in the stagnation point frame of reference (Figures 5.5 - 5.7). In the stagnation point frame of reference the solution appears to have achieved a quasi-steady state for temperature along the jet surface while in the laboratory frame of reference the solution appears to fluctuate.

DeBar energy advection was tested with the laboratory frame of reference and results were worse than those seen in Chapter 7. Many simulations failed after only a few time steps due to catastrophic failure with extreme high and low temperatures.

The laboratory frame of reference proved to be more difficult for the XFEM in ALEGRA. Figures 10.9 - 10.11 of the laboratory frame are compared with Figures 8.4 - 8.6 of the stagnation point frame of reference. The oscillations shown in Chapter 8 have amplified causing a failure for the highest resolution, 17 elements across the jet. The lineouts on the axis, in the middle of the jet, and on the jet surface show temperature increases for all mesh resolutions when compared with the stagnation point frame of reference. Many of these increases are less than those seen in the default ALEGRA algorithms.

In general, the laboratory frame of reference did change the results slightly though many of the differences were minor. The most significant improvement was seen in the temperature lineout on the jet surface in Figure 10.5. The lowest mesh resolution, 3 elements across the jet, shows reduced heating from the stagnation point frame of reference along the jet surface. With the wide variety of options tested and retested in the laboratory frame of reference, none seem to have much impact on the shaped charge test problem with the exception of the void compression algorithm.

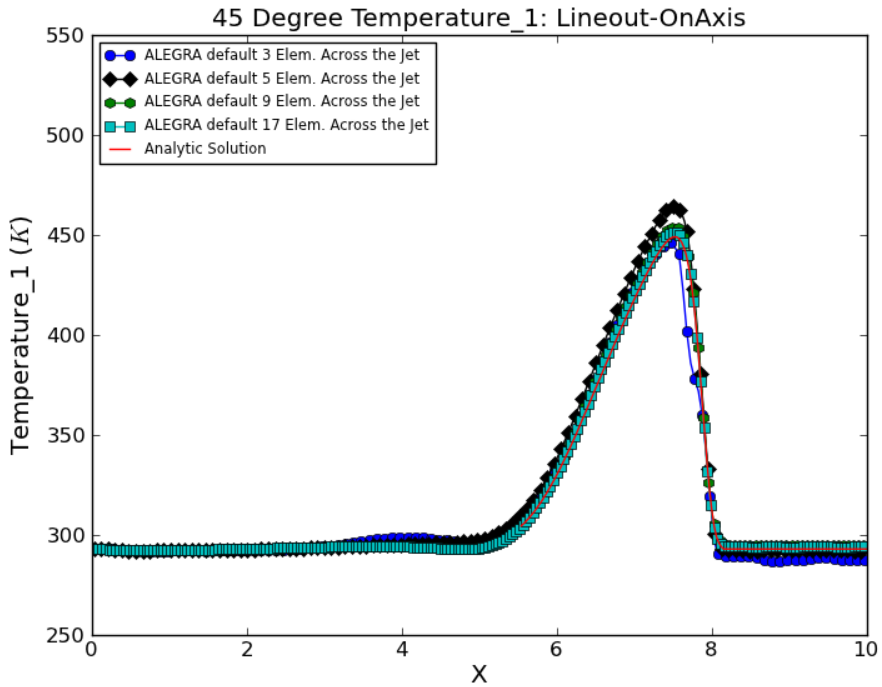

Figure 10.3. $\beta = 45°$: Temperature lineout on the axis for comparison of mesh resolution with the laboratory frame of reference. Compare with Figure 4.11.

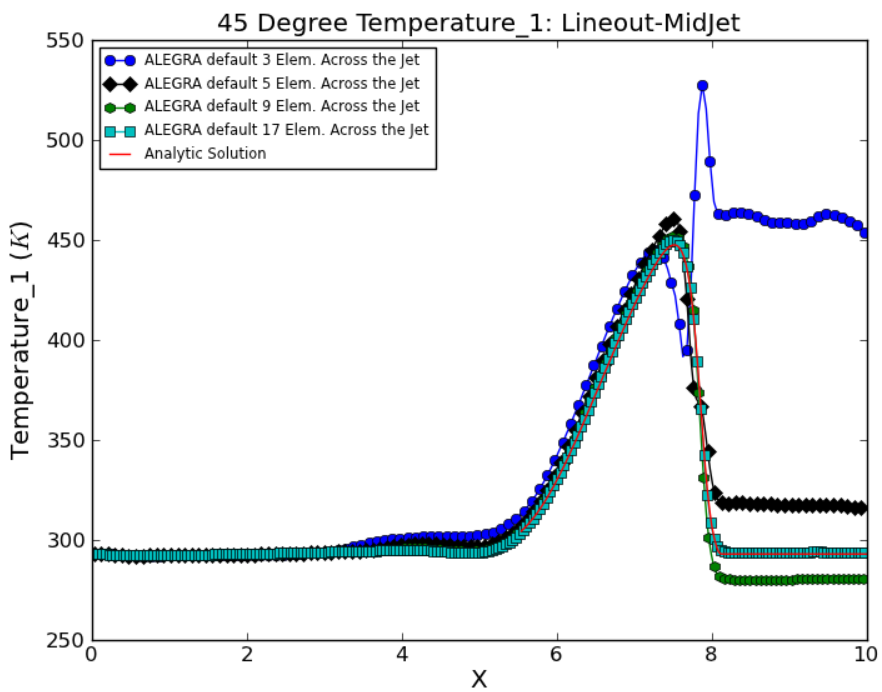

Figure 10.4. $\beta = 45°$: Temperature lineout in the middle of the jet for comparison of mesh resolution with the laboratory frame of reference. Compare with Figure 4.12.

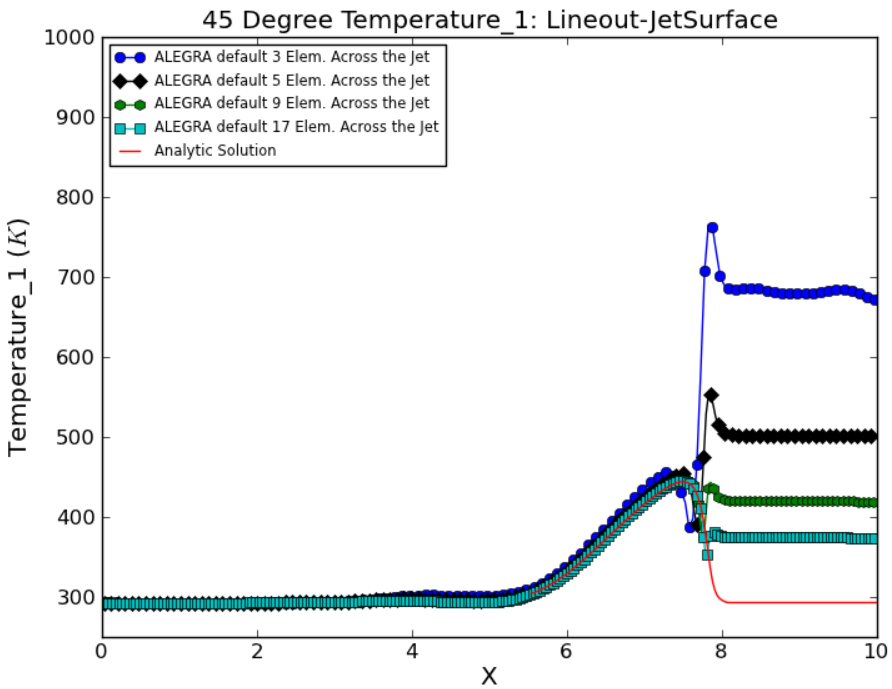

Figure 10.5. $\beta = 45°$: Temperature lineout on the jet surface for comparison of mesh resolution with the laboratory frame of reference. Compare with Figure 4.13.

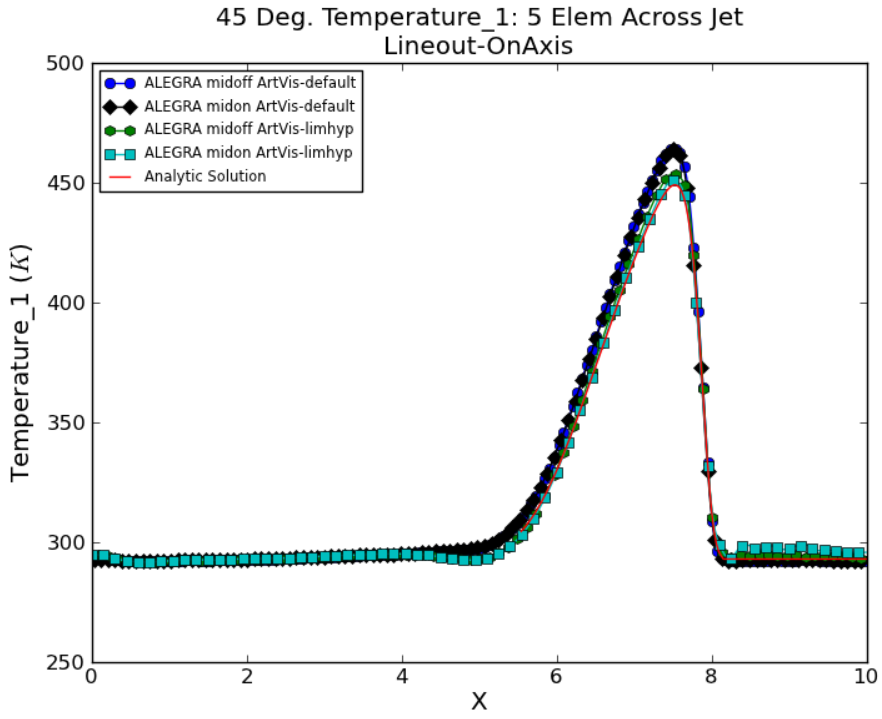

Figure 10.6. $\beta = 45°$: Temperature lineout on the axis for the laboratory frame of reference. Compare with Figure 6.2.

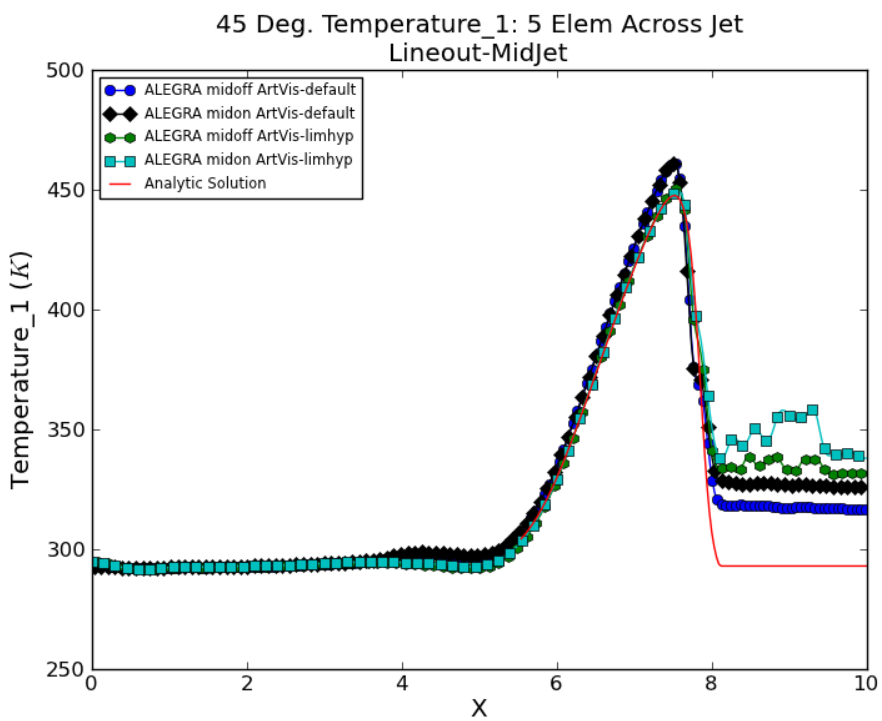

Figure 10.7. $\beta = 45°$: Temperature lineout in the middle of the jet for laboratory frame of reference. Compare with Figure 6.3.

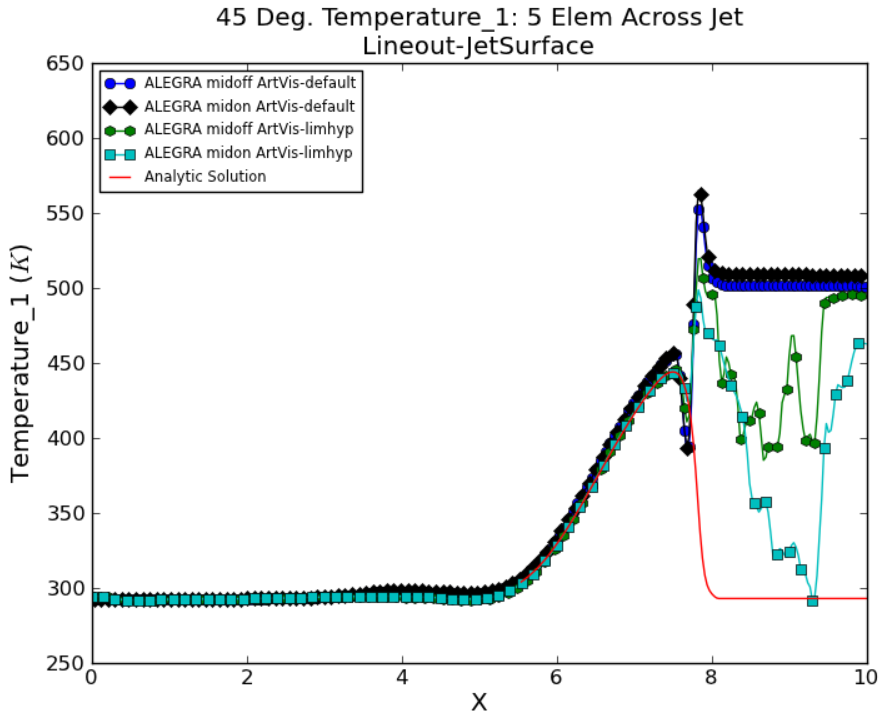

Figure 10.8. $\beta = 45°$: Temperature lineout on the jet surface for the laboratory frame of reference. Compare with Figure 6.4.

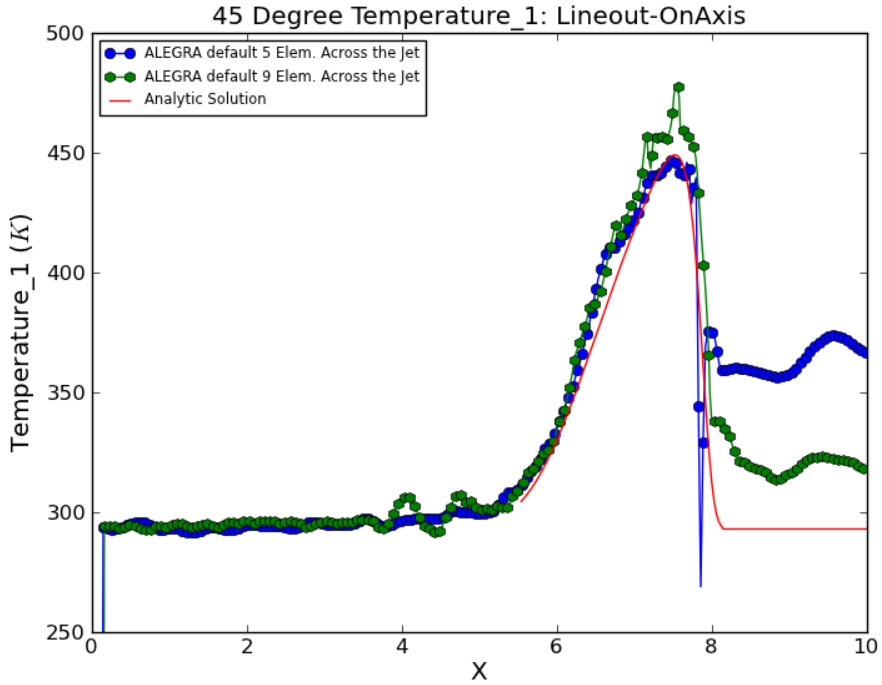

Figure 10.9. $\beta = 45°$: Temperature lineout on the axis for the laboratory frame of reference with the XFEM. Compare with Figure 8.4.

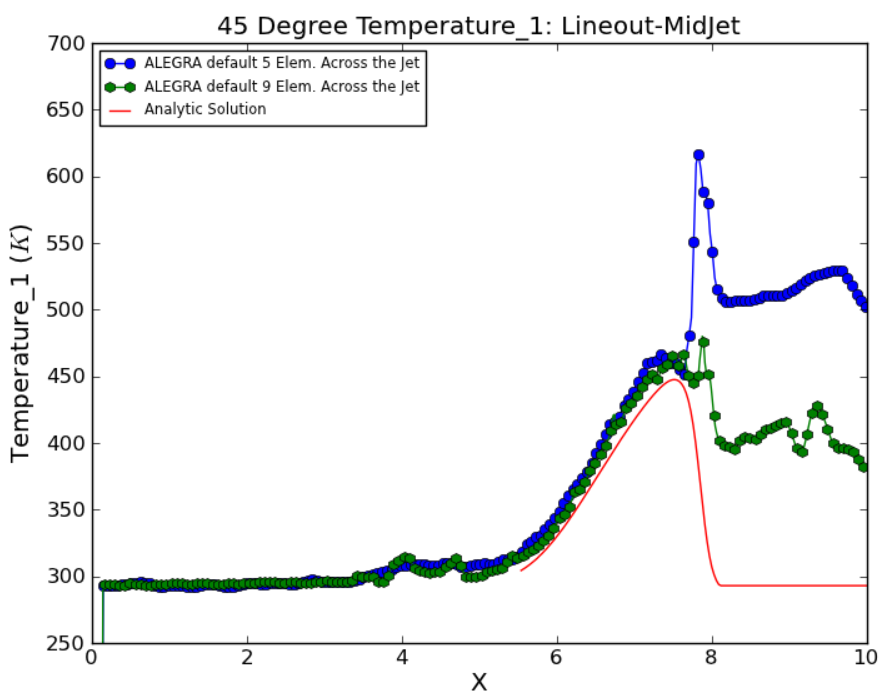

Figure 10.10. $\beta = 45°$: Temperature lineout in the middle of the jet for laboratory frame of reference with the XFEM. Compare with Figure 8.5.

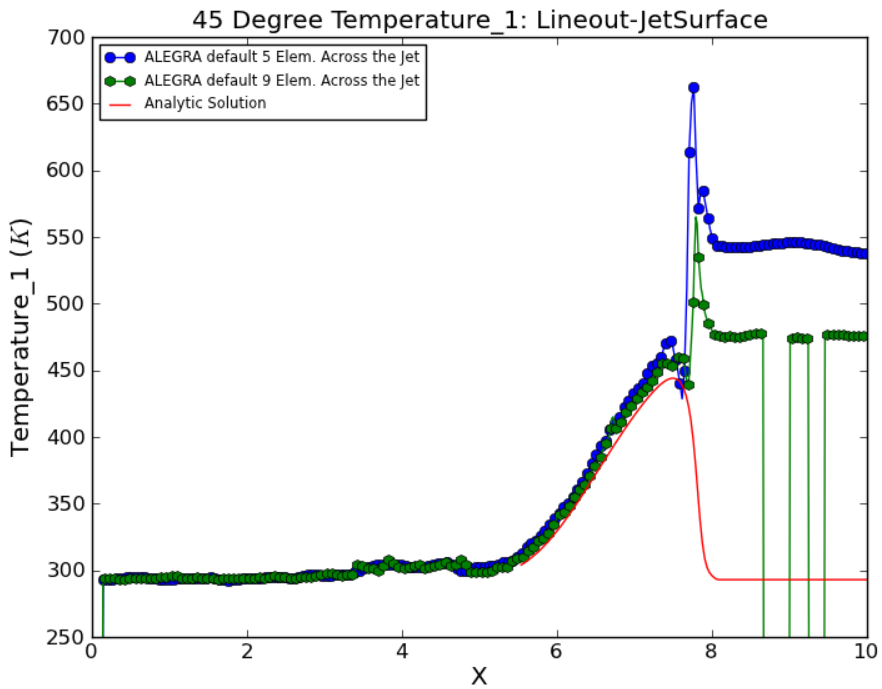

Figure 10.11. $\beta = 45°$: Temperature lineout on the jet surface for the laboratory frame of reference with the XFEM. Compare with Figure 8.6.

Chapter 11

Conclusions

We have found that the solution import capabilities in ALEGRA allow for setting up and integrating forward in time the complex steady state exact subsonic flow problem that we have described. We believe the problem is a significant test for a shock capturing, Lagrangian/Eulerian code such as ALEGRA. We found that most of the default ALEGRA algorithms performed quite well; however, there are still improvements to be made in the default algorithms, other proposed improvements, and optional algorithms. This shaped charge jet test problem creates heating anomalies on the jet surface which we believe may be associated with similar thermodynamic issues which appear in other very complex ALEGRA simulations. It provides a concrete test problem in a difficult yet controlled simulation environment. Continued analysis of the simulation results will allow for evidencial improvement of current default and proposed algorithms.

The entropy in this shaped charge prototype problem should remain constant through the entire simulation because the initial conditions constitute a steady state isentropic flow. Temperature should increase and then decrease as the material passes through the stagnation point region and then asymptote to the free stream value value in the outgoing jet or slug. In the stagnation point frame of reference where $\beta = 90^\circ$ the simulation creates minimal heating along the edge of the jet. This simulation is consistently the closest to the analytic solution. Where $\beta = 45^\circ$, the heating along the jet surface can be very severe. Evidence shows that this is primarily related to the mixed cell algorithms active in cells with partial void. Studies indicated that the mixed cell constant volume fraction algorithm and the isentropic multi-material algorithm in conjunction with the void compression algorithm constituted the most important algorithmic variants which could provide insight.

The time integration algorithm did not have a major effect on the accuracy of the simulation. In many plots there was no visible difference between the central difference and midpoint time integrators. In the cases where a change was visible it was generally small and insignificant.

DeBar energy advection was also specifically tested. In each case, DeBar has the adverse effect of increasing the heating along the jet. For this test problem DeBar also caused heating into the slug and some negative temperatures along the inflow. This algorithm needs much more detailed analysis and improvements.

New artificial viscosity algorithms were tested to see if they improved anomalous heating along the edge of the jet or in the interior. Specific parameters using the limiter and hyperviscosity were selected for the simulation. The new parameters, as seen in Table 5.1, slightly reduced the heating

along the jet surface yet results for the limiter and hyperviscosity varied for other lineouts in the jet.

Generally, the XFEM algorithms appeared to robustly run this test problem. However, some sort of anomalous wave structure is created. Heating characteristics along the jet surface are excellent and appear to be similar to results with void compression off.

At lower resolutions a significant factor is the void compression algorithm. In the current default settings of ALEGRA, a user is forced to use void compression with the IMMA. Switching to the CVFA without void compression or minor changes to the IMMA to remove void compression greatly reduced the heating along the jet surface. At higher resolutions these algorithms do not have significant effect.

The default settings in ALEGRA with a resolved mesh appear to be the most accurate and consistent results obtained up to this point. The major issues in the simulations occur along the edge of the jet and can be significantly reduced by increasing the mesh resolution. It has been determined that the thermodynamic anomalies in the simulations are related to mixed cells. Cells that include material and void appear to be causing the anomalies and it appears that this work recommends a detailed look at current algorithms that interact with mixed material/void elements.

The resuls and recommendations given herein are specifically for the version of the ALEGRA repository head code as of August 2013 and as such are subject to change in the current dynamic research and development environment. The test problem setups presented here are integrated into the ALEGRA test suite and maintained daily. ALEGRA tools are utilized to compute the norm of the simulation and exact solution lineouts in the jet. These tools can thus indicate any improvement or decline in the performance of the code for this problem. As such, these problems represent an example of test driven development in which ALEGRA developers are able to test new and improved algorithms against a well characterized solution in a permanent testing environment. Thus a continually improving state of code quality will be maintained as algorithms are improved and benchmarked against this exact solution.

References

[1] M. Abramowitz and I. A. Stegun. *Handbook of Mathematical Functions*. Dover Publications, Inc., New York, 1972.

[2] L. Bers. *Mathematical Aspects of Subsonic and Transonic Gas Dynamics*. John Wiley and Sons, New York, 1958.

[3] G. Birkhoff, D. P. MacDougall, E. M. Pugh, and G. I. Taylor. Explosives with lined cavities. *J. Appl. Phys.*, 19:563–582, 1948.

[4] G. Birkhoff and E. H. Zarantonello. Jets, wakes and cavities. In *Applied Mathematics and Mechanics*, volume II. Academic Press, New York, 1957.

[5] S. A. Chaplygin. On gas jets. Technical report, Moscow University, 1902. In Russian, Translated in NACA Technical Memorandum No. 1063, 1944.

[6] P. C. Chou, J. Carleone, and R. Karpp. Criteria for jet formation from impinging shells and plates. *J. Appl. Phys.*, 47(7), July 1976.

[7] L. Pamela Cook, Elsa Newman, Scoot Rimbey, and Gilberto Schleiniger. Sonic and subsonic axisymmetric nozzle flows. *SIAM J. Appl. Math.*, 59(5):1812–1824, 1999.

[8] J. Dolbow, S. Mosso, J. Robbins, and T. Voth. Coupling volume-of-fluid based interface reconstructions with the extended finite element method. *Computer Methods in Applied Mechanics and Engineering*, 197(5):439 – 447, 2008.

[9] J. Dolbow, N. Mos, and T. Belytschko. Discontinuous enrichment in finite elements with a partition of unity method. *Finite Elements in Analysis and Design*, 36(3-4):235–260, 2000.

[10] D. F. Ferguson and M. J. Lighthill. The hodograph transformation in transonic flow, IV. tables. *Proc. Roy. Soc*, A192:135–142, 1947.

[11] Evelyn Frank. *Continued Fraction Expansions for the Ratios of Hypergeometric Functions Evaluated on Computers*, volume 419, pages 110–119. Springer, Berlin, 1974.

[12] K. G. Guderley. *The Theory of Transonic Flow*. Pergamon Press, 1962.

[13] M. I. Gurevich. *The Theory of Jets in an Ideal Fluid*. Pergamon Press, Oxford, 1965.

[14] R. R. Karpp. An exact partial solution to the compressible flow problems of jet formation and penetration in plane, steady flow. *Quart. Appl. Math*, pages 15–29, 1984.

[15] R. R. Karpp and S. Goldstein. Modifications to the hydrodynamic computer code HELP. Technical Report M-4-1596, Los Alamos National Laboratory, December 1977. Work for U. S. Army Ballistic Research Lab. under Army Project Order N721-77.

[16] Ray Kinslow, editor. *High-Velocity Impact Phenomena*. Academic Press, New York, 1970.

[17] E. Love, W. J. Rider, and G. Scovazzi. Stability analysis of a predictor/multi-corrector method for staggered-grid lagrangian shock hydrodynamics. *Journal of Computational Physics*, 228:7543–7564, 2009.

[18] E. Love, G. Scovazzi, and W. J. Rider. Algorithmic properties of the midpoint predictor-corretor time integrator. Technical Report SAND2009-1127, Sandia National Laboratories, Albuquerque, NM, 2009.

[19] W. C. Mills-Curran, A. P. Gilkey, and D. P. Flanagan. Exodus: A finite element file format for pre- and postprocessing. Technical Report SAND87-2997, Sandia National Laboratories, 1987.

[20] R. Von Mises. *Mathematical Theory of Compressible Fluid Flow*. Academic Press, Inc., New York, 1958.

[21] G. Y. Nieuwland. Transonic potential flow around a family of quasi-elliptical aerofoil sections. Technical Report T-172, National Aerospace Lab NLR, Amsterdam, 1967.

[22] W. F. Noh. Errors for calculation of strong shocks using an artificial viscosity and an artificial heat flux. *J. Comp. Phys.*, 72:78–120, 1978.

[23] C. E. Pearson. Extension of a numerical streamline method. *Comm. Appl. Num. Meth.*, 1:177–181, 1985.

[24] E. Racah. Shaped charge jet heating. *Propellants, Explosives, Pyrotechnics*, 13:178–182, 1988.

[25] W. J. Rider, E. Love, G. Scovazzi, and V. G. Weirs. A high resolution lagrangian method using nonlinear hybridization and hyperviscosity. *Computers & Fluids*, 83:25–32, 2013.

[26] W. J. Rider, E. Love, M. K. Wong, O. E. Strack, S. V. Petney, and D. A. Labreche. Adaptive methods for multi-material ALE hydrodynamics. *International Journal for Numerical Methods in Fluids*, 65(11-12):1325–1337, 2011.

[27] J. Robbins and T. Voth. An extended finite element method formulation for modeling the response of polycrystalline materials to dynamic loading. In *AIP Conference Proceedings*, volume 955, page p259, December 2007.

[28] A. C. Robinson. Evaluation techniques and properties of an exact solution to a subsonic free surface jet flow. Technical Report SAND2002-1015, Sandia National Laboratories, 2002.

[29] A. C. Robinson, J. H. J. Niederhaus, V. G. Weirs, and E. Love. Arbitrary lagrangian-eulerian 3d ideal mhd algorithms. *International Journal for Numerical Methods in Fluids*, 65:1438–1450, 2011.

[30] A. C. Robinson, W. J. Rider, et al. ALEGRA: an arbitrary Langrangian-Eulerian multimaterial, multiphysics code. In *Proceedings of the 46th AIAA Aerospace Sciences Meeting, Reno, NV*, January 2008. AIAA-2008-1235.

[31] J. A. Schmitt. Truncation error terms in the kinetic energy calculation in the HELP algorithm and their consequences. *J. Comp. Phys.*, 35:206–228, 1980.

[32] L. I. Sedov. *Two-dimensional Problems in Hydrodynamics and Aerodynamics*. Interscience Publishers, New York, 1965.

[33] V. Stodden, I. Mitchell, and R. LeVeque. Reproducible research for scientific computing: Tools and strategies for changing the culture. *Computing in Science and Engineering*, 14(4):13–17, 2012.

[34] W. J. Thron and H. Waadeland. Accelerating convergence of limit periodic continued fractions k(a_n/1). *Numer. Math.*, 34:155–170, 1980.

[35] E. D. Tomilov. *Two-Dimensional Subsonic Gas Flows: Basic Methods and Problems*. Novosibirsk, Izdatel'stvo Nauka, 1980. Available in Russian from AIAA TIS as A81-31825.

[36] E. Vitali and D. J. Benson. An extended finite element formulation for contact in multi-material arbitrary lagrangian–eulerian calculations. *International Journal for Numerical Methods in Engineering*, 67(10):1420–1444, 2006.

[37] J. VonNeumann and R. D. Richtmyer. A method for the numerical calculation of hydrodynamic shocks. *Journal of Applied Physics*, 21(3):232–237, 1950.

[38] W. P. Walters and J. A. Zukas. *Fundamentals of Shaped Charges*. John Wiley and Sons, New York, 1989.

[39] J. Wimp. *Sequence Transformations and Their Applications*. Academic Press, New York, 1981.

[40] Jonas A. Zukas, Theodore Nicholas, Hallock F. Swift, Longin B. Greszczuk, and Donald R. Curran. *Impact Dynamics*. John Wiley and Sons, 1982.

Appendix A

Exact Solution Evaluation Code

In the spirit of test reproducibility, we intend to make the code, CJETB, used to evaluate the exact jet solution described in the text, freely available to interested researchers [33]. Please contact Allen Robinson (acrobin@sandia.gov) for information related to obtaining a copy of the source code and a sample input file.

The code writes out data in the EXODUS I finite element database format and as x-y pair data for plotting [19]. It is expected that any user interested in running the CJETB code will have access to reasonable post-processing procedures for this type of data and may modify the code with little effort to be compatible with any particular finite element database format.

Setting up this solution as a useful verification problem for a transient flow shock capturing code may require some ingenuity since the solution presented here is steady state. It is very important that the initial conditions in the transient code should be given as closely as possible by the exact solution to avoid transients that will destroy the ability to compare the solution later in time. Since the flow has a stagnation point, it will take some time for any initial transient response to be advected out of the problem. These issues need to be examined and monitored carefully.

The steady state defined by this exact solution can be used as a test of an arbitrary mesh to mesh transfer capability. Indeed, for the testing process discussed in the report to be effective such a mesh to mesh transfer capability must be in place.

Distribution

External Distribution:

U.S. Army Research Laboratory
Attn:
Robert L. Doney (electronic copy)
Andrew J. Porwitzky (electronic copy)

Los Alamos National Laboratory
Attn:
M. Shashkov (electronic copy)

Internal Distribution:

MS 1323 Bradley W. Hanks, 01443 (electronic copy)
MS 1323 Allen C. Robinson, 01443 (electronic copy)
MS 1323 O. Erik Strack , 01443 (electronic copy)
MS 1323 William J. Rider, 01443 (electronic copy)
MS 1323 Ed Love, 01443 (electronic copy)
MS 1323 John Niederhaus, 01443 (electronic copy)
MS 1323 Richard R. Drake, 01443 (electronic copy)
MS 1323 Sharon Petney, 01443 (electronic copy)
MS 1323 Jay Mosso, 01443 (electronic copy)
MS 1323 Thomas E. Voth, 01443 (electronic copy)
MS 1323 Jason Sanchez, 01443 (electronic copy)
MS 0840 John Pott, 01525 (electronic copy)
MS 0847 Stephen W. Attaway,01525 (electronic copy)
MS 0836 David W. Crawford, 01525 (electronic copy)
MS 0836 Eric N. Harstad, 01525 (electronic copy)
MS 0828 Kevin Rugerillo, 01525 (electronic copy)
MS 0836 Robert G. Schmitt, 01525 (electronic copy)
MS 0836 Shane Schumacher, 01525 (electronic copy)

MS 0899 Technical Library, 9536 (electronic copy)

Sandia National Laboratories